ALBERT-LUDWIGS UNIVERSITÄT FREIBURG

Groundwater Model of the Swakop River Basin, Namibia

by

Florian Winker

Diploma Thesis

in the
Faculty of Forest and Environmental Sciences
Institute of Hydrology Freiburg

Supervisor: Dr. Christoph Külls
Co-Supervisor: Prof. Dr. Markus Weiler

February 2010

Declaration of Authorship

I, Florian Winker, declare that this thesis titled, 'Groundwater Model of the Swakop River Basin, Namibia' and the work presented in it are my own.

I confirm that the work was made independently and only on the use of indicated resources.

Signed: ____

Date: ____

"Schnell wachsende Keime welken geschwinde, zu lange Bäume brechen im Winde. Schätz nach der Länge nicht das Entsprungene, fest im Gedränge steht das Gedrungene."

Wilhelm Busch

Abstract

A numerical groundwater model study of the regional groundwater movement in the Swakop River basin (30100 km^2), Namibia has been conducted. The basin will be target of intensive economic development and associated migration. Both will have strong impacts on the availability of groundwater. The aim was to develop an initial understanding of the groundwater flow system, to determine recharge and discharge areas as well as possible direct recharge rates consistent with the basin geology. Furthermore, potential interactions between alluvial aquifers and the basement were investigated.
Geologically, the study area is built up by a versatile hard rock lithology and climatically, it is characterized by low annual rainfall and huge evaporation rates. Three conceptual models were constructed, while increasing complexity. One challenge was the implementation of the versatile (folded and fractured) underlying lithology on the large scale using a coarse grid size within the finite difference flow model, MODFLOW SURFACT. This was achieved by using the EPM approach and a classification of hydrogeological units rested on the generalisation of lithological layers according to the Hydrogeological Map of Namibia as well as the introduction of a exponential decrease of hydraulic conductivity with depth. Basin wide recharge rates, determined with the different models range from 0.25 mm/a to 2.25 mm/a. Best model performance achieved, resulted in a mean absolute error of 22.12 m and a root mean square error of 28.37 m ($R^2 = 0.992$). On the regional scale results show that groundwater is mainly recharged at the basin margins as well as along a line of potentiometric mounds, which trend from the northeast of Wilhelmstal alongside the ridges of the Otjipatera and Chous Mountains to the southwest. From these mounds, groundwater diverges to the northeast and southwest into the subbasins of the Khan and Swakop Rivers, respectively. This large scale flow pattern consists a complex conglomerate of local and intermediate flow systems, where recharge areas alternate with their adjacent discharge areas which are preferably located in troughs and river valleys. In contrast, no deep, regional groundwater flow system was identified, since no connected flow lines between the lower points and higher elevations in the basin exist. This was confirmed by particle tracking analyses conducted at different locations in the basin.
Mass balance computations and particle tracking analyses in six selected river compartments insinuated different intensities of basement water influences depending on climatic and topographic basin characteristics. This was most clearly shown in the compartments of the Khan River where basement fluxes into the alluvial aquifer of the Khan River increased towards the confluence.

Zusammenfassung

Für das 30100 km^2 große Einzugsgebiet des Swakop in Namibia, wurde anhand eines numerischen Grundwassermodells das regionale Grundwassersystem untersucht. Das Untersuchungsgebiet ist gekennzeichnet durch eine vielfältige Festgesteinslithologie sowie geringe jährliche Niederschläge und hohe Verdunstungsraten. Ziel der Arbeit war eine erste Klassifizierung des Grundwasserfließsystems und die Lokalisierung potentieller Grundwasserneubildungs und Quellgebiete. In Abhängigkeit der vorherrschenden Geologie sollten mögliche direkte Grundwasserneubildungsraten bestimmt werden. Zudem wurden potentielle Interaktionen zwischen den alluvialen Aquiferen und dem Grundgebirge untersucht. Drei Konzeptmodelle wurden entwickelt, die sich in ihrer Komplexität, hinsichtlich der Berücksichtigung einzugsgebietsspezifischer Merkmale unterscheiden. Eine Herausforderung war die Implementierung der gefalteten und geklüfteten Lithologie in das finite Differenzenmodell MODFLOW SURFACT. Hierfür wurde der Kontinuum Ansatz angewandt, unter der Annahme einer exponentiellen Abnahme der hydraulischen Leitfähigkeit mit der Tiefe. Die Diskretisierung der Lithologie wurde anhand der hydrogeologischen Karte von Namibia umgesetzt. Die mit den drei verschiedenen Modellen bestimmten Neubildungsraten liegen zwischen 0,25 und 2,25 mm/a. Das beste Modellergebnis wies Fehler von 22,12 m (MAE) und 28,37 m (RMS) auf. Im regionalen Maßstab betrachtet, zeigen die Ergebnisse, dass Grundwasserneubildung hauptsächlich sowohl an den Rändern des Einzugsgebiets als auch entlang potentiometrischer Grundwasserhügel stattfindet, welche entlang südwestlich verlaufender Gebirgsrücken liegen. Von hieraus fließt das Grundwasser nordöstlich in das Teileinzugsgebiet des Kahns und südwestlich in das des Swakops ab. Dieses makroskalische Fließmuster setzt sich aus einer Ansammlung komplexer, lokaler und mesoskalischer Fließsysteme zusammen, wobei Neubildungs- und Quellgebiete alternieren. Quellgebiete sind darin hauptsächlich in Trögen und (Fluss-)tälern aufzufinden. Ein tiefes regionales Grundwasserfließsystem konnte aufgrund nicht identifizierter Fließwege zwischen hoch und tief gelegenen Regionen nicht nachgewiesen werden. Dies wurde durch mehrere Particle Tracking Analysen bestätigt. Die Massenbilanzen und die Auswertung von Particle Tracking Analysen in sechs ausgewählten Abschnitten der alluvialen Aquifere zeigten, dass diese unterschiedlich von Grundwsser aus dem Festgestein beeinflusst werden. Dies ist abhängig von den lokal vorherrschenden klimatischen und topographischen Gegebenheiten des Einzugsgebiets. Dies konnte am besten anhand des Khans gezeigt werden, in welchem influente Bedingungen in Richtung der Flussmündung zunehmen.

Acknowledgements

Sincerely, I would like to thank Dr. Christoph Külls for his guidance throughout this thesis.
His support and patience helped me a lot.
Thanks for the motivation and spending so much time in discussions.

I would also like to thank Prof. Dr. Markus Weiler for making this work possible and for the co-supervision of the thesis.

Thanks also go to the diploma students for their advice and help.

Finally, I would like to thank my familiy and friends who directly and indirectly contributed to this work.

Contents

List of Figures

List of Tables

Abbreviations

a.s.l.	**a**bove **s**ea **l**evel
b.g.l.	**b**elow **g**round **l**evel
CZ	**C**entral **Z**one
EPM	**E**quivalent **P**orous **M**edia
ET	**E**vaporation
I	**I**ndicator
MAE	**M**ean **A**bsolute **E**rror
OL	**O**kahadja **L**ineament
OML	**O**maruru **L**ineament
P	**P**recipitation
$\mathbf{R}^2$	coefficient of determination
Rch	**R**echarge
RH	**R**elative **H**umidity
RMS	**R**oot **M**ean **S**quare error
SZ	**S**outhern **Z**one
sCZ	**s**outhern **C**entral **Z**one
TI	**T**opographic **I**ndex

Symbols

A	area	L^2
b	saturated thickness	L
c	constant	
C	mass transfer coefficient	$\mathrm{L/ML^{-1}T^{-1}}$
D	decay coefficient	L
e	vapour pressure	$\mathrm{ML^{-1}T^{-2}}$
e_s	saturation vapour pressure	$\mathrm{ML^{-1}T^{-2}}$
g	constant of gravity	$\mathrm{L/T^2}$
G	volumetric source/sink term	1/T
h	piezometric head	L
$k_{x,y,z}$	hydraulic conductivities	L/T
K	permeability	L^2
l	length	L
n	porosity	1
p	presurre	$\mathrm{M/L/T^2}$
Q	discharge	$\mathrm{L^3/T}$
R	universal gas constant	$\mathrm{J/mol^{-1}K^{-1}}$
S	storativity	1
S_S	specific storage	1/L
S_w	degree of water saturation	1
S_y	specific yield	1
t	time	T
T	temperatur	K
T	transmissivity	$\mathrm{L^2/T}$
v	velocity	L/T

x, y	length, width	L
z	height (in direction of g)	L
β	compressibility	T^2L/M
γ	decay coefficient	L
η	dynamic viscosity	M/L/T
λ	decay coefficient	1
ρ	density	M/L^3

Dedicated to my family

Chapter 1

Introduction

The westward draining Swakop River basin, presenting Namibia´s largest basin with an area of 30,100 km^2 will be target of intensive economic development and associated migration. Both will have strong impacts on the availability of groundwater.
As the driest country in Africa, Namibia´s water resources are commonly scarce and barely reliable. Surface waters are exposed to high evaporation especially during droughts, and floods as a result of strong rainfall events are not easy to handle. Therefore groundwater, which is available even during droughts is a essential component of water supply. The knowledge about its spatial and temporal distribution facilitates a sustainable water resource management in terms of over-exploitation and consequent negative environmental impacts.
The Swakop River Basin is coined by thin soils and hard rock crystalline and metamorphic geology in which the ephemeral Swakop and Khan Rivers are embedded. The rivers present important groundwater suppliers due to the high yields of their alluvial porous aquifers. These ephemeral systems were altered due to constructions of surface water dams and will furthermore be required for the intensified future water demand. Therefore river compartments are investigated and numerically modeled.
Still existing open cast uranium mining and the exploitation and operation of further mineral deposits in the basin require large volumes of water. According to *Ellmies* (2009) 7 Mm^3/a water were required by uranium mines in the year 2008 and the demand will possibly raise up to 48-64 m^3/a till the year 2015. The installation and use of desalination plants represent a possibility to account for the increasing demand, but can also have negative influence on the system, through the feed-in of sewages.
Groundwater contour lines derived from boreholes distributed within the basin (either located within hard rock areas or within the alluvial aquifers) insinuate a connected flow system on the regional scale with a gradient toward the Atlantic Ocean. Besides in the western part of the basin is a zone of saline groundwater, which could be caused

by evaporation of upwelling water in a regional discharge zone. Furthermore, chemical compositions of water from the alluvial aquifers indicate dues of basement water and pose the question, if there is an lateral and/or vertical in flow from the basement into the alluvial aquifer and where does it occur?

A physically based and distributed model provides a opportunity to simulate the groundwater systems of a large basins like the Swakop River Basin. The more physically based individual processes are represented and the less conceptual a model is, the better it can be used for scenario analysis and decision making (*Wolf et al.*, 2008).

A reasonable solution of the model will provide boundary conditions for subregional, local and/or compartment models of the alluvial aquifers and could be used as a basis for long term assessments and possible future scenarios, respectively.

1.1 State of the Art

Through its aptitude to interact with the ambient environment and its systematized spatial distribution of flow, both, in all scales of space and time, groundwater plays a active and important role in nature. Three main types of interactions between groundwater and the environment exist: Chemical interaction, relating to different chemical reactions (e.g. dissolution, oxidation-reduction); physical interaction with regard to processes of lubrication and pore-pressure modification and at last kinetic interaction involving the transport of water, heat and mass (*Tóth*, 1999).

Corresponding to *Tóth* (1962, 1999) three hydraulically different regions of groundwater movement in drainage basins can be delineated (Figure 1.1): recharge-, discharge- and through flow- or midline areas. In a local flow system the discharge area is immediately close to its recharge area. A intermediate system may overstretch one or more local flow system, but does not extend from the principle watershed to the main valley and in a regional flow system the principal recharge area is connected with the principle discharge area of the basin. But nevertheless drainage basins are often a conglomerate of all different hydraulic regions spatially overlapping.

To describe elements of groundwater flow mathematical models use mathematical equations . These models can be empirical, probabilistic or deterministic, depending upon the nature of equations they use.

Empirical models are derived from experimental data, that are fitted to some mathematical function (e.g. Darcy´s law). The disadvantage of these models is, they are limited in scope and usually site or problem specific.

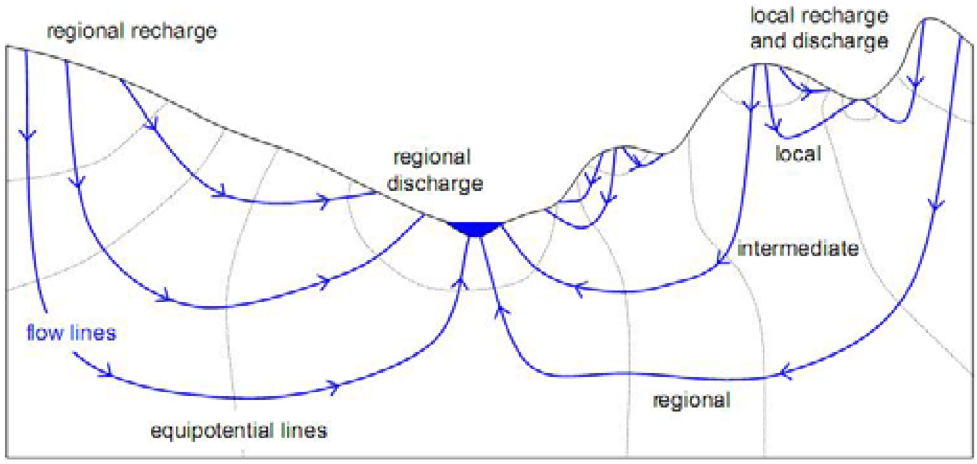

FIGURE 1.1: Schematic flow systems of local, intermediate and regional groundwater flow (*Feyen* (2005) after *Tóth* (1962))

Probabilistic models use laws of probability and statistics. They can have divers forms and complexity. Usually by starting with a simple probabilistic distribution of a hydrogeological property of interest and ending with complicated stochastic time-dependent model. An overview of this type of models is given by *Dagan* (2002).
Deterministic models are the common model type used in groundwater investigation. They assume that reactions of a system are predetermined by physical laws governing groundwater flow. They can be sophisticated as a multiphase flow through a multi layered, heterogeneous, anisotropic aquifer system or as facile as the Theis equation for two dimensional radial flow to a point source in an infinite, homogeneous aquifer.
Depending upon the type of mathematical equations involved, a distinction is made between two large groups of deterministic models, namely analytical or numerical models (*Kresic*, 2006).
Simply stated, analytical models solve one equation of groundwater flow at a time and the result can be applied to one point or line of points in the analyzed flow field.
The first mathematically modeling of groundwater flow may be attributed to *Tóth* (1962) and *Tóth* (1963), who found a analytical solution for describing groundwater flow in homogeneous lithology, by introducing boundary conditions. This equation related the fluid potential to the earth acceleration constant, topographic gradient of the valley flank, horizontal distances between water divide and valley bottom, elevation above a horizontal impermeable boundary, elevation of the water table at the valley bottom above a horizontal impermeable boundary and horizontal distance from the valley bottom. By the use of this equation possible flow patterns and potential distributions were obtained.

Large scale modeling:

Modeling of large/regional scale areas encounters difficulties of identifying and considering the main properties and processes taking place. Therefore often simplifications are made.
Large scale watershed models have been applied to problems of surface water management without treating groundwater in much detail, by assuming that percolation from the soil profile is lost from the system, and thus ignore it. Several studies describe large scale surface water models for catchments larger than 50000 km^2, not including modeling the groundwater system, except for the routing of base flow in large linear reservoirs (a review is given by *Refsgaard* (2001)).
Coupled models commonly describe groundwater surface water interactions based on the conductance concept that implies a particular interface at the land surface, separating the surface from the subsurface domain. With an exchange flux, that depends upon the magnitude and direction of the hydraulic gradient across the interface and a proportionality constant (e.g. hydraulic connectivity) the two domains are linked. The exchange flux appears in both the groundwater and the surface water equations as general source/sink terms. Examples for large scale coupled models are given by *Kim et al.* (2008), *Gunduz & Aral* (2005),*Anderson et al.* (2001), *Said et al.* (2005), *Yu et al.* (2006) and *Bauer et al.* (2006).
For example *Anderson et al.* (2001) applied a modified version of the physically based distributed MIKE SHE model code (*Refsgaard & Storm*, 1995) to the 375,000 km^2 Senegal River basin. Here gravity driven flow was assumed for the unsaturated zone and the groundwater flow simulation was based on flow between interconnected storages, semi-distributed and conceptual.
Yu et al. (2006) describe a method of coupling climate and hydrological models on the continental scale, based on categories of fine grid hydrological cells with in each coarse grid climate cell. This coupling technique addresses the heterogeneity of infiltration and evaporation due to small scale variations in surface moisture and surface water. The groundwater compartment was modeled in the hydrological model as a one layer aquifer, representing a single bedrock unit extending from the surface to a depth of tens to a few hundred meters with an impervious (no-flow) base. Hydraulic properties of the single bedrock layer for the conterminous U.S. were determined from the USGS Hydrologic Atlas for the simulation of the North American continent. Hydrologic parameters for each lithologic type were aggregated for the 20 km x 20 km grid.

Large scale groundwater modeling is often conducted by the use of deterministic, physically based, numerical models. The advantage of a deterministic, numerical groundwater flow model is that it provides much more information than conceptual water balance models often used on the regional scale. Spatial distributions of hydraulic heads, the description of horizontal and vertical flows, flow directions, velocities and the quantitative simulations of groundwater discharge into surface waters can be computed (*Wolf et al.*, 2008).
One of the largest groundwater investigation study found in literature , in which the groundwater was numerically modeled is given by *Gossel et al.* (2004). They constructed a GIS-based groundwater flow model for the Nubian sandstone aquifer in the eastern Sahara (Egypt, northern Sudan and eastern Libya) and simulated the response of the aquifer to climate changes that occurred during the last 25,000 years. Two three dimensional numerical groundwater models were developed. A finite difference modeling system and a finite element modeling system. The grid covered an area with active cells covering 1.65 million km^2. A grid size of 10 x 10 km^2 was used for the finite difference scheme and in the finite element scheme the area of triangles ranged from 10 to 100 km^2.

Translating the physical system:

Using a deterministic, physically based numerical model a modeler is faced with the problem of considering important properties of the bedrock material. Especially in fractured and folded hard rocks this is challenging.
Local scale groundwater flow models in fractured material usually account for flow path geometry and fracture properties in detail. This can be achieved by so called Discrete Fractured Network models (DFN). But by the ability to extrapolate properties from small scales to larger regions, by data available on fractures as well as by a associated large computing power required for large regions this model approach is inappropriate for large scale modeling. Dual Porosity models, Channel Network models and stochastic models are also often used in small scale investigations. A comparison of these modeling approaches is given by *Selroos et al.* (2002).
Usually numerical groundwater models on the regional scale use a simplification for rock properties, by assuming that fractured material can be treated as a equivalent continuous porous medium, the so called Equivalent Porous Media (EPM) approach. Therefore a numerical model requires definition of the effective values of transmissivity or hydraulic conductivity in steady-state solution and the storage coefficient and porosity in transient solution (*Kresic*, 2006). Even highly karstified aquifers can sometimes be numerically modeled, using the EPM approach to simulate hydraulic heads, groundwater fluxes and spring discharges, but often fail to predict information as flow direction, destination, and velocity (e.g. *Scanlon et al.* (2003)).

Michael & Voss (2009) carried out three different approaches for the estimation of equivalent hydrogeologic parameters using three different types of data in the Bengal Basin of India and Bangladesh (200,000 km^2). By inverse modeling using transient hydraulic head measurements, by manually calibrating a steady state model by the use of groundwater age estimates from ^{14}C measurements and by the analysis of the lithology using driller logs which allowed a regionalization of hydraulic parameters by statistical analysis. All three approaches resulted in similar parameter value estimates.
Examples for large scale groundwater flow modeling using the EPM approach are given by *Massuel et al.* (2007); *Ophori* (2007); *Klock* (2001); *Schmidt & Plöthner* (1999) and are briefly summarized below.
In practice hydraulic properties are usually derived from pumping tests but in fractured media it is very difficult to extrapolate them to the scale of the grid size of the regional model. Therefore recharge, rather than transmissivity or hydraulic conductivity is used as an independent variable during regional steady-state model calibration and in transient model, temporal distribution of recharge in place of storage coefficient and porosity (*Lubcynski*, 1997). This is challenging in arid and semi-arid regions, because groundwater recharge in such areas is often only possible in consequence of temporal or spatial concentration of rainfall events or runoff, i.e. if the rainfall amount is higher than the evaporation and may not occur annually (*Külls*, 2000). Until the mid 1970s it was assumed that in Namibia direct groundwater recharge is not possible in areas like the Swakop River basin. However, following investigations using tritium and groundwater level fluctuation observations clearly indicated direct groundwater recharge (e.g. *Foster et al.* (1982); *Mazor* (1982)).
Since then, a large range of recharge rates were reported by several investigations and vary from 0.3 to 10 % of annual rainfall (e.g. *Mainardy* (1999); *Wrabel* (1999); *Külls* (2000); *Heynes* (1992)). *Heynes* (1992) obtained a recharge rate for the entire country of 1 % of annual rainfall. Due to the wide range of recharge values, point data can only represent regional features in a limited way. Therefore the recharge distribution within a large area plays an important role (*Klock*, 2001).

Another aspect, that should be considered by modeling large scale and deep groundwater flow is the decrease of permeability with depth, due to compaction, metamorphism, and/or filling of pore spaces and fractures by precipitating minerals. In the vertical direction the results of pumping- or slug-tests are also a opportunity to identify permeability at intermediate field scales but are in general not representative for larger scales as well. Therefore models are used to explore permeability distributions at large scales. (*Ingebritsen & Sanford*, 1998). Furthermore *Marklund* (2009) found, that the decreasing of permeability has a effect on near surface fluxes for topographic scales larger than 2 km.

Belcher (2004) used a function of exponential decrease of hydraulic conductivity (implemented as a feature of MODFLOW-2000 (*Harbaugh et al.*, 2000)) within the development of a 3D numerical transient ground water model of the Death Valley Regional Flow System (approximately 100,000 km^2), Nevada. The model represented Precambrian and Paleozoic crystalline and sedimentary rocks, Mesozoic sedimentary rocks, Mesozoic to Cenozoic intrusive rocks, Cenozoic volcanic tuffs and lavas, and late Cenozoic sedimentary deposits. These unconsolidated sediments and consolidated rocks were subdivided into 27 hydrogeologic units on the basis of lateral extent, physical characteristics, and structural features. The model was built up by a finite-difference grid consisting of 194 rows and 160 columns, and uniform cells 1500 m on each side for a total of 314,784 active cells. 16 layers ranging from 1 to more than 3000 m were implemented.
The assigned exponential decrease of hydraulic conductivity resulted in better model performances in all of the volcanic-rock units as well as in the basin fill sedimentary units and was less important in carbonate rock aquifers. *Carroll et al.* (2009) compared this model from *Belcher* (2004) with an unconfined groundwater model based on MODFLOW-SURFACT, which uses a pseudo-soil function for rigorous treatment of unconfined flow. In contrast MODFLOW 2000 assumes that saturated thickness remains constant throughout the entire simulation. *Carroll et al.* (2009) concluded that the unconfined MODFLOW-SURFACT model represents an evolution toward greater conceptual accuracy and improved stability.

The representation of small structures like alluvial aquifers is also challenging in large scale modeling with a in general associated large grid size.
Barthel et al. (2008) and *Wolf et al.* (2008) developed a groundwater flow model for the Upper Danube catchment (77,000 km^2 at gauge Passau, Germany) within the framework of the research project "GLOWA-Danube" using MODFLOW (*McDonald & Harbaugh*, 1988). The Decision Support System "DANUBIA" is comprised of 15 individual fully coupled models. To allow for appropriate calculation time and to facilitate data exchange the spatial discretization of such systems must be relatively coarse. The aim was to achieve a connected aquifer system, which is able to receive the groundwater recharge in the mountainous areas and yielding a reasonable base flow at gauging stations in the forelands. In order to implement narrow and highly permeable alluvial aquifers into the coarse finite difference grid among others the hydraulic properties of the alluvial aquifer cells were calculated by using the arithmetic mean.

Examples:

Massuel et al. (2007) simulated groundwater flow of the Musi catchment, India (11,000km^2, grid size 1 km^2) using MODFLOW 2000 (*Harbaugh et al.*, 2000) and the EPM approach. Two layers were implemented to describe weathered granites and fractured weathered granites (with a thickness of 15 and 20 m, respectively). Predicting the potential of renewable storage that could be further used in water allocation models was the aim of this study. By using a water table fluctuation method the aquifer seasonal and annual storage variations had been estimated for each year. Calibration was done by inverse modeling of groundwater levels and minimizing the root mean square error by tuning total recharge, permeability and storativity. The modeling results gave an overview of the basins water budget.

Ophori (2007) developed a large scale groundwater flow model for the Niger Delta (75,000km^2), Nigeria to evaluate any possible trends that may exist between groundwater and hydrocarbon movement and -accumulation in the basin. In the study area a tertiary sequence of three formations had been admitted. These formation were conceptualized by assuming the deepest formation consisting of a shale unit as impermeable, and by considering the other two overlying formations as separated and homogeneous EPM layers of sediments. Due to the objectives of the modeling study, the model scale and the high frequency and distribution of geologic structures the EPM approach was considered to be adequate, despite the extensive and densely distributed series of growth faults and accompanying rollover anticlines. The geometry consists of 70 rows and 44 columns that were 5 km x 5 km in size. By assuming that average discharge equals the recharge rate of 750 mm (independently estimated) the hydraulic conductivity of the top layer (because of the lack of deeper layer data) was adjusted until discharge was close to 750 mm. Results indicate, that due to topographic properties no regional flow system exits, local flow systems prevail and the basin could be characterized as a shallow basin. This was confirmed by particle tracking, which illustrated favorable flow systems and a discharge zone that occurred within a known oil-rich belt.

Schmidt & Plöthner (1999) used the results of hydrological interpretations of data derived from several groundwater studies conducted in the Otavi Mountains of Namibia to develop a three-dimensional groundwater model of the karst aquifer system for the period from 1978 to 1997. The heterogeneous hydrogeological composition of the area is build up by fractured dolomite with near surface karstification and by underlying meta sediments and basement rock types. In the conceptual model the fractured rock matrix was reproduced as a equivalent porous medium (EPM), due to analyses of observed groundwater level reactions and the appraisal of the general hyrogeological situation on the regional scale. The aquifer system was categorized into fourteen hydrogeological units, which represented either aquifers, aquitards or aquicludes according to their horizontal and vertical hydraulic conductivities. A horizontal grid size of 1000 km^2 was used. Through a narrow vertical discretization hydraulic conductivity contrasts between the upper and lower zones were considered. The regional model assumed a area-wide precipitation distribution and a effective recharge duration within a rainy season of one month. Calculated recharge factors varied between 1.3% (7 mm) and 5% (28 mm) of the mean annual rainfall.

Klock (2001) set up a simple groundwater flow model using ProcessingMODFLOW for basic understanding of the hydrogeological system and for inverse determination of groundwater recharge rates of the Kalahari in northeastern Namibia. The model consists of 179 active cells with a grid size of 26 km x 28 km (a total area of 130,312 km^2). It has been assumed that the groundwater system is in equilibrium, so a steady state simulation was performed. The aquifer system has been modeled as a single layer with weighted kf-values corresponding to the thickness of each formation. A kf-multiplier raster was introduced in areas where basalts occurred, due to high hydraulic conductivities at basalt sandstone interfaces. A initial basin wide recharge value of 1 mm/a was used. A maximum kf approach was performed by multiplying initial kf values by a kf multiplier. In a second step the minimum basin wide recharge was estimated by looking on the recharge amount that the basin allowed by neglecting additional groundwater flow in the basalt sandstone interfaces. Minimum basin wide recharge volume was
$5.4 \cdot 10^6 m^3/a$ and for the maximum approach $1.2 \cdot 10^8 m^3/a$.
Nevertheless, *Klock* (2001) stated that the resolution was to course and data availability to spare for a detailed modeling (e.g. unconformities between formations could not be respected) therefore the shape of the groundwater surface only could be reproduced with the introduction of a kf multiplier raster.

1.2 Objectives

The primary objective of the thesis is to develop an initial understanding of the groundwater flow pattern, i.e. the research questions focus on the different regions of groundwater flow paths and possible interactions between surface and groundwater hydrology. Due to literature review the attempt is made to represent various processes by a distributed large scale steady state model, using a numerical finite difference scheme for flow equations and mass balance, that can handle saturated and unsaturated conditions (MODFLOW-SURFACT (*HydrogeologicInc.*, 2007)) and the Equivalent Porous Medium approach. Because of the versatile, fractured and folded lithology as well as the size of the basin a grid size of 1 km^2 will be used. Furthermore, a exponential decrease of hydraulic conductivity will be implemented. Since lack of detailed basin wide information about hydraulic properties of the bedrock material, two approaches will be used with fixed recharge rates of 0.5 and 1% of annual rainfall, denoted as minimum and maximum approach, respectively. Different concepts will be developed, while increasing complexity according to climatical and lithological characteristics of the basin.

The aims of the thesis are:

- The representation of the groundwater flow pattern
- The determination of recharge and discharge zones
- The ascertainment of potential direct recharge rates, consistent to the basin geology
- The investigation of potential interactions between alluvial aquifers and the basement rocks

Chapter 2

Methodology

In this chapter tools and methods used to achieve the objectives of the thesis are described.

2.1 Numerical modeling

The graphical user interface Groundwater Vistas (GV) (*Rumbaugh & Rumbaugh*, 2007), which couples a model design system with graphical analysis tools as well as the flow and transport model MODFLOW SURFACT (*HydrogeologicInc.*, 2007) are used in this thesis.
MODFLOW SURFACT is a fully integrated flow and transport numeric code based on the USGS finite difference groundwater model MODFLOW (*McDonald & Harbaugh*, 1988). SURFACT´s modified BCF4 (Block Centered Flow) package performs a complex saturated-unsaturated subsurface flow analysis by using a pseudo-soil function for rigorous treatment of unconfined flow (*HydrogeologicInc.*, 2007).

2.1.1 Numerical model description

Groundwater flows either laminar or turbulent depending on the ratio of inertial forces to viscous forces of the water flow (i.e. with a Reynolds number ¡2000 water moves laminar). The flow direction is controlled by the hydraulic gradient. According to Darcy´s Law groundwater moves laminar:

$$\frac{Q}{A} = v = -k\frac{\delta h}{\delta l} \tag{2.1}$$

where Q[L^3/T] is the water flow, A [L^2] is the cross-section area of the medium, v [L/T] is the velocity, h is the hydraulic potential or hydraulic head [L]), l [L] the distance. Elevation, velocity head and pressure head affect the hydraulic head. Energy head from velocity is often negligible and the fluid is assumed incompressible so the potential becomes:

$$h = z + \frac{p}{\rho g} \tag{2.2}$$

where z [L] is the elevation, p [M/L/T^2] is the pressure, $\rho[M/L^3]$ is the density of water, and g [L/T^2] is the earth´s gravitational acceleration constant.
Properties of fluid and the medium affect the hydraulic conductivity:

$$k = K\frac{\rho g}{\eta} \tag{2.3}$$

where K [m^2] is the permeability of the medium and $\eta[kg/(s{\cdot}m]$ the dynamic viscosity of water (*Maidment*, 1993). So gravity is the main driving force and topography and geology define the effects of gravity on groundwater flow.
Based on mass conservation and Darcy´s law, MODFLOW SURFACT represents groundwater flow in three dimensions for an unconfined aquifer in variable saturated porous media as follows (*Huyakorn*, 1986):

$$\frac{\partial}{\partial x}(k_{xx}k_{rw}\frac{\partial h}{\partial x}) + \frac{\partial}{\partial y}(k_{yy}k_{rw}\frac{\partial h}{\partial y}) + \frac{\partial}{\partial z}(k_{zz}k_{rw}\frac{\partial h}{\partial z}) - G = \Phi\frac{\partial S}{\partial t} + S_w S_S\frac{\partial h}{\partial t} \tag{2.4}$$

where k_x, k_y, k_z [LT^{-1}] are the hydraulic conductivities along the x, y and z coordinates and h[L] is the hydraulic. G [$\frac{1}{T}$] is a volumetric source/sink term, S is storativity [dimensionless], b is saturated thickness [L] and t is time [T].
This equation includes additional terms relative to the equation used in MODFLOW (see *McDonald & Harbaugh* (1988)), these are:
$k_r w$ equal to relative permeability (a function of water saturation, dimensionless), ϕ equal to a drainable porosity (i.e. specific yield S_y) and S_w representing the degree of water saturation (a function of pressure head, dimensionless). When fully saturated conditions exist, then S_w=1.0, k_{rw}1.0 and Equation 2.4 reduces to the confined groundwater equation used by MODFLOW.
Furthermore MODFLOW´s HUF2 package (Hydrologic Unit Flow) uses the harmonic mean for computing effective interblock transmissivity (i.e. harmonic mean of transmissivity between a cell i and a cell j, defined as T_{ij} = 2-$T_iT_j/(T_i$+T_j)).
The effective transmissivity is equal to the saturated hydraulic conductivity multiplied by the saturated block thickness. The saturated thickness is equal to cell thickness (b), for confined systems. The harmonic mean removes the impacts of large outliers, aggregates smaller values and is best used to average fluxes. This estimation automatically

underestimates the equivalent interblock conductivity by biasing toward the lower block value, and in the extreme case never allows a desaturated block (i.e.saturated thickness of zero) to resaturate.

SURFACT´s BCF4 package computes interblock conductance as a product of the weighted harmonic mean of block saturated hydraulic conductivities (k_{xx}, k_{yy}, k_{zz}), relative permeability (k_{rw}), and mean flow area. Compared to MODFLOW´s unconfined solution (where the storage coefficient S s replaced by the specific yield S_y) the SURFACT approach to interblock conductance is more stable, does not bias toward the lower block value and does not inactivate dry cells during desaturation (*Carroll et al.*, 2009).

As aforementioned, the MODFLOW code generates a system of equations describing the groundwater flow system in a finite difference form. Within the program this set of algebraic equations can be solved by the use of the Slice Over-Relaxation- (SSOR), a Strongly Implicit Procedure- (SIP) or the Preconditioned Conjugate Gradient- 2 and 4 (PCG2, PCG4) methods. In the thesis the PCG4 package will be used. Furthermore the new Recharge-Seepage Face Boundary (RSF4) condition package of SURFACT allows the supplied recharge into the groundwater system if the water is below a user prescribed pool (ponding) elevation. The simulation allows only as much recharge to occur to maintain the prescribed pool conditions, if the water table reaches the pool elevation. The remaining recharge is not accepted into the simulation domain and equal to surface runoff. The output express this reduction in volumetric recharge flux [L^3/T] to the system following from the system saturating up to the ponding height. The Recharge package (RCH1) of MODFLOW provides the supplied recharge to the aquifer (as in confined systems) with heads continually rising above the ground surface, due to neglecting surface runoff (*HydrogeologicInc.*, 2007).

2.2 The Equivalent Porous Medium approach

Usually three vertical zones are distinguished in an hard rock environment. An upper or weathered zone characterized by regolith, colluvium and talus, side by side with alluvial, fluvial, glacial and lacustrine deposits with intergranular porosity prevailing.

An middle fractured zone with depth between tens to hundreds of meters. Here permeabilities generally decreasing with depth, due to the dependence of fracture aperture on exogenous geologic processes. At last a deep or massive zone with relatively scarce fracture and fault zones. Inhomogeneities in the deep or massive zone, in general due to light fracture apertures may form interconnected networks facilitating enhanced regional to continental groundwater flow (*Krasny & Sharp*, 2007).

Since it is very difficult to account for all properties of faulted, weathered and fractured

rocks (e.g. fracture network geometry) especially in large scale models the subsurface is often assumed to be a equivalent porous media. This approach is known as the Equivalent Porous Medium approach (EPM). In practice hydraulic parameters are usually derived from aquifer pumping tests but in fractured media it is very difficult to extrapolate them to the scale of the grid size of the regional model. Therefore recharge, rather than transmissivity/hydraulic conductivity is used as an independent variable during regional steady-state model calibration and in transient model, temporal distribution of recharge (if available) in place of storage coefficient and porosity (*Lubcynski*, 1997).
Effective porosity is defined as the ratio of void space that is available for groundwater flow, i.e. void spaces used by adhesive and capillary water excluded. In fractured medium effective porosity depends in part on fracture frequencies, orientations and apertures. Also it was found that effective porosity is a dynamic parameter that depends on fluid velocity and fluid or tracer molecular size. Furthermore, a fractured material can have a lower effective porosity than an unfractured one of the same material. This arises from the dominant effect that even small fractures can have on groundwater flow. The continuity of fractures profoundly effects the effective porosity. Is the fractured material treated as a porous continuum, the equivalent continuum effective porosity is estimated as the volumetric fraction of fracture void space contributing to flow per bulk volume of rock, i.e. interconnected matrix void space is neglected. Due to the low matrix permeability compared to the fractured permeability, matrix void space may not substantially contribute to groundwater flow and advective contaminant transport (*Gordon*, 1986).
In principle the EPM has some limitations. Only a cell size much bigger than the fracture spacing should be used. Besides, the fracture network must be interconnected and rather uniformly distributed within zones of equal density, when dealing with contaminant fate and transport analysis where all field scales are equally important (*Kresic*, 2006).

2.3 Depth dependence of permeability

The permeability, K [L^2], is a important material property describing a material´s capability to transmit fluids. It is the most relevant parameter in geological porous media flow. Often ranging over more than 15 orders of magnitude in geological materials and thus it can be highly anisotropic and inhomogeneous.
Measurements of permeability in laboratory settings may not reflect field scale, neglecting larger representative elementary volumes, which include large-scale fractures or layers . Especially the large scale permeability distributions affect numerous processes like regional flow patterns and long term water management (*Saar & Magna*, 2004). It is useful or even necessary to use analytical or numerical models to explore permeability

distributions at large scales.
Usually K decreases with depth, because of compaction, metamorphism, and/or filling of pore spaces and fractures by precipitating minerals (*Ingebritsen & Manning*, 1999; *Ingebritsen & Sanford*, 1998). To describe the non linear decrease of permeability with depth, mathematical representations are used: *Ingebritsen & Manning* (1999) describe the relation between depth and permeability by a power-law function (Equation 2.5), which was afterwards refined, suggesting to be exponential for the top 800 meters of depth by *Saar & Magna* (2004). Equation 2.6 was developed in the Oregon Cascades (Oregon, U.S.A.), a volcanic range located along an active, convergent plate boundary. Equation 2.7 was found based on swedish borehole data (Rehn et al (1999) in *Marklund* (2009)) and Equation 2.8 is implemented in MODFLOW-2000 (*Anderman & Hill*, 2003).

$$K(z) = K_D(\frac{-z}{D})^{-\gamma} \tag{2.5}$$

$$k(z) = k_0 e^{\frac{-z}{\delta}} \tag{2.6}$$

$$k(z) = k_0 e^{cz} \tag{2.7}$$

$$k(z) = k_0 \cdot 10^{-\lambda d} \tag{2.8}$$

K_S [L^2] is the permeability at the ground surface, K_D [L^2] the permeability at some depth. D, δ, γ and λ [L] are decay coefficients. k_0 L/T]) is the hydraulic conductivity at the ground surface, z [L]) is elevation, and c is a positive constant.
Ingebritsen & Manning (1999) recommended following values to represent the continental crust: K_D= 10^{-14} m^2 , D= 1000 m, γ= 3,2 m. *Saar & Magna* (2004) give conformable values: K_S= $5{\cdot}10^{-13}$ m^2 and δ= 250 m.
Over 3000m of depth Equation 2.8 by *ITCorporation* (1996) results in a conductivity of 50% with λ=$1{\cdot}10^{-4}$ (green line in Figure 2.1), and in 0.1% of the surface value with λ=$1{\cdot}10^{-3}$.
Values of c and k_0 fitted to borehole data from Sweden down to approximately 1600 m are 0.00641 and $1.925{\cdot}10^{-7}$ m^2, respectively. Each of these functions has limitations and advantages. For example Equation 2.6 by *Saar & Magna* (2004) tends to provide unrealistic low permeabilities at depth greater than about 2 km and reasonable near surface magnitudes. On the other hand the power law function (Equation 2.5 by *Ingebritsen & Manning* (1999)) gives realistic values at greater depth but converges infinity for $z{\to}0$ and is not defined for z=0 (*Saar & Magna*, 2004).
In this thesis the equation of (*Saar & Magna*, 2004) will be used with the reported decay coefficient (δ= 250 m) , because of the lack of information about the decay of hydraulic conductivity in the study area, and because literature review about the equation found in Sweden by Rehn et al. (1999) failed, except for a citation in *Marklund* (2009).

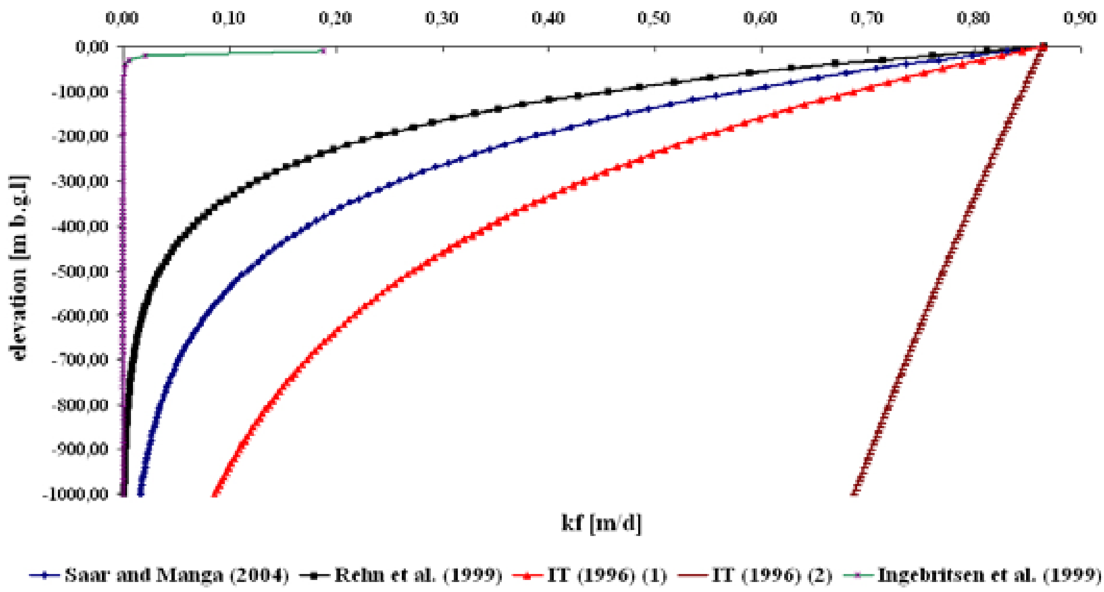

FIGURE 2.1: Various models for the depth dependence of hydraulic conductivity

2.3.1 The influence of temperature on hydraulic conductivity

The hydraulic conductivity defined by Equation 2.3 actually contains an viscosity dependent term $\tau = \rho g \eta^{-1}$. Using the kf-value in groundwater investigations, this term may be treated as a constant (about $7.5 \cdot 10^6$) at a temperature of 10 °C and a density of 1000 kg/m^3.

Dynamic viscosity of water has a strong dependence on temperature. It can be calculated directly from temperature using the Poiseulle relationship (Equation 2.9)(Stelczer, 1987 in (*Gordon et al.*, 2004)):

$$\eta = \frac{1,78 \cdot 10^{-3}}{(1 + 0,0337T + 0,000221T^2)}[\frac{kg}{ms}] \tag{2.9}$$

Table A.1 in appendix A and Figure 2.2 illustrate the effect of temperature on hydraulic conductivity. The gray line in Figure 2.2 shows the depth dependence of hydraulic conductivity using Equation 2.6 by *Saar & Magna* (2004) for a near surface permeability K_0= 1,03$\cdot 10^{-12}$ m^2, a near surface water temperature of T=20 °C, a density of 1000 kgm$^-3$ as well as a temperature gradient of ∂T/∂z= 3°C/100m. The decrease of hydraulic conductivity with depth by neglecting temperature and density is indicated by the black line. Values are listed in appendix A (Table A.1).

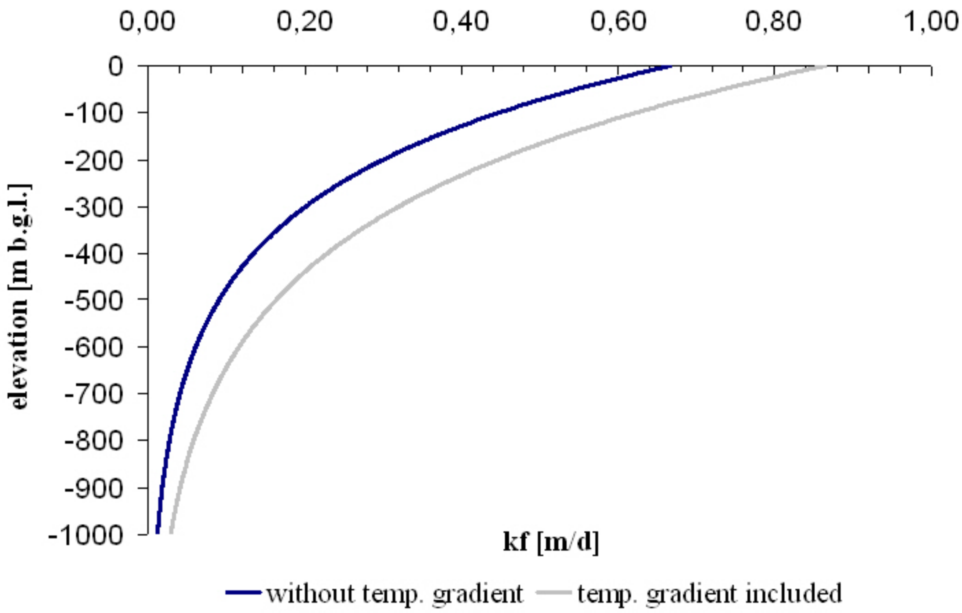

Figure 2.2: Relation between depth-decaying of hydraulic conductivity and temperature

For calculations in multi-phase systems or geothermal systems with different temperatures and different viscosities the permeability has to be used. Since the differences between the values in Figure 2.2 is marginal to other uncertainties (e.g. the decrease of permeability with depth) the influence of temperature and density on hydraulic conductivity will not be considered in this thesis.

2.4 Pre- and post-processing

Spatial data, such as digital elevation, geology, recharge and evaporation and borehole information, were manipulated using ArcMap 9.3 (*ESRI*, 2008) and were converted into matrix or shape files and imported into Groundwater Vistas (*Rumbaugh & Rumbaugh*, 2007).

2.5 Model calibration

Model calibration will be done by trail and error procedure by fitting simulated to observed groundwater levels derived from the GROWAS borehole database (*DWA*, 2004). As a measure of the deviation between simulated and observed groundwater heads the Root Mean Square Error (RMS) (Equation 2.11) and the Mean Absolute Error (MAE) (Equation 2.12 will be used. Residuals are defined as (Equation 2.10):

$$Residual = (h_{o,j} - h_{s,j}) \tag{2.10}$$

$$RMS = \sqrt{\frac{1}{n}\sum_{j}^{n}((h_{o,j} - h_{s,j})^2}, \in [0; \infty] \tag{2.11}$$

$$MAE = \frac{1}{n}(\sum_{j}^{n} |h_{o,j} - h_{s,j}|), \in [0; \infty] \tag{2.12}$$

2.6 Basement-water indicators

In chapter 5.5 mass balances of different river compartments were calculated. For the determination of basement water influence on these river sections four indicators (I) will be used.

1. $$I1 = \frac{TotalIn - Rch}{TotalIn} \tag{2.13}$$

   A measure for the water amount that enters the compartment from the subsurface (vertical and lateral).

2. $$I2 = \frac{BottomIn}{TotalIn} \tag{2.14}$$

   A measure for the fraction of basement water inflow on total inputs.

3. $$I3 = \frac{BottomIn}{TotalIn - Rch} \tag{2.15}$$

   A measure for the ratio of vertical basement inflow on total basement inflow.

4. $$I4 = \frac{ET}{TotalIn} \tag{2.16}$$

   A measure for the influence of evaporation.

Chapter 3

Study area

3.1 Overview

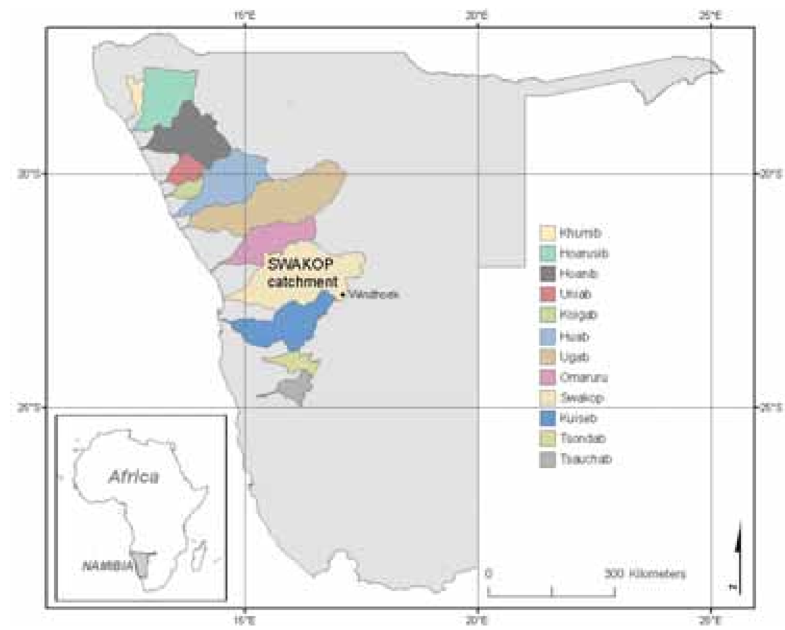

FIGURE 3.1: Location of Namibia in Africa and the country´s western catchments (Marx, V., 2009 modified from Jacobson et al.,1995)

The westward draining Swakop River catchment with an area of 30,100 km^2 is the largest catchment within Namibia and the one with the most developed infrastructure. It stretches from the Atlantic Ocean to the east and is bordered by the Kuiseb River catchment in the south and the Omaruru River catchment in the north (Figure 3.1 (*CSIR*, 1997).

The elevation varies from sea level to about 2400 m a.s.l. in the Khomas Highland. Located in the catchment are numerous towns like Okahandja, Otjimbingwe, Karibib, Usakos and the capital Windhoek. Several farms and mines, Rössing uranium mine, Langer Heinrich uranium mine and the gold mine Navachab are also situated in the study area. In the upper part of the catchment the Von Bach and the Swakoppoort Dam together with a third dam located in the northern neighboring Omatako catchment constitute an interconnected system and allocate considerable amount of water to the region. Figure 3.2 gives elevation information and depicts prominent features.

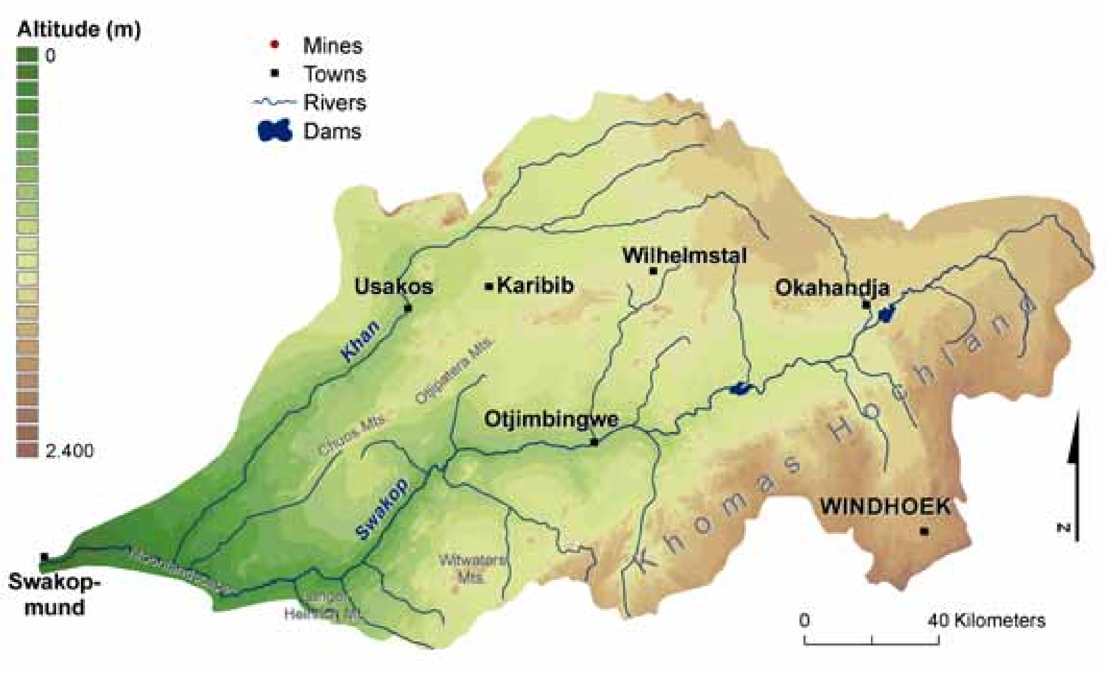

FIGURE 3.2: Elevation information and prominent features (modified from *DEA* (2002))

3.2 Climate

Low annual rainfall, relatively high temperatures during the rainy season and huge evaporation losses cause an almost continuous water deficit, Namibia´s climate can be classified as dry according to the Köppen climate classification. A nearly permanent temperature inversion at the coast caused by cold Atlantic sea water (Benguela current) leads to the extreme aridity of the Namib desert. Rainfall events are variable, unreliable and unevenly distributed in space and time. There is a steep rainfall gradient from east to west with most precipitation falling as showers or thunderstorms in summer between October and May. The variability of rainfall increases with aridity toward the Atlantic sea. Annual rainfall varies from 0-50 mm at the coast and up to 450 mm in the interior regions (*Christelis & Struckmeier*, 2001). High moisture conditions in the coastal area lead to common fog formation, which is an important water supply for the adapted fauna and flora in the Namib desert. Fog precipitation can exceed three to four times the annual precipitation (*Jacobson et al.*, 1995).

Mean annual potential evaporation is around 3000 mm a year, up to 3400 mm in the center and less than 2400 mm at the coast (*DEA*, 2002). Thus water is rapidly lost from ecosystems and surface water storages (e.g. dams).

Average minimum temperatures range from 10 - 12°C at the coast and from 4 - 6°C in Windhoek and average maximum temperatures are 20 - 22 °C at the coast and around 30 - 32 °C in Windhoek (*DEA*, 2002).

3.3 Soils and Vegetation

Due to the arid climate and the relatively slow rates of weathering, soils are generally thin and poorly developed. Thus they are often very rocky and frequently giving way to the bare rock beneath. Close to the coast dune fields consisting of littoral sands are located. Soils in the lower catchment are in general halomorphic, often associated with gypsum or salt deposits. The thickest and most fertile soils can be found in major valleys, and originated from alluvial and colluvial deposits. However they are also often calcareous and saline and thus have as well limited potential for irrigated agriculture. Soils of floodplains, with a thickness of about 10 - 30 m, formed of deposits of sediments transported by floods of the ephemeral rivers, exist of sandy loams and sandy clay loams. These alluvial soils are composed of variantly layers of sand, silt, clay and gravels tributary upon the magnitude of individual floods and source materials (*Jacobson et al.*, 1995; *CSIR*, 1997). A map of major soil types in the basin is given in Figure 3.3.

The vegetation in the catchment is highly adapted to the climatic conditions and along the ephemeral rivers to the erratic and destructive nature of floods. Variation in species composition of plant communities is associated with the rainfall gradient, i.e. variation in rainfall is the primary determinant of vegetation. Riparian vegetation occurs along alluvial aquifers, due to soil deposition, soil moisture and groundwater storage.
Faidherbia albida (Ana tree), Tamarix (Tamarisk), Acacia erioloba (Camelthorn) and Prosopis glandulosa (Prosopis, an alien invasive plant) represent the Swakop riparian vegetation. In general four vegetation types according to Giess can by found in the catchment: Central Namib (9%), Semi-desert / Savanna Transition (34%), Thornbush Savanna (28%) and Highland Savanna (29%) (*Marx*, 2009; *Jacobson et al.*, 1995).

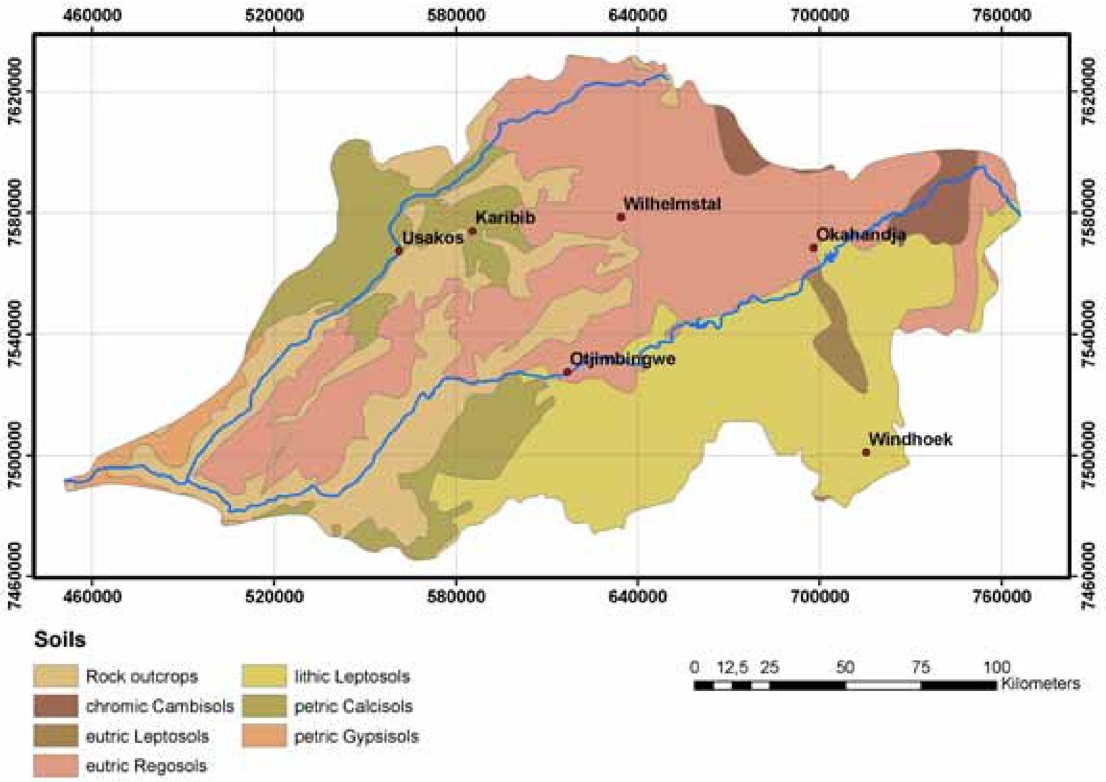

FIGURE 3.3: Soils within the Swakop River basin (*DEA*, 2002)

3.4 Surface water

The Swakop River and its tributary, the Khan River, are the biggest ephemeral streams in the Swakop river basin and important groundwater suppliers to several towns in the central area. Several smaller ephemeral tributaries are located in the catchment, some of them were also used for water supply in former times. The riverbeds of the westward-flowing Swakop and Khan rivers exist of sand, gravel and silt deposits with a general thickness between 10 and 30 meters. The hydrogeological map in Figure 3.9 displays high yields within the porous alluvial aquifers.
The river gradient of the Swakop River with an mean slope of 1:270 can be characterized as very constant and slightly convex over long sections, in contrast the average gradient of 1:182 is steep resulting in faster travel times and smaller transmission losses if equal conditions in both rivers would prevail. In general the rivers are following the strike of the bedrock formation and when cutting across the strike, the bedrocks form barriers that split up the alluvial aquifers into compartments (*CSIR*, 1997). The construction of the Von Bach and Swakoppoort dams upstream of Otjimmbingwe resulted in a rigorous change of water supply from the streams by the reduction of frequency and volume of floods (*Müller*, 2001). A description about the characteristics of the ephemeral system

and the alterations due to the construction of the two surface dams is given by *Marx* (2009).

3.5 Geology and hydrogeology

3.5.1 Overview

Numerous different processes and formation phases formed todays versatile landscapes of Namibia. Figure 3.4 illustrates the different tectonic settings. The oldest parts (more than 2 billion years) are build up by two primarily separated cratons, the Congo Craton in the north and the Kalahari Craton in the south east. Over million of years further mainlands joined those two cratons under orogenesis. During the first orogenesis the Epupa-, the Huab-, and the Grootfontein - complex were added to the Congo Craton and rocks, which formations are called Vaalian were formed.
In the following second big orogeny rocks of the Mokolian were generated, consisting of metamorphic erosion deposits from the Congo and Kalahari Cratons and from the ambient mountains of the Vaalian, which were sedimented in the Damara geosyncline. Approximately 900 million years ago tectonical plate procedures led to an convergence of the Congo and the Kalahari Cratons and a displacement of water from the Damara sea. Finally, about 650 - 500 million years before today the cratons clashed, the erosion deposits were raised and the Damara belt was generated. Numerous magma intrusives were crystallized in this southwest - northeast aligned range at the end of this folding process. At this point in time Pangaea was generated as well by the joining of Africa, South America, Australia, Antarctic, India and Madagascar.lia, Antarctic, India and Madagascar. Following the Damara Sequence, about 300 million years ago, an erosion-cycle in South Africa (Karoo Sequence) occurred. In this process the Damara range was weathered and eroded. The deposits were sedimented over the Kalahari Craton mainly to the south and south-east of the mountains and built up the so called Nama Formation. Because of the former adjacency to the South Pole inland glaciers covered Namibia during the Godwana ice age. About 280 million years ago, at the end of this ice age, large glacial deposits remained in southern Namibia, e.g. the Dwyka formation. Glacio-fluviatile sediments can be found preferentially in central Namibia, e.g. the Omingonde Formation, furthermore fluviatile deltasediments (Ecca-sediments) in the south and consolidated sandstones and quartzites from the Etjo-Formation in the north of the country.

At the end of the Karoo time, around 135 million years before today, the super continent Pangaea began to split up into northern hemispherical Laurasia and southern hemispherical Godwana involving further big magmatic eruptions, e.g the Etendeca basalts. The tertiary was characterized by erosion and sedimentation of the Kalahari sequence or rather Post-Karoo-Sequence and the genesis of the Namib-Erg took place as well. During the last million years aeolian and fluviatile forces formed the landscape (*Hueser et al.*, 2001; *Gruenert*, 2003; *Christelis & Struckmeier*, 2001).

Table 3.1: Stratigraphical units in Namibia (after *Christelis & Struckmeier* (2001))

Era	Formation	Namibian	Classification
Cenozoic < 65 Ma	Cretaceous to Quaternary < 135 Ma	< 135 Ma	Cenozoic Sediments
Mesozoic 65-250 Ma			Post-Karoo Complexes
	Permian to Jurassic 135-300 Ma	135-300 Ma	Karoo Sequence
Paleozoic 250-540 Ma			
	300-500 Ma	Erosion	
	Cambrian 500-540 Ma	Namibian to early Cambrian 500-1000 Ma	Nama Group Damara Group Gariep Complex
Precambrium > 540 Ma	Neoproterozoic 540-1000 Ma		
	Mesoproterozoic 1000-1600 Ma	Middle to late Mokolian 1000-1800 Ma	Gamsberg Granite Fransfontein Suite Sinclair Sequence Namaqualand Complex Rehoboth Sequence
	Paleoproterozoic and Archaean > 1600 Ma	Vaalian to early Mokolian > 1800 Ma	Elim Formation Khoabendus Group Vioolsdrif Suite Orange River Group Mooiriver Complex Neuhof Formation Hohewarte Complex Abbabis Complex Grootfontein Complex Huab Comblex Kunene Complex Epupa Complex

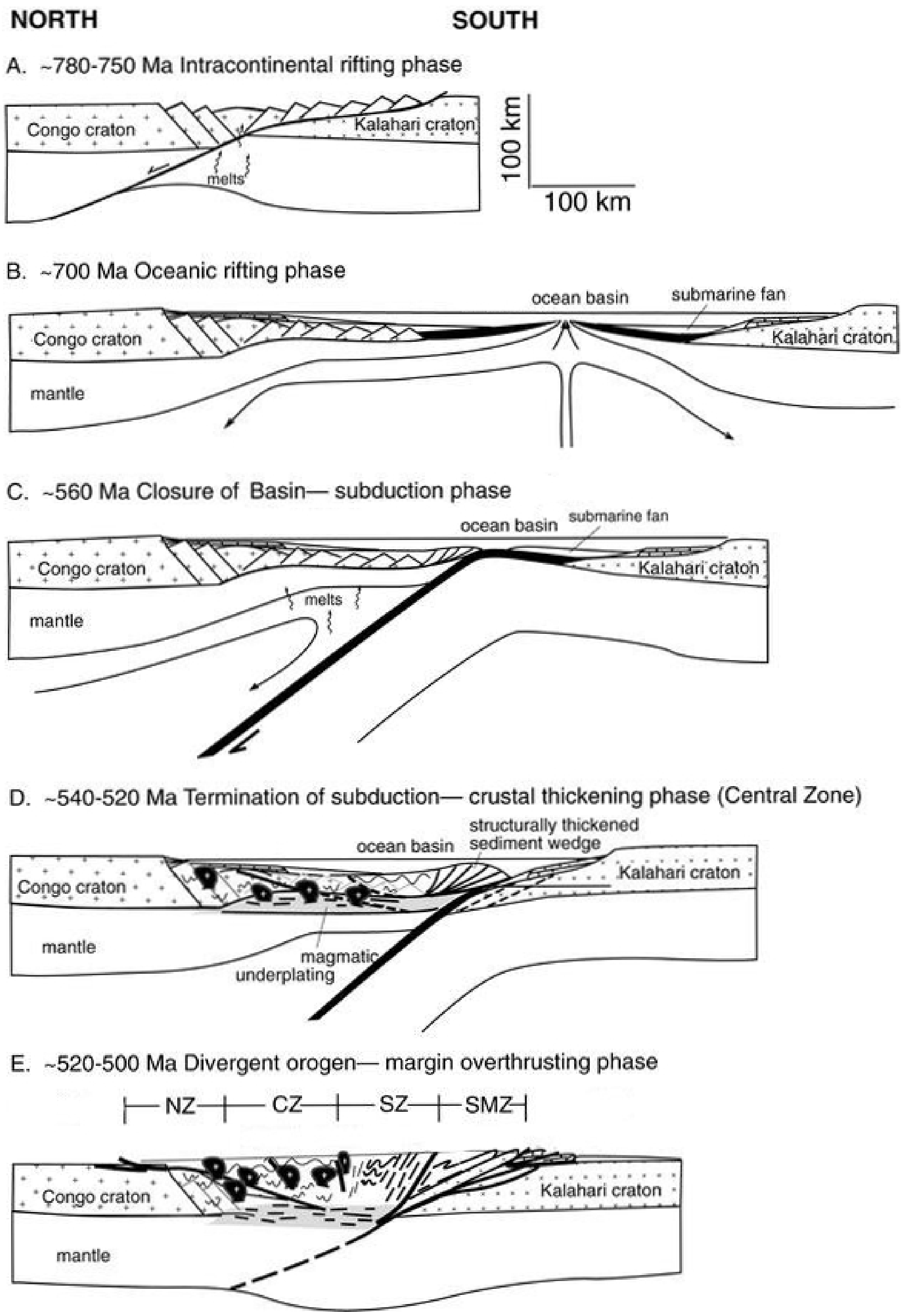

FIGURE 3.4: Tectonic settings of the Damara Orogen (modified after *GSA* (n.a.))

3.5.2 Geology

The Swakop River catchment is located within the Damara Orogen. The Damara Orogen in Namibia has been divided into a north-south trending coastal branch and a north-east trending inland branch, which has been interpreted as a result of the collision between the Congo, Kalahari and Rio de la Plata cratons (Stanistreet et al., 1991; Prave, 1996 in *Nex et al.* (2002)). *Miller* (1983) divided the inland branch into a number of zones based on lithostratigraphical, structural and metamorphic criteria (Figure 3.5 and 3.4. Faults or lineaments represent boundaries between different zones. The Swakop River catchments occurs in the Central Zone (CZ) (bounded by the Otjihorongo thrust in the north and the Okahandjia lineament in the south)and in the Southern Zone (SZ). In the strict sense the catchment occurs in the southern Central Zone (sCZ)(bounded by the Omaruru Lineament (OML) and the Okahandja Lineament (OL)), in the Okahandja Lineament Zone (OLZ) (the southern margin of the CZ) and in the Southern Zone (SZ). The geological map (1:1000000) (*DEA*, 2002) in Figure 3.8 gives an lithological overview and displays groups, major rock types and their age. Figure 3.6 illustrates the stratigraphic column, and in table 3.2 the stratigraphic units and associated lithologies are listed.

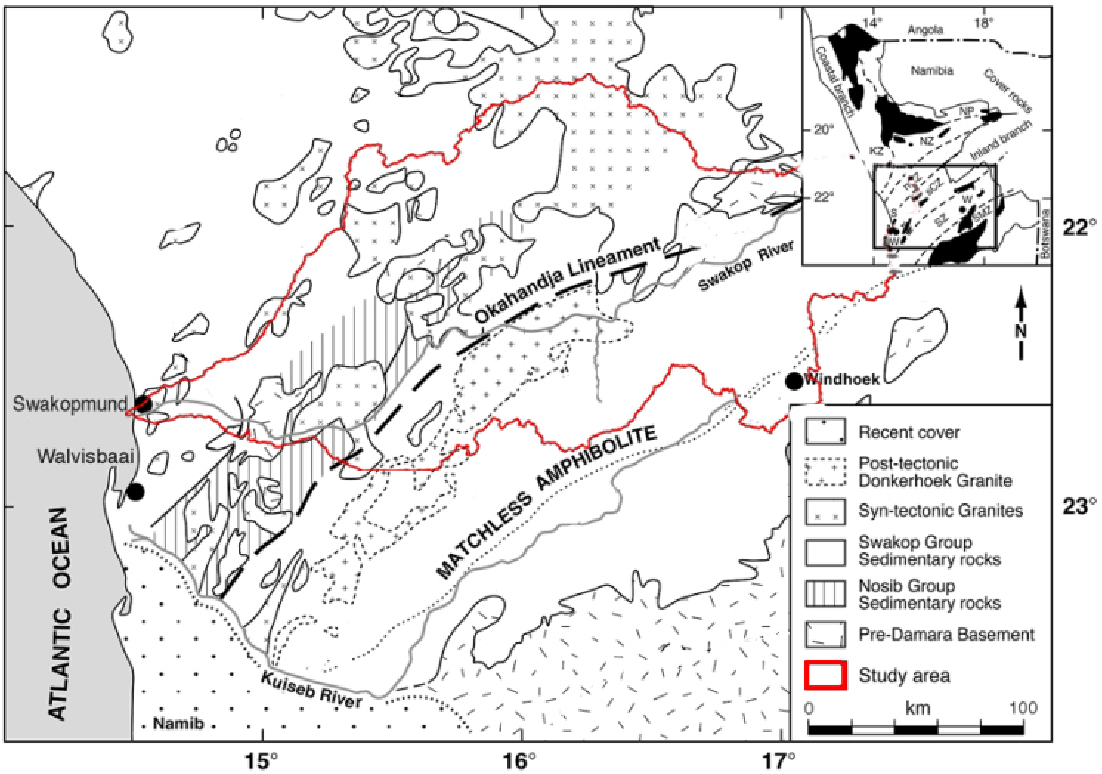

FIGURE 3.5: Generalized geological map of the central zone (modified, *Jung et al.* (1999) after *Miller* (1983)

As aforementioned, the central region, including the Swakop River basin, is dominated by the Damara Sequence. These rocks were liabled to extensive folding, faulting and erosion before being covered by sedimentary deposits, followed by another long time of erosion. The Great Escarpment in the catchment is not as pronounced as elsewhere in Namibia, mainly due to erosion caused by drainage of Swakop- and Khan River also Damaran rocks present here weather more readly than rocks forming the Great Escarpment elsewhere (*Schneider et al.*, 2008). As shown in Figure 3.6 quarzofelspathic biotite gneisses and schists with subordinate para- and ortho-amphibolites of the Precambrian Abbabis Formation compose the basement on which they were deposited (*Smith*, 1965). The overlying Damara Sequence (540-1000 Ma) comprises the Nosib and Swakop Groups, consisting of various metamorphic rock types and is subdivided with decreasing age into the Etusis, Khan, Rössing, Chuos, Arandis, Karibib, Tinkas and Kuiseb formations. Typical rock types of these formations are metasediments, marbles, dolomites, calc-silicate rocks, schists and gneisses.

The following Karoo Sequence with an age of 130 - 300 Ma is composed of Damaran granites, uraniferous alaskites and basalts as well as dolerites of the Etendeka Group. Aeolian sands and other surficial deposits (Table 3.2) represent the top in some areas. The OLZ and the SZ together form the Khomas trough (*Breitkopf & Maiden*, 1988) and both only comprise the Kuiseb Formation of the Swakop Group, distinguished by a thick sequence (almost 10000 m) of highly thrusted, high pressure, low temperature pelitic and graphitic schists (mica-schist, quartzite and meta-greywacke) with a southward vergence (*Nex et al.*, 2002; *Schneider et al.*, 2008; *Miller*, 1983).

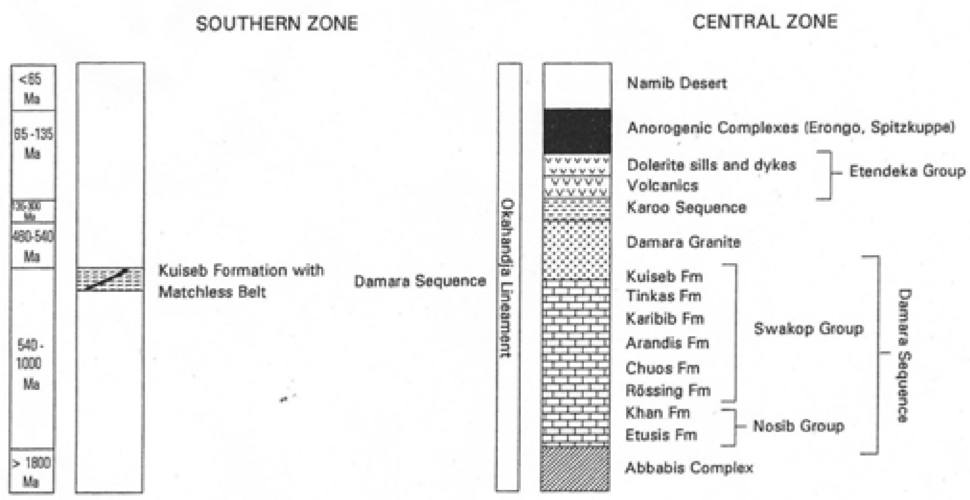

FIGURE 3.6: Stratigraphic column (*Schneider et al.*, 2008)

Toward the center of the trough a zone of graphitic schists units separates this sequence from the other half of the trough which is characterized by increasing proportions of schists with inter layered meta volcanic material concentrated along the so called "Matchless Amphibolit Belt". In total it has a SW-NE strike length of 350 km and ranges in thickness from 0,5 to 3 km, representing metamorphosed mafic volcanic and intrusive rocks (*Breitkopf & Maiden*, 1988). In the basin the Matchless Belt occurs with a length of about 50 km near Windhoek.
In the south of Windhoek well fractured sandstones of the Rehoboth Group (Paleoproterozoic age ca. 2200 to 1800 Ma) occur (not included in the stratigraphic column of the Central Zone).
Between Windhoek and Okahandja the prominent Windhoek Graben occurs. This fault system is characterized by individual, in relation to each other vertically displaced blocks along steeply dipping faults (Figure 3.7) and is characterized in the hydrogeological map (Figure 3.9) as a fractured aquifer with moderate to high yields.

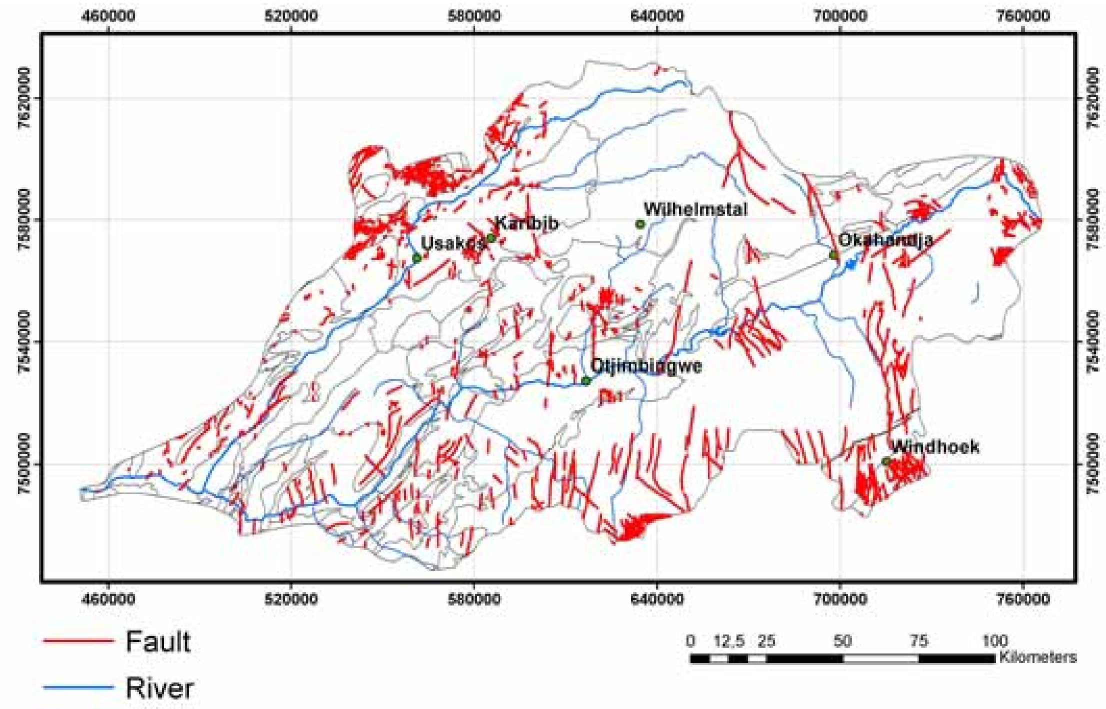

FIGURE 3.7: Faults in the Swakop River basin (*GSN*, n.a.)

The Okahandja Lineament separates the southern Central Zone from the Southern Zone (Figure 3.5). Here, alteration in the stratigraphic succession, in the degree of metamorphose and changes in seismic profiles occur (*Miller*, 1983; *Schneider et al.*, 2008; *Nagel*, 1999). The NE trending lineament itself is characterized by a vertical, isoclinal fault structure with upright layer-, shale- and shear zones and a thickness of about 500 - 2000 m (*Nagel*, 1999).

The sCZ is distinguished by high temperature, low pressure rocks. Here a large number of syn- to post-tectonic granite plutons, which have been intruded during the Damaran Orogeny (190-650 Ma) are located. Regional metamorphism and much of the deformation in the Damara Belt is related to two thermal events: First the mobilization of the basement and the lower parts of the Damara Sequence with related generation of syntectonic granites and secondly the emplacement of post-tectonic granite bodies toward the close of the Damara cycle.
Approximately 520 Ma ago the Donkerhoek batholith (a gray, garnet-bearing, two mica, post tectonic Damaran granite (Figure 3.5) disrupted and invaded the northern edges of the Khomas trough for nearly 200 km along the strike. The Ugab Subgroup is represented by the Rössing Formation in the areas immediately north of the Khomas trough. Marbles of the Karibib Formation of the Swakop Group can be found at Karibib and also mountains of triassic arkose of the Karoo Sequence, topped by hard Createaceus basalt. Near Karibib at the southern site of the Khan River mountains by quartzite and meta-arkose of the Etusis Formation are located. From Usakos onward Swakop Group meta-sediments become increasingly intruded by granite, alkasite and pegmatites. Some of alkasite carry uranium and are stooped in open cast uranium mines (*Schneider et al.*, 2008).
Highly metamorphosed rocks of the mesoproterozoic Abbabis Complex are exposed in some domes and antiforms within the basin. The Abbabis inlier is the largest of several small inliers of the basement, which are found in cores of domal structures draped by units of the Damara Sequence.
Toward the coast occurrence of dykes increase. These dolerite dykes form NE and less frequently EW trending dyke swarms, which cut through all the meta-sediments and intrusive rocks. They are related to the cretaceous Etendeka volcanism, which immediately preceded the break-up of the African-South American part of Godwana. Individual dykes range between 10 cm and several tens of meters wide, and often extend for many kilometers along the strike (*Schneider et al.*, 2008).

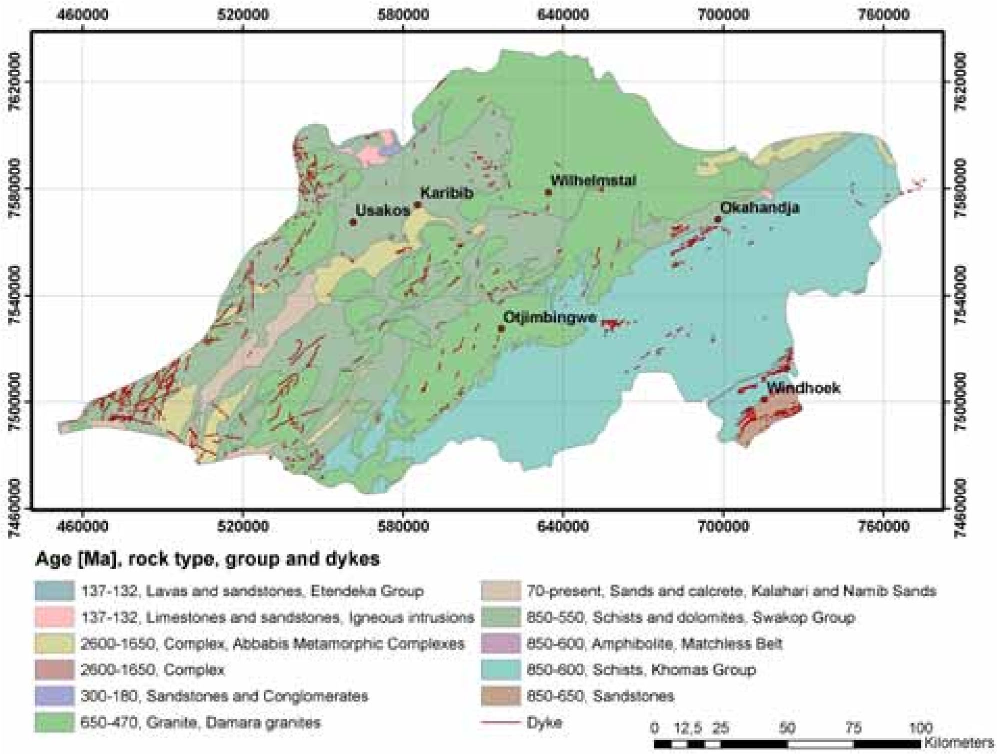

FIGURE 3.8: Geological map (1:1 mio) (*DEA*, 2002; *GSN*, n.a.)

TABLE 3.2: Stratigraphic succession of the Swakop River Basin

System	Sequence	Group	Subgroup	Formation	Max. thickness	Lithology
Quaternary, Tertiary		Namib				aeolian sand surficial deposits
Cretaceous, Jurassic, Triassic	Karoo (300-130 Ma)	Etendeka				basalt dolerite
Permian, Carboniferous, Devonian, Silurian Ordovician, Cambrian						alaskite (uraniferous) Damara granites
Namibian 540-1000 Ma	Damara	Swakop	Khomas	Kuiseb	> 3000 m	mica schist, metagreywacke, migmatite, quartzite (micaceous), calc-silicate rock, schist (graphitic) marble/dolomite,amphibolite
				Tinkas		mica schist, metagreywacke calc-silicate rock, quartzite (micaceous), marble, amphibolite
				Karibib	1000 m	marble, dolomite, limestone, calc-silicate rock, mica schist peltic and semi-peltic schist and gneiss, biotite amphibolite schist, quartz schist, migmatite
				Arandis		mica schist, para-amphibolite, metasediments, marble (impure), calc-silicate rock
				Chuos	700 m	diamictite, pebbly schist, calc-silicate rock, quartzite, marble (dolomitic), ferruginous quartzite
			Discordance			
			Ugab	Rossing	200 m	Marble, peltic schist and gneiss, biotite-hornblende schist, migmatite, calc-silicate rock, quartzite, metaconglomerat
			Discordance			
		Nosib		Khan	1100 m	calc-silicate rock, conglomerate, mica schist, amphibolite, migmatite, banded and mottled quartzofeldspathic clinopyroxene-amphibolite gneiss, hornblende-biotite schist, biotite schist and gneiss, migmatite,
				Etusis	3000 m	quartzite (feldspathic), meta-arkose, pelitic and semi-pelitic schist and gneiss, migmatite, quartzofeldspathic clinopyroxene-amphibolite gneiss, calc-silicate rock, metaphyolite.
		Major unconformity				
Mokolian > 1800 Ma		Abbabis Complex				quartzofeldspathic biotite gneiss and schist

3.5.3 Hydrogeology

Figure 3.9 shows a detail of the Hydrogeological Map of Namibia (1:1000000) (*DWA & GSN*, 2001) and the boundaries of the Swakop River basin (red line). The map presents a color scheme that subdivides the rock bodies into aquifer (blue, green) and non-aquifers (brown) and further into fractured (green) or porous (blue) ones. Dark blue and dark green illustrate aquifers with high potential and yields generally above 15 m^3/h, while the light colors describe aquifers with moderate potential and yields between 3 and 15 m^3/h. The map is based on informations from the GROWAS borehole database (*DWA*, 2004). The aquifer productivity data set, was created by analysis and spatial interpolation of the yield figures stored in the database. Further, the results of the data analysis exercise were discussed with local groundwater consultants (*Christelis & Struckmeier*, 2001).
The potential of bedrock-aquifers in the Swakop River catchment is very limited, because of low rainfall, lack of recharge and to some extend because of generally adverse aquifer properties of Damara Sequence rocks. Due to that fact most towns are situated on or near rivers and obtain their water by surface water storage in dams or from alluvial aquifers. High yielding bedrock properties can be found in the quartzite aquifer of the Windhoek area. Faults, generally north-south subvertical tension faults associated with the Windhoek Graben (Figure 3.7) present the major water conductors in this area and extend as a zone of moderate potential northward toward Okahandja. Here recharge takes place mainly by direct infiltration of rainwater over areas of quartzite outcrops, or in areas underlain by schist by direct recharge along fault zones. Water pumped from Windhoek boreholes has a mean age of approximately 12000 a. Deep groundwater circulation is assumed in fault zones some kilometers north of the main quartzite outcrops, due to the presence of strong flows of hot water. The mica schist with occasional quartzite intercalation, which are located in the Khomas Highland, have less recharge rates in the west of Windhoek , due to higher rainfall and thus enhanced chemical weathering, while joints and fractures in the east of Windhoek tend to be open. Mean borehole yields of about 2.4 m^3/h are in the east of Windhoek, 9 m^3/h in Windhoek and 2.9 m^3/h further west. Nevertheless borehole success rates and yields decrease toward the Namib. Subvertical pegmatite dykes parallel to the strike of the mica schist near Okahandja (Figure 3.8 present preferred drilling targets and have highest yields between 15 and 35 m below the water level. The marble and schist aquifers around Karibib and also the calcrete aquifer in the Kranzberg area at Usakos have moderate yields. Bedrock aquifers in the eastern part of the Namib have generally low but locally moderate yield potential. Low to limited yields are encountered in the Namib. Represented by orange hatching on the map, groundwater in fractured aquifers between the coast and 20 to 150 km inland is saline in most instances (*Müller*, 2001).

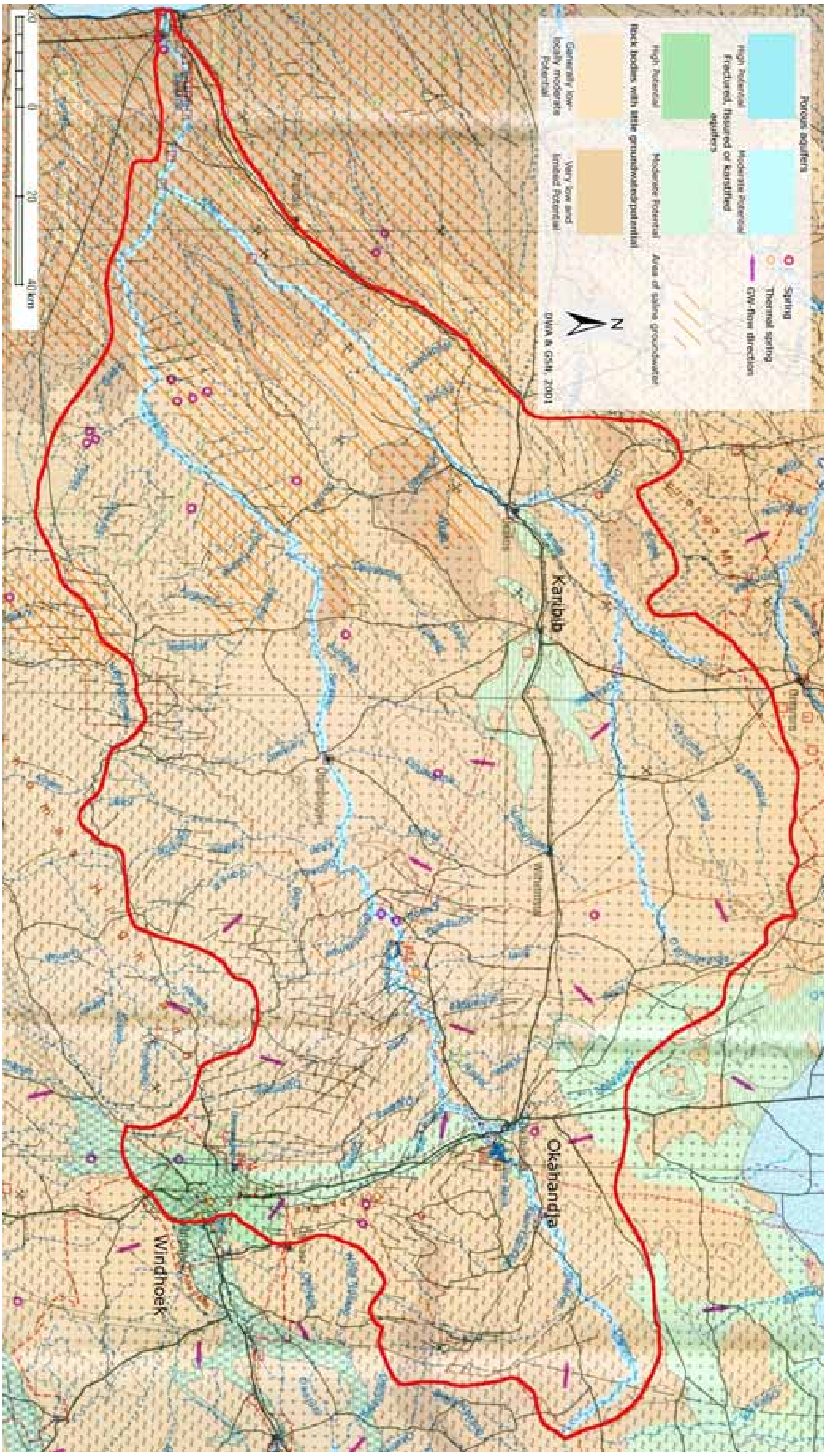

FIGURE 3.9: Hydrogeological Map (1:1 mio) (*DWA & GSN*, 2001)

Chapter 4

Model conceptualization

This chapter presents the model conceptualization for the study area, i.e. translating the physical system in one that can be modeled numerically. It includes the physical and hydrogeologic settings of the study area and the hydrologic factors that control groundwater flow. Special subjects implicated in this chapter are initial model parameter values, boundary conditions, and references to the source data. Model conceptualization was done in several steps while increasing complexity, i.e. the model was built up from simple to more detailed according to the translation of basin characteristics. Three different recharge and evaporation as well as two aquifer concepts were developed and combined in three modeling approaches. The results of different conceptualizations were interpreted to achieve improvements in the subsequent model conceptualization.
In Figure 4.1 fluxes considered in the conceptual model are demonstrated as well as the implemented layers and their thickness. It has been assumed that the groundwater system is in equilibrium and groundwater withdrawals have been neglected.

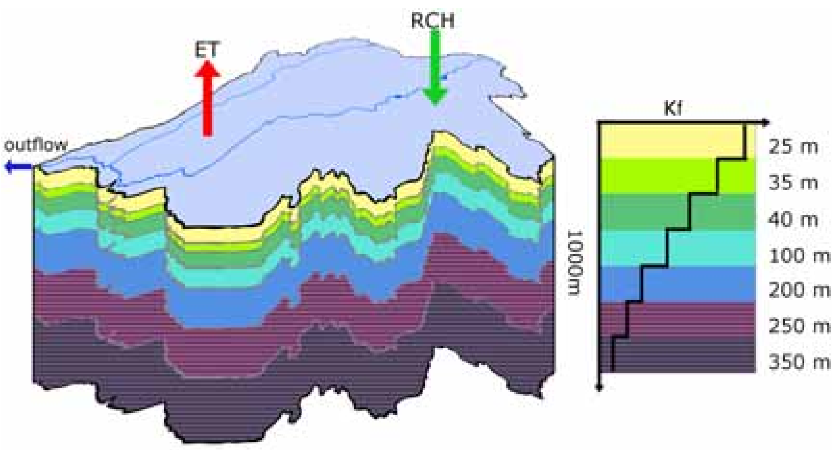

FIGURE 4.1: Fluxes and thickness of layers considered in the conceptual model

4.1 Topography

Land elevation data of the study area were derived from SRTM (Shuttle Radar Topography Mission provided by NASA) and used to represent the surface elevation in the model (Figure 4.2).

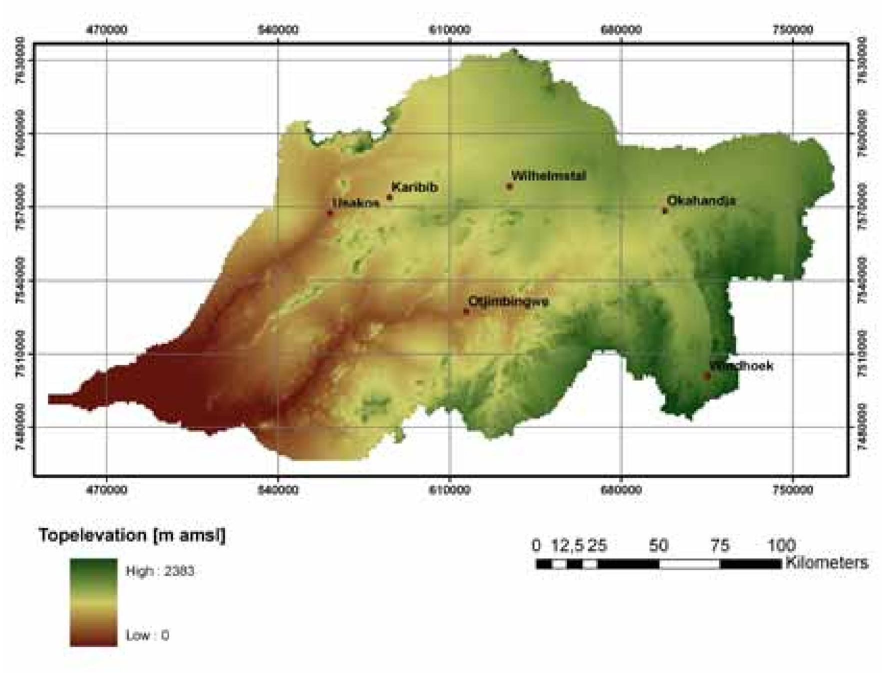

FIGURE 4.2: Topelevations of layer 1

4.2 Model boundaries and model resolution

The model area comprises the entire catchment of the Swakop River. It was assumed that surface and subsurface catchment equal each other. Thus, for the groundwater flow in the basement no constant heads around the catchment borders are needed which simplifies the model. All groundwater flows, recharge and discharge occur within the model domain, except for discharge into the sea.

The location of the saltwater-freshwater interface can be described by the Ghyben-Herzberg relation which indicates that the interface lies at a depth below sea level 40 times the height of the water table above sea level. Water discharges into the sea through an outlet face extending seaward from the coast (*Dingman*, 2008). Therefore a constant head boundary of 0 m was assigned at the outlet of basin in layer 1 and no flow boundaries to all other layers (Figure 4.3).

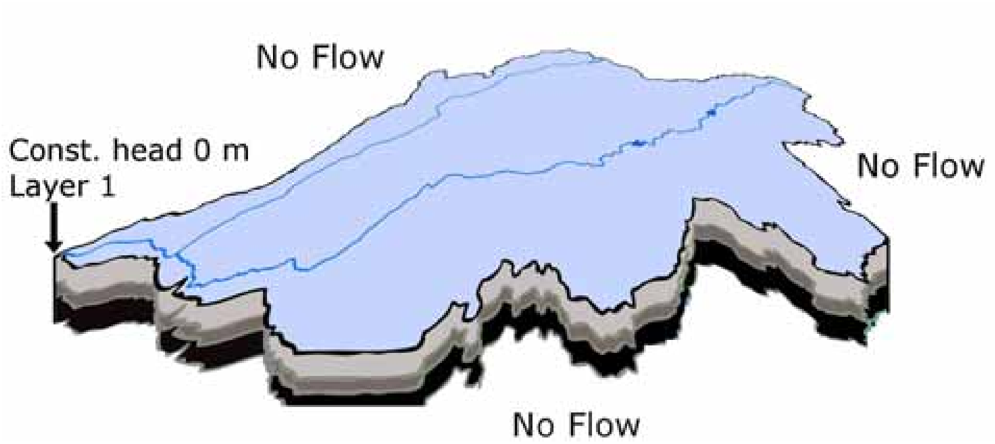

FIGURE 4.3: Boundary conditions considered in the conceptual model

The fewer cells the more stable is the model. However, the fewer cells a model runs with, the less accuracy can be achieved. In general the grid size of a groundwater flow model should not be chosen because of the size of the model but to display the dominant structures in the most realistic way (*Wolf et al.*, 2008).
Due to lack of basin wide data for hydraulic properties and the objectives of the thesis a grid size of 1 km^2 was assumed to be appropriate.
Furthermore the model setup consists of seven layers to get a smooth decrease of permeability with depth. Determinations of the layer bottom elevations were calculated by subtracting layer thickness or rather cumulated layer thicknesses from top elevation using ArcMap 9.3 (*ESRI*, 2008). Layer 1 has a thickness of 25m to enable the implementation of the shallow alluvial aquifers of the Swakop and Khan Rivers. Layer 2 has a thickness of 35 m, layer 3 of 40 m, layer 4 of 100 m, layer 5 of 200 m, layer 6 of 250 m and layer 7 a thickness of 350 m (Figure 4.1).
The model has a total area of 57594 km^2 with active cells covering 29284 km^2 in layer 1, representing the Swakop River Basin. In total the model consists of 174 rows, 331 columns and 7 layers, resulting in 403158 cells in total and 204705 active cells (198453 no flow cells).

4.3 Calibration Targets

1214 head targets were derived from the GROWAS groundwater database (*DWA*, 2004). Checking target values led to the decision only using head targets in layer 1 and 2. No basement head information were available for the area from the outlet up to 80 km westward in the database (e.g. Figure 5.3), thus one additional target was assigned near the outlet with a head of 0 m.

After applying target thinning (only one target per cell and location was permitted) a total of 967 head target data were used as the measure of observed steady-state hydraulic heads (Table 4.1).

TABLE 4.1: Distribution of selected head targets on layers

Layer	Initial head targets	Targets selected for calibration	Distribution of targets by layer[%]
1	720	606	62,67
2	402	361	37,33
3	76	0	0
4	14	0	0
5	1	0	0
6	1	0	0
7	0	0	0
Total number	1214	967	100

4.4 Recharge

Three different recharge concepts were developed and adopted which are described below.

4.4.1 Recharge concept 1

Recharge zones were assigned according to the rainfall map from *DEA* (2002) (Figure 4.4). Annual recharge was estimated as 0.5 to 1 % of annual rainfall. Direct recharge is applied to the highest active grid layer and will also occur if the layer is dry.

Recharge rates per day of concept 1 are listed in Table 4.2 for the nine zones.

TABLE 4.2: Recharge zones and rates of recharge concept 1

		0.5%	1%
Zone	P [mm/a]	Rch [m/d]	Rch [m/d]
1	25	$3.42 \cdot 10^{-7}$	$6.84 \cdot 10^{-7}$
2	75	$1.0 \cdot 10^{-6}$	$2 \cdot 10^{-6}$
3	125	$1.7 \cdot 10^{-6}$	$3.4 \cdot 10^{-6}$
4	175	$2.4 \cdot 10^{-6}$	$4.8 \cdot 10^{-6}$
5	225	$3.1 \cdot 10^{-6}$	$6.2 \cdot 10^{-6}$
6	275	$3.8 \cdot 10^{-6}$	$7.6 \cdot 10^{-6}$
7	325	$4.45 \cdot 10^{-6}$	$8.9 \cdot 10^{-6}$
8	375	$5.14 \cdot 10^{-6}$	$1.03 \cdot 10^{-5}$
9	425	$5.82 \cdot 10^{-6}$	$1.16 \cdot 10^{-5}$

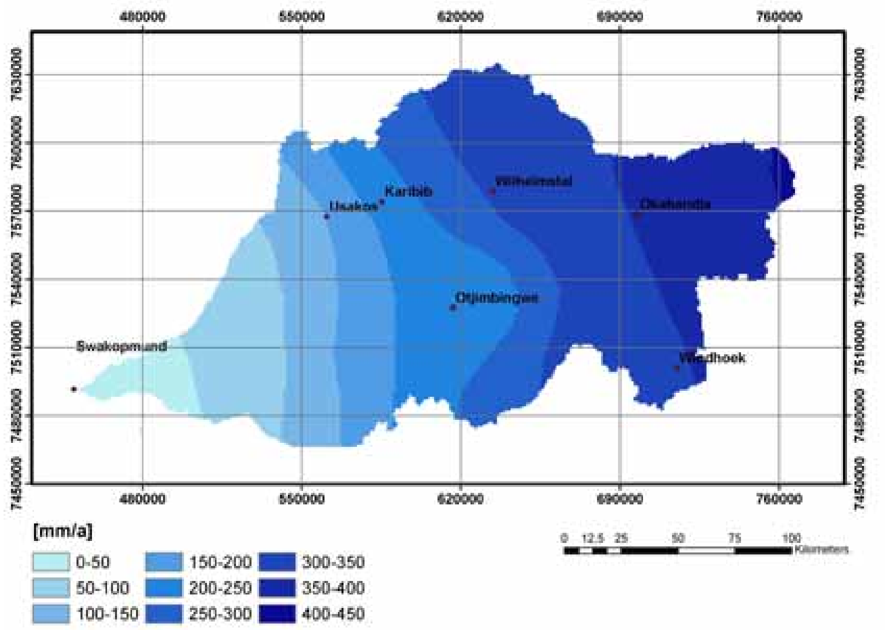

FIGURE 4.4: Recharge zones derived from annual rainfall map (*DEA*, 2002)

4.4.2 Recharge concept 2

This concept was established to account for the effect of elevation on rainfall. The rainfall zones of the rainfall map from *DEA* (2002) were blended with the digital elevation model. Mean elevation within each zone was then correlated to annual recharge (Figure 4.5). With this model recharge amounts for 23 zones were calculated (each with an extend of 100 m in altitude). Figure 4.6 shows recharge zones of this concept. All detailed rates are given in appendix A (Table A.2).

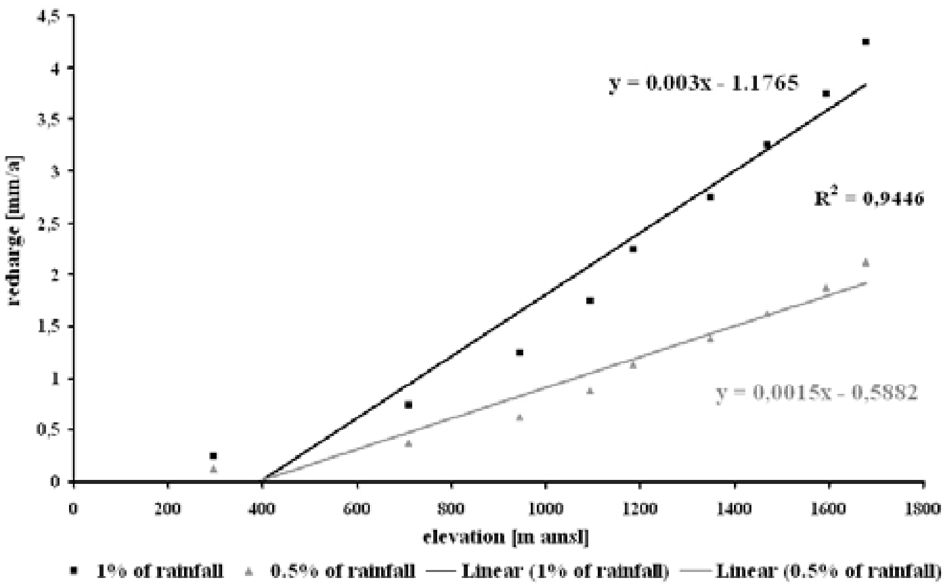

FIGURE 4.5: Correlation between recharge and elevation derived from annual rainfall map of *DEA* (2002)

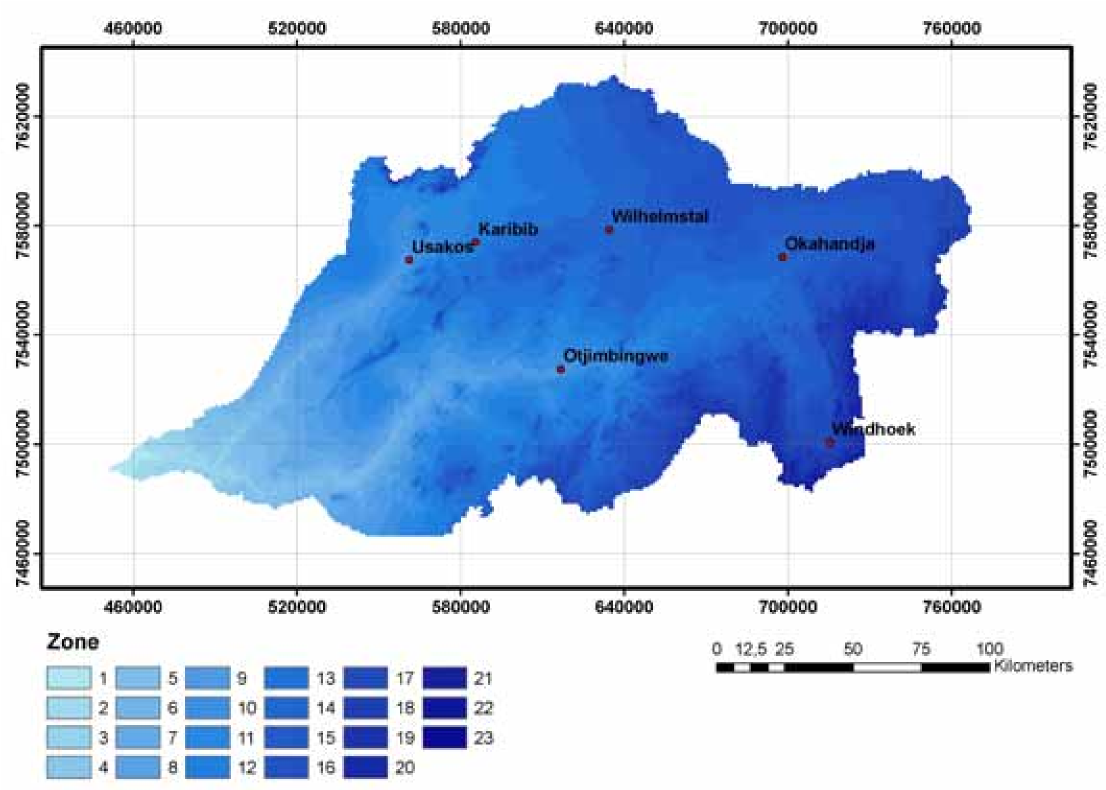

FIGURE 4.6: Recharge zones of recharge concept 2

4.4.3 Recharge concept 3

To account for local groundwater flow systems and a fractile distribution of recharge and discharge areas the topographic index (TI) of the top elevation was computed. It is considered, that discharge areas are mainly located in shallow terrain. Through this procedure areas were identified where only evaporation or only recharge takes place, i.e. in this concept recharge is defined as "net recharge", from which evaporation is already subtracted. The topographic index is defined as:

$$TI = ln(a/\tan\beta) \tag{4.1}$$

where a is the upslope contributing area per unit contour and tanβ the local slope angle (*Beven & Kirkby*, 1979). The location of different indices in the basin are given in Figure 4.7. By determining a boundary value of the index recharge and discharge/evaporation zones can be identified. All indices higher than the boundary index are reclassified to zero, all values lower then the boundary index are defined as recharge zones and reclassified to a value of 1.

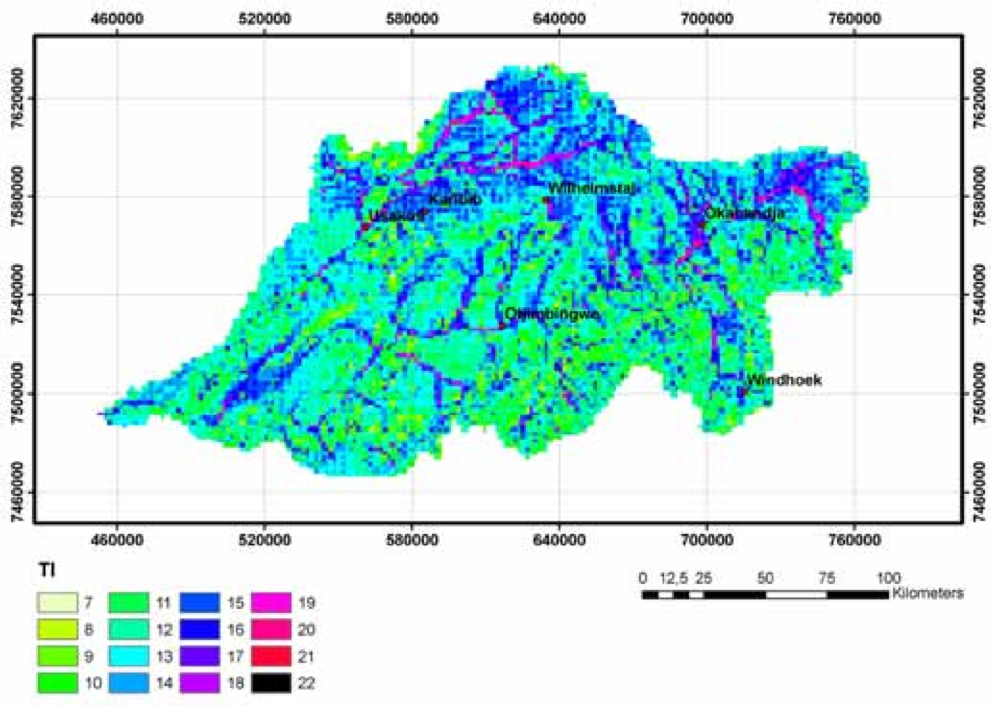

Figure 4.7: Topographic indices within the study area

The frequency distribution of the TI is shown in Figure 4.8, with a minimum index of 6.61 a maximum of 21.14 and a mean index of 12.36.

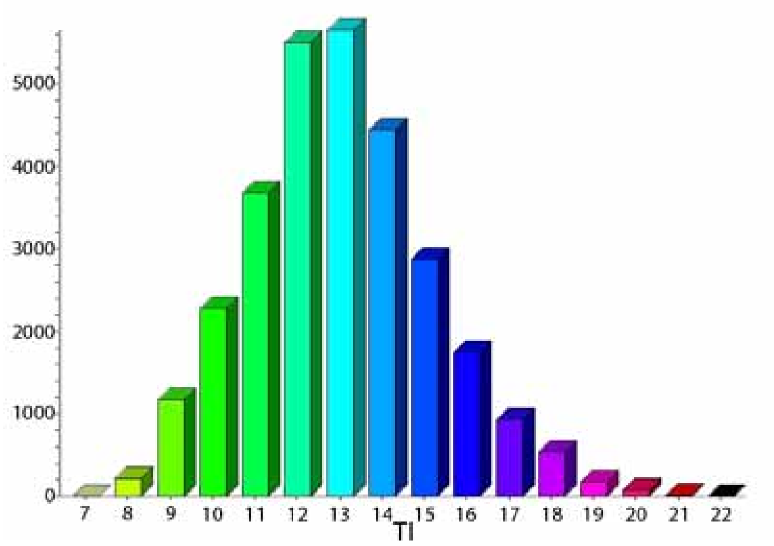

Figure 4.8: Frequency distribution of the topographic index in the study area

The binary map was multiplied with the recharge map from recharge concept 2. Figure 4.9 shows the distribution of recharge zones according to a boundary index of 12 and a recharge rate of 0.5% of annual rainfall; i.e. all indices lower than 12 were assigned as recharge zones.

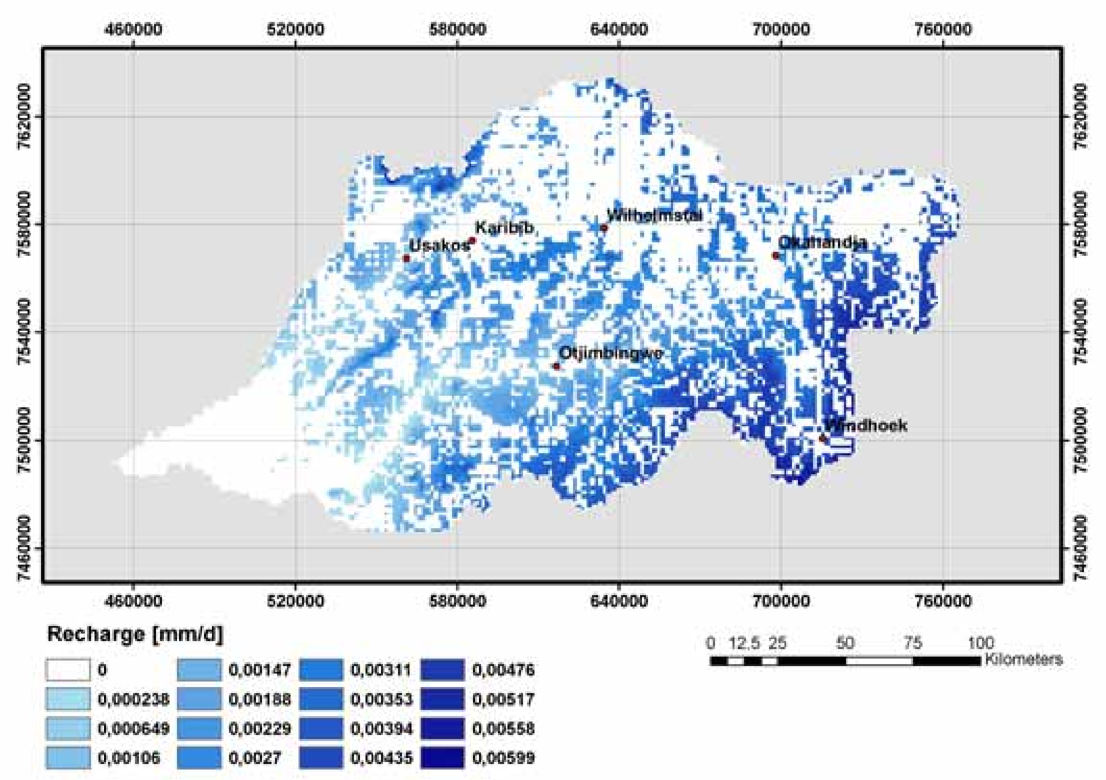

FIGURE 4.9: Recharge rates/zones of recharge concept 3

4.5 Evaporation

Three different evaporation concepts were developed and adopted which are described below. Evaporation was applied to the highest layer only and the extinction depth was set to 2 m b.g.l. in all concepts.

4.5.1 Evaporation concept 1

Evaporation zones were assigned according to the evaporation map from *DEA* (2002) (Figure 4.10). To account for higher evapotranspiration rates, due to riparian vegetation along the Khan and Swakop Rivers, additional recharge zones were generated along the river reaches.

TABLE 4.3: Rates of evaporation concept 1

Zone	ET[mm/a]	ET[m/d]
1	2700	$7{,}4\cdot10^{-3}$
2	2900	$7{,}9\cdot10^{-3}$
3	3300	$9\cdot10^{-3}$
4	3100	$8{,}5\cdot10^{-3}$

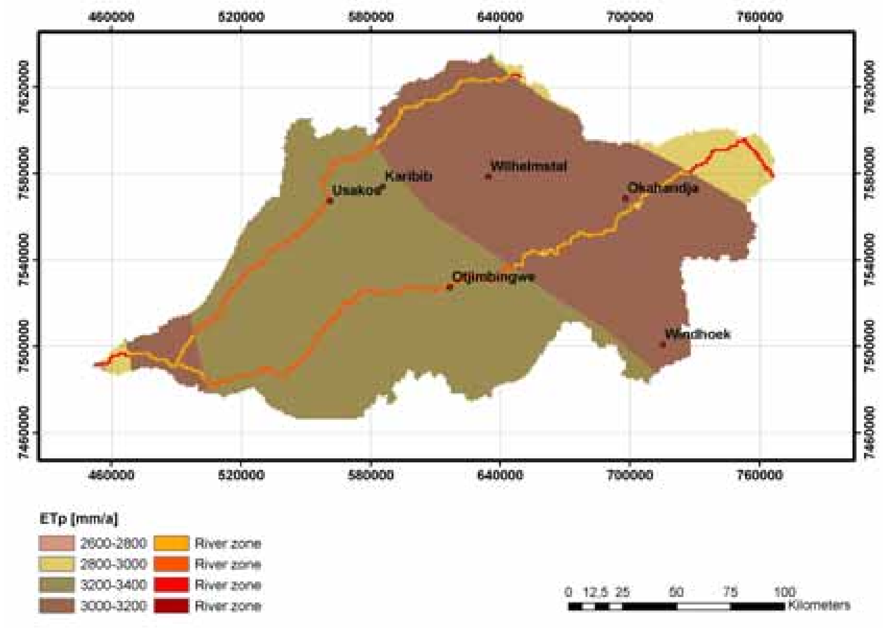

FIGURE 4.10: Potential evaporation rates per year and zones of evaporation concept 1

4.5.2 Evaporation concept 2

Evaporation zones were assigned like in recharge concept 2, based on elevation (m a.s.l.). A simple "Dalton - type" evaporation function was used to compute evaporation rates. Dalton´s law is given by Equations 4.2 and 4.3 (*Dingman*, 2008):

$$ET \propto e_s - e \tag{4.2}$$

where ET is the evaporation rate, e_s the saturation vapor pressure and e the vapor pressure. In general the proportionality depends on the height where e was measured (above the surface layer) and on the factors controlling the diffusion of water vapor in the air. The Dalton formula estimates evaporation by a mass transfer, bulk-aerodynamic method, usually using convenient parameters routinely measured at weather stations.

$$ET = f(v) \cdot (e_s - e)[mm/d] \tag{4.3}$$

f(v) = C·v is a function of wind velocity (v) in [mm/hPa·d], where C is an empirical mass transfer coefficient, dependent on the elements of weather. Due to the correlation between mean annual temperature and elevation a linear temperature gradient was computed with an increase of temperature up to 500 m a.s.l. and a decrease from 500 m to 2400 m a.s.l.. Mean annual relativ humidity (RH) was estimated as 35 - 45% according to (*DEA*, 2002) and a value of 35% was used for the calculation.

The saturation vapor pressure, which is a function only of temperature T was calculated with Equation 4.4 and the vapour pressure e with Equation 4.5 (*Maidment*, 1993). All parameters relating to elevation and temperatur are itemized in Table A.3.

$$e_s = 6,11 \cdot exp\left(\frac{17,3 \cdot T}{T + 237,3}\right) [hPa] \tag{4.4}$$

$$RH = \frac{e}{e_s} \cdot 100\% \tag{4.5}$$

Abd Ellah (2009) used amongst others the Dalton Formula to calculate evaporation rates of Wadi El-Rayan Lake, Egypt with a mean annual value for f(v) of 0.54 mm/hPa·d. As the initial f(v) a value of 0.45 mm/hPa·d was estimated, resulting in plausible annual evaporation rates, illustrated in Figure 4.11.

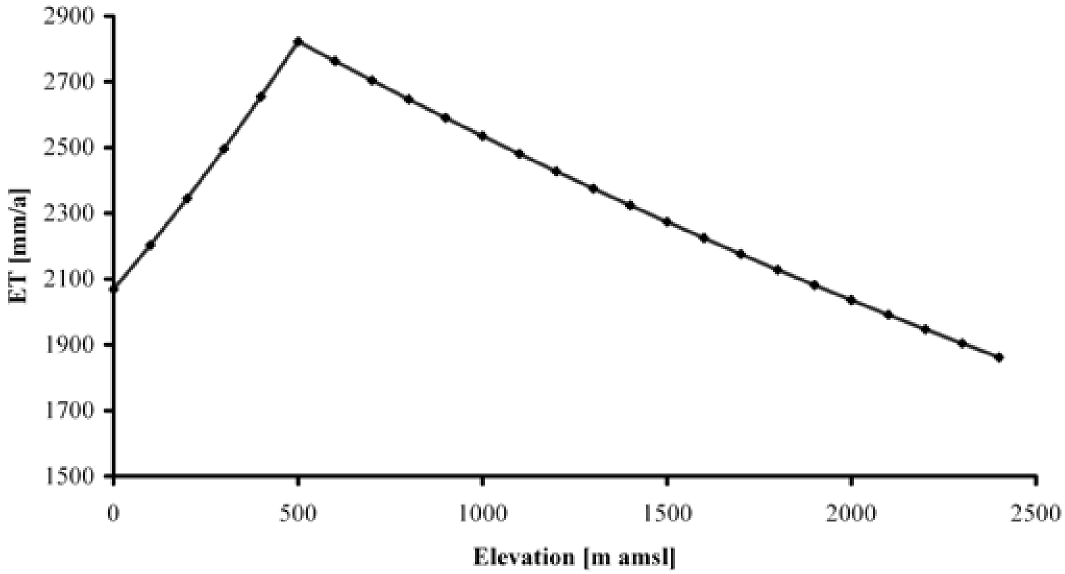

FIGURE 4.11: Correlation between elevation [m amsl] and evaporation rates [mm/a]

The distribution of evaporation zones (concept 2) within the basin are given in Figure 4.12 and the evaporation rates as well as the climatic parameters are listed in appendix A (Table A.3).

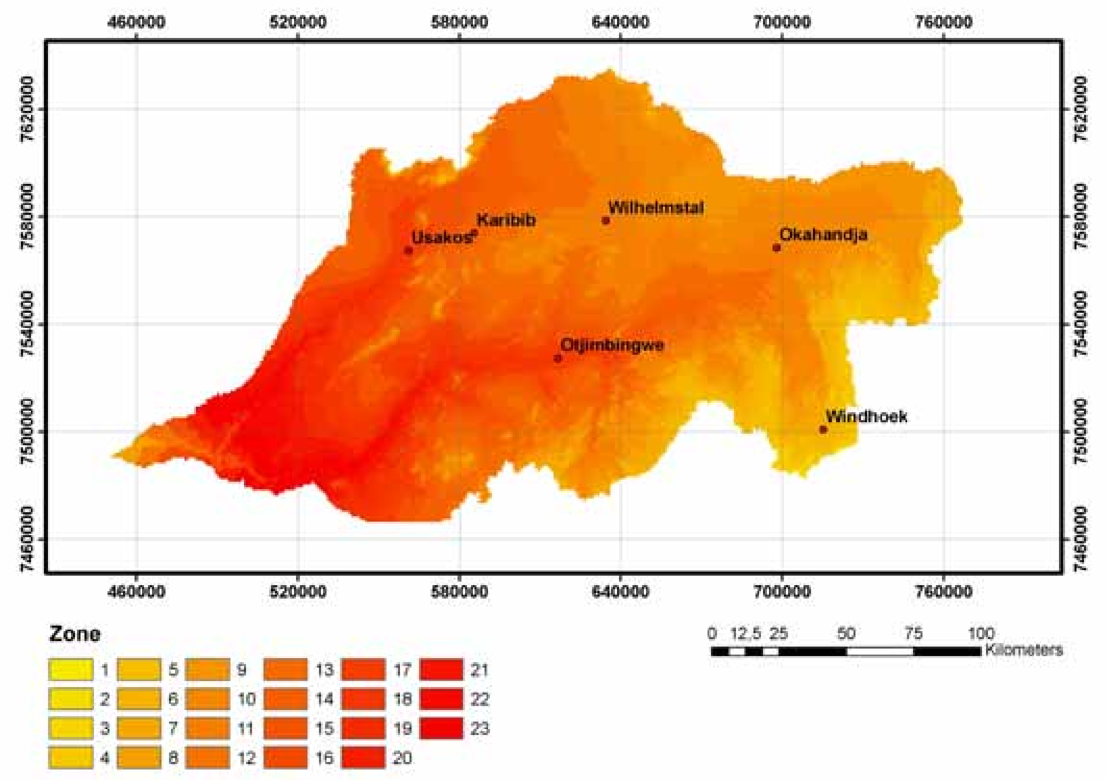

FIGURE 4.12: Evaporation zones of evaporation concept 2

4.5.3 Evaporation concept 3

For the development of the evaporation concept 3 a complementary map to the recharge map in Figure 4.9 was created. All topographic indices lower than the boundary index were defined as recharge zones and reclassified to zero evaporation and all inidces higher than the boundary index were defined as discharge or rather evaporation zones and reclassified to one. This binary map was multiplied with the evaporation map from evaporation concept 2 (Figure 4.12). Figure 4.13 shows the distribution of evaporation zones and rates with a boundary index of 12 and a Dalton coefficient f(v) of 0.45 mm/hPa·d.

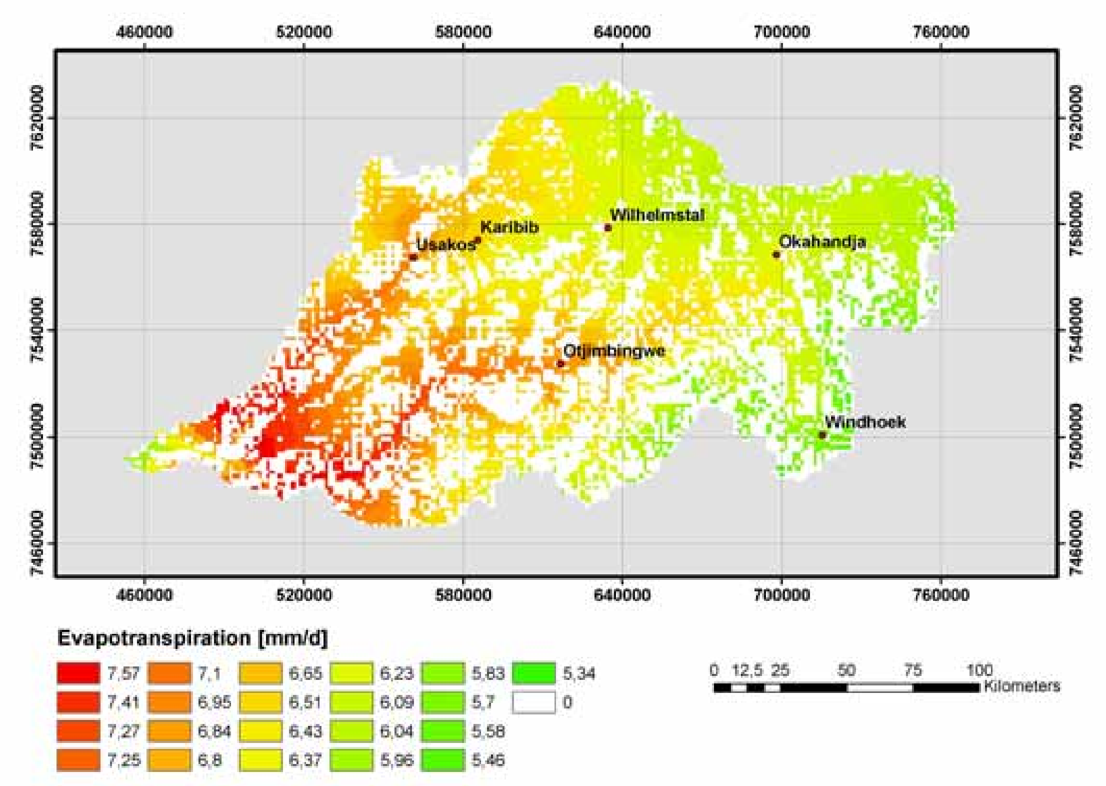

Figure 4.13: Evaporation zones and rates of evaporation concept 4

4.6 Aquifer parameters

The geology and the associated versatile rock types of the Swakop River basin are highly complex. Basin wide cross and/or longitudinal sections are not available. Hence, it is assumed that general characteristics of the basin on the regional scale can be displayed by a simplification of the geological settings. All aquifers are assumed to be unconfined with a top elevation equal to surface elevation, since soils are in general thin, poorly developed and frequently giving way to the bare rock beneath (Chapter 3.3). Aquifer parameters for numerical modeling usually are derived from pumping tests, but in fractured media it is difficult to extrapolate them to the scale of the grid size and of the regional model (*Kresic*, 2006). Therefore hydraulic parameters found in literature were used. Hydraulic parameters released in publications for rock types occurring in the study area are listed in Table 4.5. Vertical hydraulic conductivity was always estimated as one order of magnitude less than the horizontal and is therefore not explicit listed. Furthermore leakance (vertical conductance) was computed by dividing vertical conductivity by inter-layer distance between two adjacent nodal layers (*HydrogeologicInc.*, 2007).

4.6.1 Aquifer concept 1

Each discrete layer was set up with uniform parameters and a depth dependent hydraulic conductivity according to equation 2.6 of *Saar & Magna* (2004). Figure 4.14 gives examples of decreasing hydraulic conductivity with depth. An initial kf-value of $8.64 \cdot 10^{-3}$ m/d according to *Mainardy* (1999) was used.

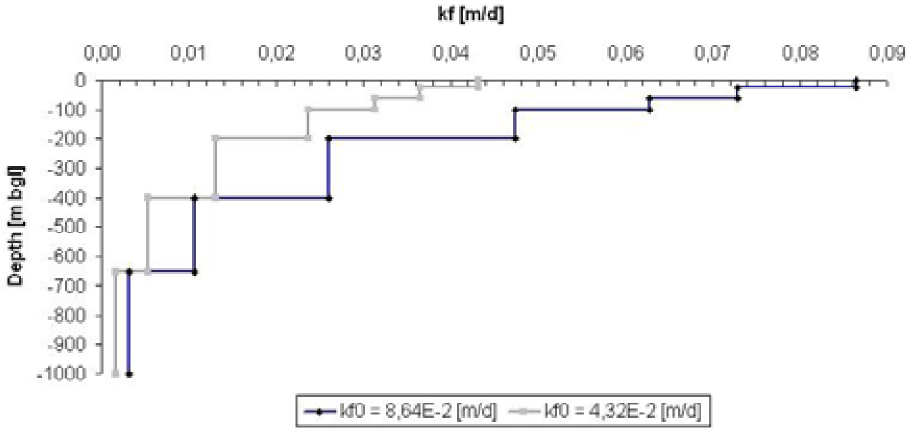

FIGURE 4.14: Decrease of kf-values according to layer depth

4.6.2 Aquifer concept 2

Aquifer zones were assigned according to the classification of groundwater potentials in the hydrogeological map (*DWA & GSN*, 2001) (Chapter 3.5.3). Five hydrogeological units (Figure 4.15) were implemented:

1. Rock bodies with low to moderate groundwater potential (23065 km^2)
2. Fractured aquifers with moderate groundwater potential (1704 km^2)
3. Rock bodies with limited to very low groundwater potential (3159 km^2)
4. Fractured aquifers with high groundwater potential (523 km^2)
5. Porous aquifers with high groundwater potential (833 km^2)

The zones encompass all seven layers with a decrease of hydraulic conductivity according to Equation 2.6 of *Saar & Magna* (2004), except for zone 5, representing the alluvial aquifers, which are assigned to layer 1 only. Effective channel widths along the river reaches varies between around 8 m to 300 m (*CSIR*, 1997); an average of about 100 m is assumed here. The hydraulic parameters for the alluvial aquifers were aggregated to the 1 km^2 grid using the arithmetic mean, resulting in approximately one order of magnitude less than observed in the field by *DWA* (1970).

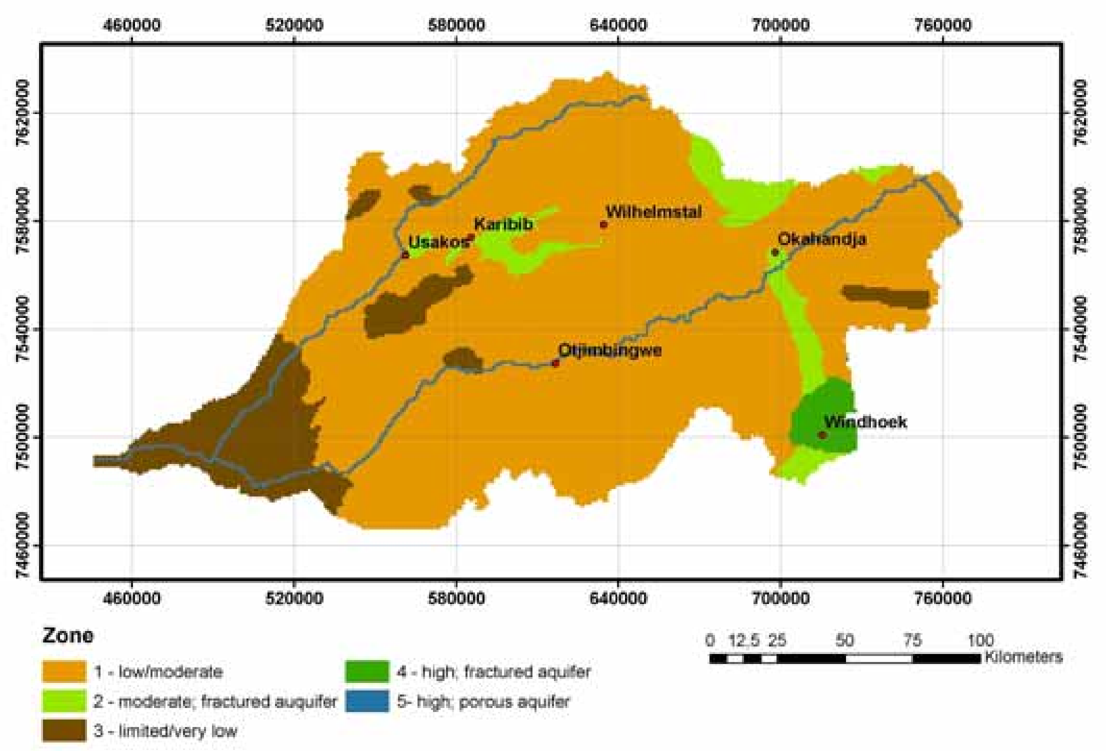

FIGURE 4.15: Zones of aquifer concept 2

Parameter ranges for each aquifer category were determined for calibration purpose. In Table 4.4 the various zones, parameter ranges and initial hydraulic parameters are listed, Figure 4.15 illustrates the distribution of aquifer zones in the basin.

TABLE 4.4: Initial hydraulic parameters and kf_0-ranges for aquifer zones

Zone	Category	kf_0-range [m/d]		Initial k_0f [m/d]	Initial n_{eff}
1	low/moderate	$8.64{\cdot}10^{-5}$	- $8.64{\cdot}10^{-2}$	$8.64{\cdot}10^{-4}$	0.08
2	moderate (fractured)	$8.64{\cdot}10^{-4}$	- $8.64{\cdot}10^{-1}$	$8.64{\cdot}10^{-3}$	0.1
3	limited/very low	$8.64{\cdot}10^{-6}$	- $8.64{\cdot}10^{-3}$	$8.64{\cdot}10^{-5}$	0.05
4	high (fractured)	$8.64{\cdot}10^{-4}$	- 8.64	$8.64{\cdot}10^{-2}$	0.12
5	high (porous)	$8.64{\cdot}10^{-1}$	- 864	30	0.2

TABLE 4.5: Hydraulic parameters for crystalline and metamorphic rocks

Author	Location	Rock type	kf [m/s]	K [m^2]	n_{eff}
Lippert (1986)	Pustertal/South Tyrol	granite	$3.00 \cdot 10^{-5}$		0.0565
		quartz-phyllite	$6.00 \cdot 10^{-6}$		0.0166
		orthogneiss	$3.00 \cdot 10^{-6}$		0.0227
		paragneiss	$4.00 \cdot 10^{-6}$		0.0333
Ophori (2004)	WRA Manitoba/Canada	plutonic rock mass		$1.00 \cdot 10^{-15}$	0.005
		fractured zones		$1.00 \cdot 10^{-13}$	0.05
Saar & Magna (2004)	Oregon Cascades	continental crust		$5.00 \cdot 10^{-13}$	
Ingebritsen & Manning (1999)				$1.00 \cdot 10^{-13}$	
Watkins (2007)	Cornwall. UK	granite			
		30-100m	$1 \cdot 10^{-6}/1 \cdot 10^{-5}$		
		few hundreds m	$1 \cdot 10^{-7}/1 \cdot 10^{-9}$		
Mainardy (1999)	Namibia				
	N of Okahandja	pegmatite	$1 \cdot 10^{-7}$		
	N of Okahandja	granodiorite	$5 \cdot 10^{-8}$		
	Windhoek	mica schist	$5 \cdot 10^{-8}$		
	Swakoprevier	amphibolite	$1 \cdot 10^{-7}$		
Mattheß & Ubell (1983)		weathered schist			up to 0.5
		fresh igneous/metamorphic rocks			0.01-0.03
		lavas			up to 0.05
Klock (2001)	Namibia	Damara and pre-Damara	$1 \cdot 10^{-7}$		0.08
		karstified Damara	$5 \cdot 10^{-6}$		0.12
Balke (2000)	global	fractured dolomite. sandstones.	$1 \cdot 10^{-3}$ -		
		crystalline rocks	$1 \cdot 10^{-9}$		
		consolidated crystalline rocks	$1 \cdot 10^{-9}$-$1 \cdot 10^{-13}$		
		fractured phylitte. metamorphic r.	$1 \cdot 10^{-6}$-$1 \cdot 10^{-10}$		
DWA (1970)	Swakop basin	Swakop alluvial aquifer	$2.53 \cdot 10^{-3}$		0.18
	near Rössing	Khan alluvial aquifer	$3.31 \cdot 10^{-3}$		0.23

Chapter 5

Results

Three models were developed by combining different recharge-, evaporation-, and aquifer concepts, while increasing complexity according to basin characteristics. Each of them was performed with a recharge amount of 0.5% and 1% of annual rainfall, denoted as minmum and maximum approach, respectively. Consecutive variation of hydraulic conductivity followed, until the simulated groundwater levels fitted reasonable with the observed ones. Best results were achieved with the maximum approach of Model 2 (Chapter 5.2), which was used for determination of the groundwater flow system (Chapter 5.4) as well as for flow path and mass balance investigations at six selected river compartments (Chapter 5.5).

5.1 Model 1

Model 1 combines the recharge and evaporation concept 1 which is based on the rainfall map and the map of potential evaporation of the Atlas of Namibia (*DEA*, 2002) (Chapters 4.4.1 and 4.5.1) and the uniform aquifer concept 1 (Chapter 4.6.1).

5.1.1 Aquifer parameter

Best model performances were achieved with a near surface hydraulic conductivity of $kf_0 = 9.55 \cdot 10^{-9}$[m/s] for the minimum approach and a near surface hydraulic conductivity of $kf_0 = 9.8 \cdot 10^{-8}$[m/s] for the maximum approach. Aquifer parameters for the two approaches are listed in Table 5.1.

Table 5.1: Hydraulic parameters of Model 1

Layer	min. approach $kf_{x.y}$ [m/d]	kf_z[m/d]	n_{eff}	max. approach $kf_{x.y}$ [m/d]	kf_z[m/d]	n_{eff}
1	$8.25\cdot10^{-4}$	$8.25\cdot10^{-5}$	0.05	$8.47\cdot10^{-3}$	$8.47\cdot10^{-4}$	0.05
2	$6.96\cdot10^{-4}$	$6.96\cdot10^{-5}$	0.05	$7.14\cdot10^{-3}$	$7.14\cdot10^{-4}$	0.05
3	$5.99\cdot10^{-4}$	$5.99\cdot10^{-5}$	0.05	$6.15\cdot10^{-3}$	$6.15\cdot10^{-4}$	0.05
4	$4.53\cdot10^{-4}$	$4.53\cdot10^{-5}$	0.05	$4.65\cdot10^{-3}$	$4.65\cdot10^{-4}$	0.05
5	$2.49\cdot10^{-4}$	$2.49\cdot10^{-5}$	0.05	$2.55\cdot10^{-3}$	$2.55\cdot10^{-4}$	0.05
6	$1.01\cdot10^{-4}$	$1.01\cdot10^{-5}$	0.05	$1.04\cdot10^{-3}$	$1.04\cdot10^{-4}$	0.05
7	$3\cdot10^{-5}$	$3\cdot10^{-6}$	0.05	$3.1\cdot10^{-4}$	$3.1\cdot10^{-5}$	0.05

5.1.2 Model performance

For the minimum and the maximum approach observed groundwater levels were plotted against simulated ones. Calibration statistics (Table 5.2) were computed as well as the location of the residuals determined. The results are shown in Figures 5.1 and 5.2 and are described below separately for the minimum and maximum approach.

Table 5.2: Calibration statistics of model 1

	min. approach	max. approach
Residual Mean	-16.06 m	-4.20 m
Res. Std. Dev.	22.83 m	34.75 m
Min. Residual	-78.40 m	-68.21 m
Max. Residual	168.10 m	233.75 m
Range in Target Values	1885 m	1885 m
MAE	22.25 m	25.05 m
RMS	27.9 m	34.99 m
R^2	0.993	0.985

Minimum approach:
The root mean square error (RMS) of the minimum approach is 27.9 m, the mean absolute error (MAE) 22.25 m. The residual standard deviation is 22.83 m, the residual mean -16.06 m and the coefficient of determination (R^2) is 0.993.
The scatter plots in Figure 5.1 and Figure 5.2 show good fits for observed and simulated groundwater levels in the western part of the catchment up to approximately 800 m a.s.l.. The most negative residual appears with a value of -78.4 m and is located in layer 2 (red arrow in Figure 5.3 a). In general, the majority of residuals are negative, i.e. these simulated heads are higher than the observed ones (especially in layer 2). With increasing elevation also the scatter increases and the largest positive residuals occur with a maximum residual of 168.1 m (black arrow in Figure 5.3 a). The basin wide distribution of positive (green) and negative (orange) residuals in Figure 5.3 a depicts that the majority of positive residuals is located in the SSW within the Khomas Highland.

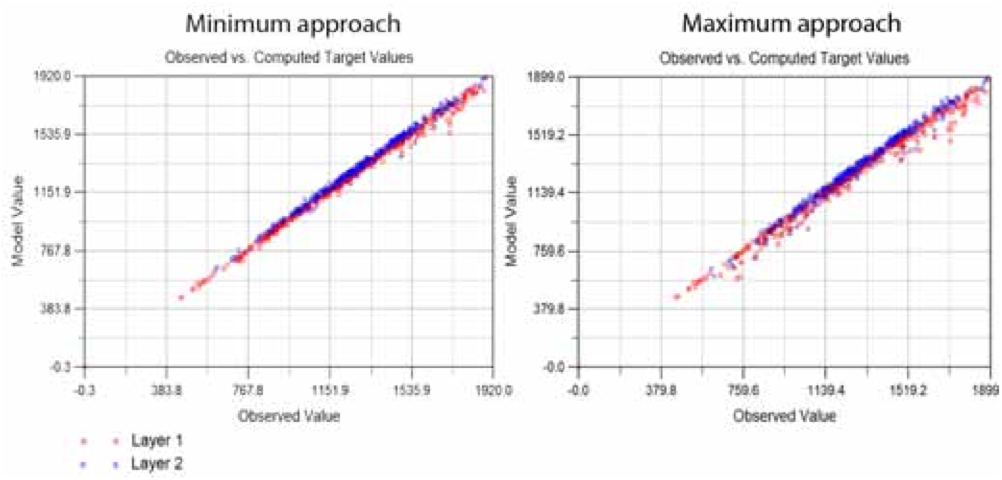

FIGURE 5.1: Observed vs. simulated groundwater heads - Model 1

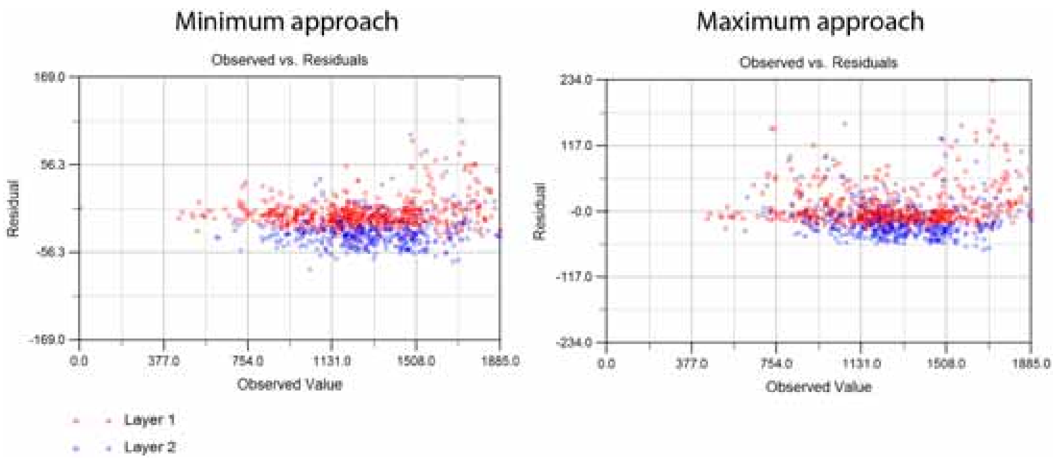

FIGURE 5.2: Observed heads vs. residuals - Model 1

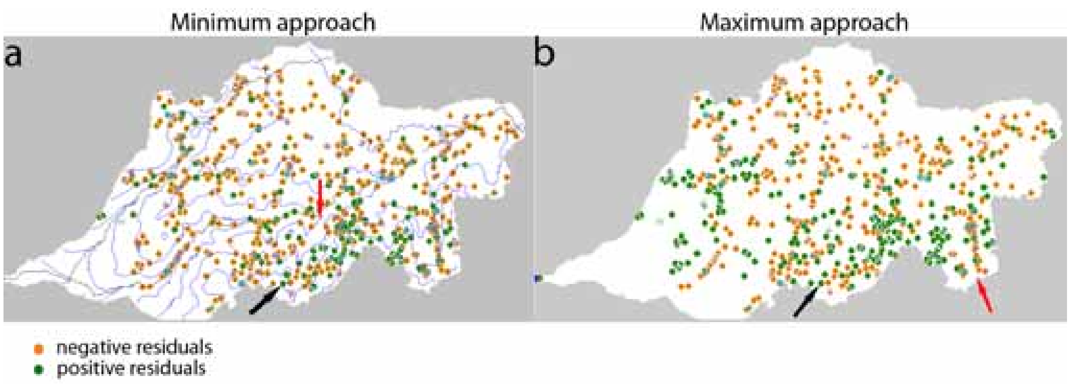

FIGURE 5.3: Residual circles - Model 1

Maximum approach:
Best simulation with the maximum approach resulted in a RMS value of 34.99 m and a MAE value of 25.05 m. The residual standard deviation is 34.75 m and the residual mean -4.2 m (R^2=0.984). In contrast to the minimum approach of model 1 the scatter plot of observed versus simulated groundwater heads (Figure 5.1 b) illustrates greater residuals in the western part of the catchment, while the scattering looks nearly similar in higher elevations. The most negative residual appears in layer 2 with a value of -68.21 m near Windhoek within sandstones (red arrow), the most positive (black arrow) with a value of 233.75 m complies with the location of the most positive one of the minimum approach.

5.1.3 Mass balance

In Tables 5.3 and 5.4 the model summaries of mass balances for the minimum and maximum approach are listed, specifying in- and outputs for each layer. Figure 5.4 illustrates the total fluxes of each approach.

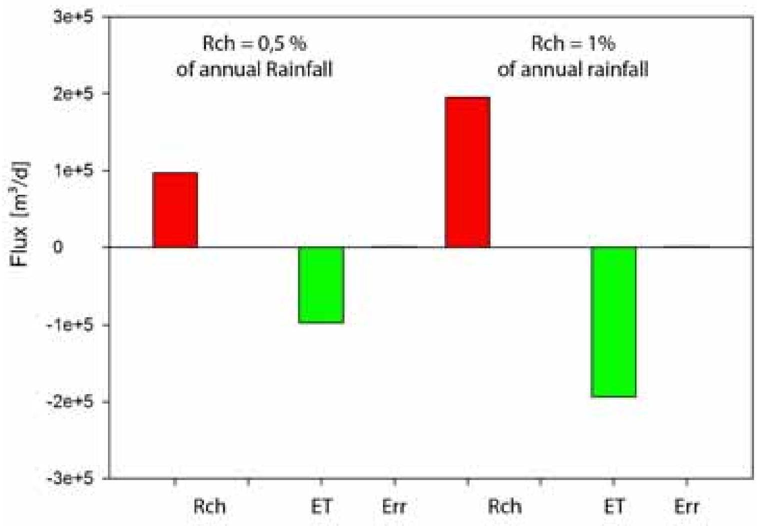

FIGURE 5.4: Mass balance model summaries of model 1

Minimum approach:
The recharge (Rch) amount is $9.72{\cdot}10^4$ m^3/d which equals to 35 $\cdot 10^6$ m^3/a. An evaporation rate (ET) of $9.70{\cdot}10^4$ m^3/d compensates the recharge amount nearly completely. A small amount of surface runoff ($8.25 \cdot 10^{-1}$ m^3/d = recharge out) and a inflow from the sea of $2.25{\cdot}10^{-3}$ m^3/d(= const. head) occur, resulting in a total error between inputs and outputs of 0.18% (Table 5.3.

TABLE 5.3: Mass balance summary Model 1 - minimum approach (fluxes in m^3/d)

Layer	1	2	3	4	5	6	7
Recharge in	$9.72 \cdot 10^4$						
Recharge out	$8.25 \cdot 10^{-1}$						
ET out	$9.70 \cdot 10^4$						
Const. Head	$2.25 \cdot 10^{-3}$						
Qz Top in		$4.28 \cdot 10^4$	$3.83 \cdot 10^4$	$3.30 \cdot 10^4$	$2.19 \cdot 10^4$	$9.24 \cdot 10^3$	$2.72 \cdot 10^3$
Qz Top out		$4.28 \cdot 10^4$	$3.83 \cdot 10^4$	$3.30 \cdot 10^4$	$2.19 \cdot 10^4$	$9.24 \cdot 10^3$	$2.72 \cdot 10^3$
Qz Bottom in	$4.28 \cdot 10^4$	$3.83 \cdot 10^4$	$3.30 \cdot 10^4$	$2.19 \cdot 10^4$	$9.24 \cdot 10^3$	$2.72 \cdot 10^3$	
Qz Bottom out	$4.28 \cdot 10^4$	$3.83 \cdot 10^4$	$3.30 \cdot 10^4$	$2.19 \cdot 10^4$	$9.24 \cdot 10^3$	$2.72 \cdot 10^3$	
IN	$1.40 \cdot 10^5$	$8.12 \cdot 10^4$	$7.13 \cdot 10^4$	$5.49 \cdot 10^4$	$3.12 \cdot 10^4$	$1.20 \cdot 10^4$	$2.72 \cdot 10^3$
OUT	$1.40 \cdot 10^5$	$8.12 \cdot 10^4$	$7.13 \cdot 10^4$	$5.49 \cdot 10^4$	$3.12 \cdot 10^4$	$1.20 \cdot 10^4$	$2.72 \cdot 10^3$
Total IN	97213.53						
Total OUT	97035.49						
Total Error	0.18%						

Maximum approach:

Compared to the minimum approach the total error between all inputs and outputs of this approach (0.14%) is slightly smaller. Input by recharge is $1.945 \cdot 10^5$ m^3/d which equals to $71.18 \cdot 10^6$ m^3/a of which 33.8 m^3/d were conducted by surface runoff. Recharge is counterbalanced by an evaporation amount of $1.941 \cdot 10^5$ m^3/d and a marginal outflow to the sea of 0.39 m^3/d.

TABLE 5.4: Mass balance summary Model 1 - maximum approach (fluxes in m^3/d)

Layer	1	2	3	4	5	6	7
Recharge in	$1.95 \cdot 10^5$						
Recharge out	$3.38 \cdot 10^1$						
ET out	$1.94 \cdot 10^5$						
Const. Head	$-3.94 \cdot 10^{-1}$						
Qz Top in		$1.16 \cdot 10^5$	$9.70 \cdot 10^4$	$7.77 \cdot 10^4$	$4.41 \cdot 10^4$	$1.54 \cdot 10^4$	$3.88 \cdot 10^3$
Qz Top out		$1.16 \cdot 10^5$	$9.70 \cdot 10^4$	$7.77 \cdot 10^4$	$4.41 \cdot 10^4$	$1.54 \cdot 10^4$	$3.88 \cdot 10^3$
Qz Bottom in	$1.16 \cdot 10^5$	$9.70 \cdot 10^4$	$7.77 \cdot 10^4$	$4.41 \cdot 10^4$	$1.54 \cdot 10^4$	$3.88 \cdot 10^3$	
Qz Bottom out	$1.16 \cdot 10^5$	$9.70 \cdot 10^4$	$7.77 \cdot 10^4$	$4.41 \cdot 10^4$	$1.54 \cdot 10^4$	$3.88 \cdot 10^3$	
IN	$3.11 \cdot 10^5$	$2.13 \cdot 10^5$	$1.75 \cdot 10^5$	$1.22 \cdot 10^5$	$5.95 \cdot 10^4$	$1.92 \cdot 10^4$	$3.88 \cdot 10^3$
OUT	$3.11 \cdot 10^5$	$2.13 \cdot 10^5$	$1.75 \cdot 10^5$	$1.22 \cdot 10^5$	$5.95 \cdot 10^4$	$1.92 \cdot 10^4$	$3.88 \cdot 10^3$
Total IN	194500.49						
Total OUT	194224.69						
Total Error	0.14 [%]						

5.2 Model 2

Model 2 combines recharge concept 2, evaporation concept 2 and the aquifer concept 2 (Chapters 4.4.2 and 4.5.2) with the hydrogeological units based on the hydrogeological map (*DWA & GSN*, 2001) (Chapter 3.5.3).

5.2.1 Aquifer parameters

Minimum approach:

Best model performances for the minimum approach were achieved with near surface hydraulic conductivities of $7.78 \cdot 10^{-4}$ m/d for rock bodies with low to limited groundwater potential, $1.3 \cdot 10^{-3}$ m/d for rock bodies with low to moderate, $8.64 \cdot 10^{-3}$ m/d for fractured aquifers with moderate, $1.73 \cdot 10^{-2}$ m/d for fractured aquifers with high and at last 28 m/d for the porous aquifers with high groundwater potential. In Table 5.5 the hydraulic parameters and their exponential decrease from layer 1 to 7 are listed.

TABLE 5.5: Hydraulic parameters of the minimum approach (kf-values in m/d)

Layer	low/limited	low/moderate	moderate/fractured	high/fractured	high/porous
1	$7.78 \cdot 10^{-4}$	$1.3 \cdot 10^{-3}$	$8.64 \cdot 10^{-3}$	$1.73 \cdot 10^{-2}$	28
2	$6.56 \cdot 10^{-4}$	$1.09 \cdot 10^{-3}$	$7.29 \cdot 10^{-3}$	$1.46 \cdot 10^{-2}$	
3	$5.65 \cdot 10^{-4}$	$9.41 \cdot 10^{-4}$	$6.27 \cdot 10^{-3}$	$1.25 \cdot 10^{-2}$	
4	$4.27 \cdot 10^{-4}$	$7.11 \cdot 10^{-4}$	$4.74 \cdot 10^{-3}$	$9.48 \cdot 10^{-3}$	
5	$2.34 \cdot 10^{-4}$	$3.90 \cdot 10^{-4}$	$2.60 \cdot 10^{-3}$	$5.21 \cdot 10^{-3}$	
6	$9.5 \cdot 10^{-5}$	$1.59 \cdot 10^{-4}$	$1.06 \cdot 10^{-3}$	$2.12 \cdot 10^{-3}$	
7	$2.9 \cdot 10^{-5}$	$4.8 \cdot 10^{-5}$	$3.19 \cdot 10^{-4}$	$6.37 \cdot 10^{-4}$	
n_{eff}	0.05	0.08	0.1	0.12	0.18

Maximum approach:

For the maximum approach only the hydraulic conductivity of the largest hydrogelogical unit, namely rock bodies with low to moderate potential changed to $4.32 \cdot 10^{-3}$ m/d. In Table 5.6 the hydraulic conductivities and their exponential decrease are listed.

Table 5.6: Hydraulic parameters for the maximum approach (kf-values in m/d)

Layer	low/limited	low/moderate	moderate/fractured	high/fractured	high/porous
1	$7.78{\cdot}10^{-4}$	$4.32{\cdot}10^{-3}$	$8.64{\cdot}10^{-3}$	$1.73{\cdot}10^{-2}$	28
2	$6.56{\cdot}10^{-4}$	$3.64{\cdot}10^{-3}$	$7.29{\cdot}10^{-3}$	$1.46{\cdot}10^{-2}$	
3	$5.65{\cdot}10^{-4}$	$3.14{\cdot}10^{-3}$	$6.27{\cdot}10^{-3}$	$1.25{\cdot}10^{-2}$	
4	$4.27{\cdot}10^{-4}$	$2.37{\cdot}10^{-3}$	$4.74{\cdot}10^{-3}$	$9.48{\cdot}10^{-3}$	
5	$2.34{\cdot}10^{-4}$	$1.30{\cdot}10^{-3}$	$2.60{\cdot}10^{-3}$	$5.21{\cdot}10^{-3}$	
6	$9.5{\cdot}10^{-5}$	$5.3{\cdot}10^{-4}$	$1.06{\cdot}10^{-3}$	$2.12{\cdot}10^{-3}$	
7	$2.9{\cdot}10^{-5}$	$1.6{\cdot}10^{-4}$	$3.19{\cdot}10^{-4}$	$6.37{\cdot}10^{-4}$	
n_{eff}	0.05	0.08	0.1	0.12	0.18

5.2.2 Model performance

In Figure 5.5 observed versus simulated groundwater levels for the minimum and the maximum approach are plotted. Figure 5.6 shows residuals corresponding to observed water levels and Figure 5.7 the location of positive and negative residuals within layer 1. Calibration statistics are listed in Table 5.7.

Table 5.7: Calibration statistics of model 2

	min. approach	max. approach
Residual Mean	-14.44 m	-13.93 m
Res. Std. Dev.	27.87 m	24.73 m
Min. Residual	-81.17 m	-72.54 m
Max. Residual	171.87 m	168.29 m
Range in Target Values	1885 m	1885 m
MAE	23.52 m	22.12 m
RMS	31.37 m	28.37 m
R^2	0.990	0.992

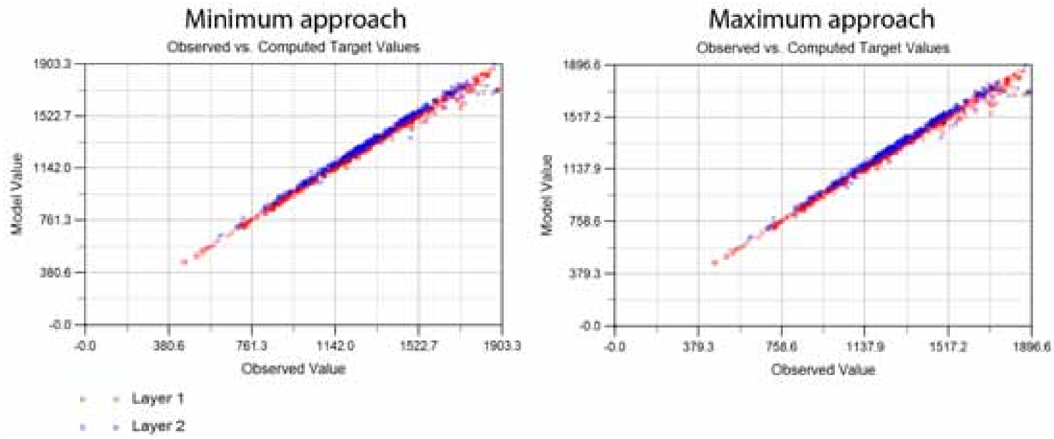

FIGURE 5.5: Observed vs. simulated groundwater heads - Model 2

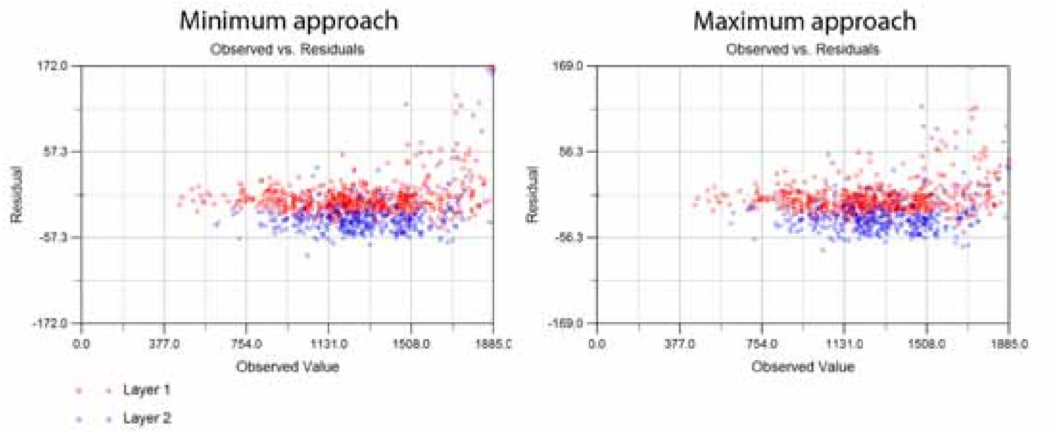

FIGURE 5.6: Observed groundwater heads vs. residuals - Model 2

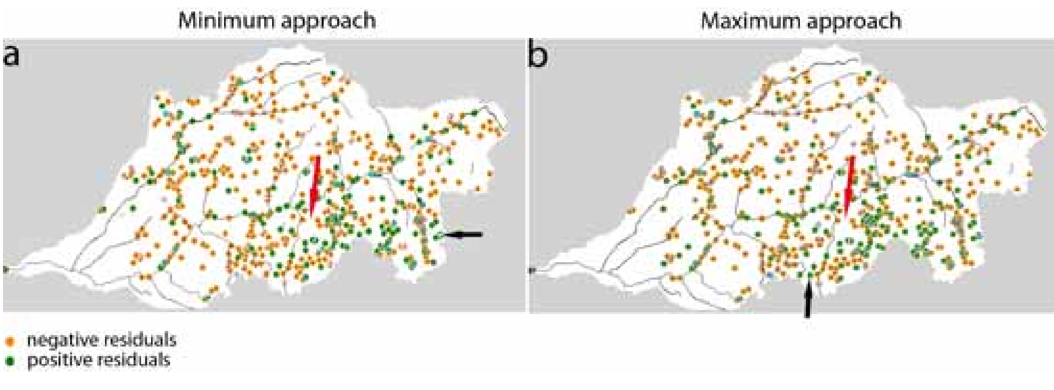

FIGURE 5.7: Residual circles - Model 2

Minimum approach:

Best model performance, achieved with hydraulic parameters listed in Table 5.5, resulted in a RMS value of 31.37 m and a MAE value of 23.52 m. The scatter plot in Figure 5.5 a is illustrating a better fit of observed and simulated groundwater levels compared to the minimum approach of model 1. The majority of positive residuals (observed groundwater levels higher than the simulated ones) are situated within and in the south of the Swakop River. The most negative residual with a value of -81.17 m is located in layer 2 at the same position like in the minimum approach of Model 1 (red arrow). The most positive residual is situated in the Windhoek aquifer northeast of Windhoek in layer 1 and has a value of 171.87 m (black arrow in Figure 5.7 a). The residual mean of this approach is -14.44 m and the residual standard deviation 27.87 m.

Maximum approach:

Since the maximum approach of model 2 resulted in the best model performance compared to all concepts, it was used for further investigations and in the following it will be described in detail.

The RMS and MAE values for the best model performance are 28.37 m and 22.12 m, respectively (R^2=0.992). Like in the other model approaches, the majority of simulated groundwater levels are higher than the observed ones, especially in layer 2. The scatter plot in Figure 5.5 illustrates better fits between observed an simulated heads in lower elevations than in higher elevations. As shown in Figure 5.7 b, again, the most negative residual is located approximately 25 km east of Otjimbingwe (red arrow). The largest residual with a value of 168.29 m is located in the south within the schists of the Kuiseb Formation (black arrow, Figure 5.7b), like in the maximum approach of model 1. The residual mean is -13.93 m and the residual standard deviation 24.73 m (Table 5.7).

In Figure 5.8 the longitudinal section R4 (see position in Figure 5.17) illustrates the groundwater level (blue) and the occurrence of dry cells (red). Particularly these dry cells appear in mountains and at the outlet of the basin where no calibration targets are located.

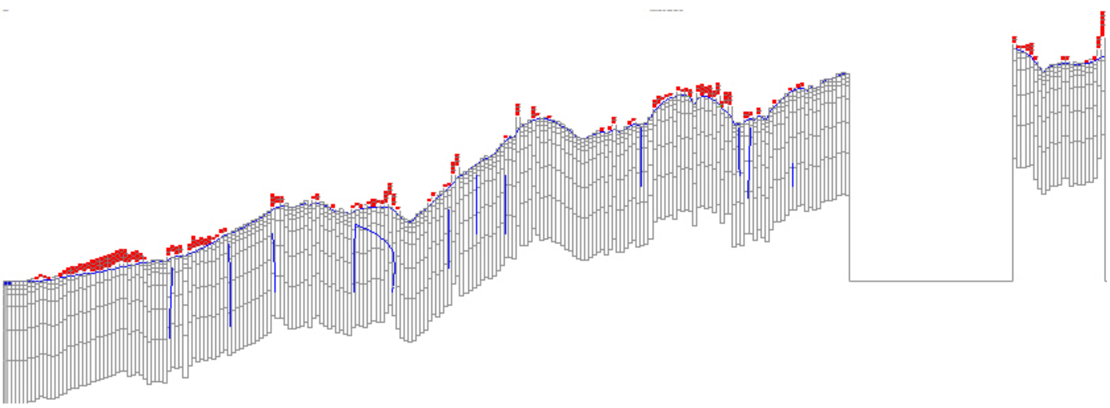

FIGURE 5.8: Dry cells and the groundwater contour line in the longitudinal section R4

In Figure 5.9 geological maps (1:1 mio (*DEA*, 2002)) are shown, illustrating main rock types, dykes and faults (derived from *GSN* (n.a.)) (Chapter 3.5.2). Residual classes with ranges of 20 m are plotted within. 40 residuals, (4.1 % of all included targets) with values from -72.54 m to -50 m given in Figure 5.9 a, are mainly distributed marginally and along fault structures. Residuals ranging from -50 m to -30 m are 190 in number (19.7 %) and shown in Figure 5.9 b. Many of them are also located nearby faults. Figure 5.9c represents 366 values (37.9 %) between -30 m and -10 m which are almost equally disposed over the whole area and often in areas where faults are nested (e.g. Windhoek aquifer). Negative residuals along the alluvial aquifers occur predominantly in the north of Usakos and Karibib. In Figure 5.9 d, 273 values (28.3 %) between -10 m and 10 m are illustrated, frequently situated along the river reaches. Further 35 positive residuals (3.6 %) are given in Figure 5.9 e ranging from 10 m to 20 m. These are also located at river reaches and mainly in the south-southeast. The positive residuals, 52 in number (5.4 %) and plotted in Figures 5.9 f,g and h with values from 20 m to 168.29 m in total are primaly located in the schists of the Khomas Highland. The most positive residual, already adressed above is lying near the interface between the schists and granites in the south-west of Otjimbingwe.

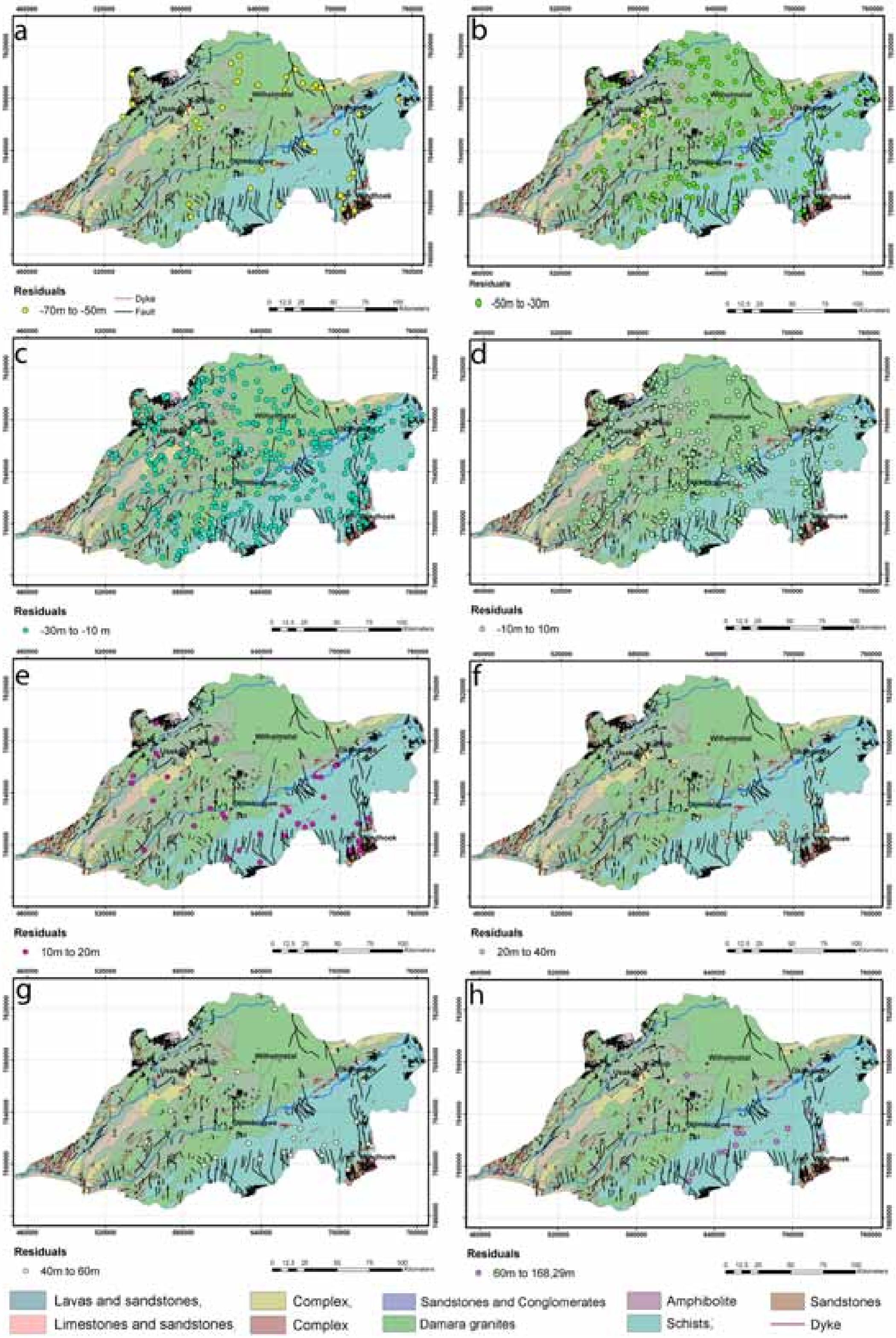

FIGURE 5.9: Ranges of residuals, Model 2 - maximum approach

5.2.3 Mass balance

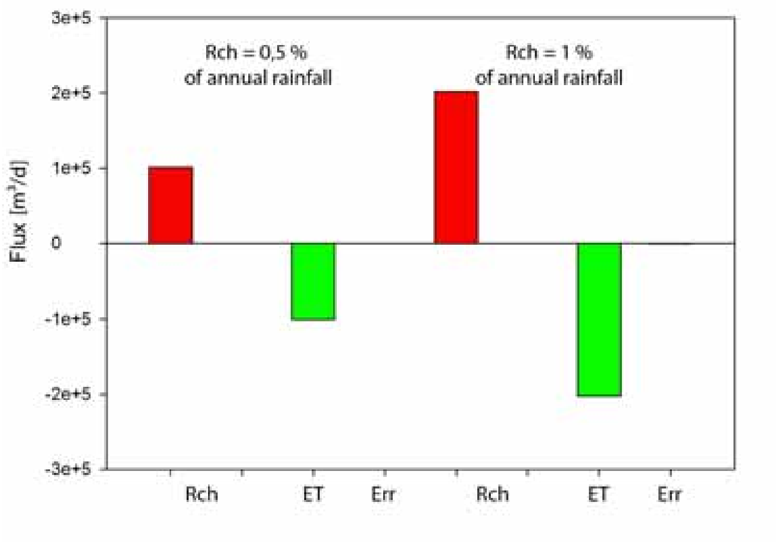

FIGURE 5.10: Mass balance summaries of Model 2

In Table 5.8 and 5.9 the model summaries of mass balances for the minimum and maximum approach are listed, specifying in- and outputs for each layer. Figure 5.10 is illustrating the total fluxes of each approach.

Minimum approach:

Inputs of the minimum approach of Model 2 are a recharge amount of $1.009{\cdot}10^5$ m^3/d equal to $36.87 \cdot 10^6$ m^3/a and a small inflow from the sea of 7.658 m^3/d (constant head). Outputs are evaporation with a value of 1.011 m^3/d and surface runoff of 25.6 m^3/d. So total input is $10.09 \cdot 10^4$ m^3 and total output $10.12{\cdot}10^4$ m^3, resulting in a total error of -0.297 % (Figure 5.10, Table 5.8).

TABLE 5.8: Mass balance summary Model 2 - minimum approach(fluxes in m^3/d)

Layer	1	2	3	4	5	6	7
Recharge in	$1.009{\cdot}10^5$						
Recharge out	$2.56{\cdot}10^1$						
ET out	$1.011{\cdot}10^5$						
Const. head	7.658						
Qz Top in		$4.49{\cdot}10^4$	$3.67{\cdot}10^4$	$2.86{\cdot}10^4$	$1.55{\cdot}10^4$	$5.14{\cdot}10^3$	$1.24{\cdot}10^3$
Qz Top out		$4.49{\cdot}10^4$	$3.67{\cdot}10^4$	$2.86{\cdot}10^4$	$1.55{\cdot}10^4$	$5.14{\cdot}10^3$	$1.24{\cdot}10^3$
Qz Bottom in	$4.49{\cdot}10^4$	$3.67{\cdot}10^4$	$2.86{\cdot}10^4$	$1.55{\cdot}10^4$	$5.14{\cdot}10^3$	$1.24{\cdot}10^3$	
Qz Bottom out	$4.49{\cdot}10^4$	$3.67{\cdot}10^4$	$2.86{\cdot}10^4$	$1.55{\cdot}10^4$	$5.14{\cdot}10^3$	$1.24{\cdot}10^3$	
IN	$1.46{\cdot}10^5$	$8.16{\cdot}10^4$	$6.54{\cdot}10^4$	$4.42{\cdot}10^4$	$2.07{\cdot}10^3$	$6.38{\cdot}10^3$	$1.24{\cdot}10^3$
OUT	$1.46{\cdot}10^5$	$8.16{\cdot}10^4$	$6.54{\cdot}10^4$	$4.42{\cdot}10^4$	$2.07{\cdot}10^4$	$6.38{\cdot}10^3$	$1.24{\cdot}10^3$
Total IN	100868.08						
Total OUT	101168.42						
Total Error	-0.297 [%]						

Maximum approach:
Within the maximum approach recharge is $2.017 \cdot 10^5$ m^3/d equal to $73.62 \cdot 10^6$ m^3/a, whereof 28.3 m^3/d are removed as surface runoff. The evaporation rate with a value of $2.023 \cdot 10^5$ m^3/d is slightly higher than the recharge rate. 7.656 m^3/d are flowing from the sea into the model domain (const. head cells). A total input of $20.17 \cdot 10^4$ m^3/d and a total output of $20.22 \cdot 10^4$ m^3/d produce a total water balance error of -0.25 %.

Table 5.9: Mass balance summary of Model 2 - maximum approach (fluxes in m^3/d)

Layer	1	2	3	4	5	6	7
Recharge in	$2.02 \cdot 10^5$						
Recharge out	$2.83 \cdot 10^1$						
ET out	$2.02 \cdot 10^5$						
Const. head	7.66						
Qz Top in		$1.01 \cdot 10^5$	$8.29 \cdot 10^4$	$6.49 \cdot 10^4$	$3.48 \cdot 10^4$	$1.15 \cdot 10^4$	$2.81 \cdot 10^3$
Qz Top out		$1.01 \cdot 10^5$	$8.29 \cdot 10^4$	$6.49 \cdot 10^4$	$3.48 \cdot 10^4$	$1.15 \cdot 10^4$	$2.81 \cdot 10^3$
Qz Bottom in	$1.01 \cdot 10^5$	$8.29 \cdot 10^4$	$6.49 \cdot 10^4$	$3.48 \cdot 10^4$	$1.15 \cdot 10^4$	$2.81 \cdot 10^3$	
Qz Bottom out	$1.01 \cdot 10^5$	$8.29 \cdot 10^4$	$6.49 \cdot 10^4$	$3.48 \cdot 10^4$	$1.15 \cdot 10^4$	$2.81 \cdot 10^3$	
IN	$3.03 \cdot 10^5$	$1.84 \cdot 10^5$	$1.48 \cdot 10^5$	$9.96 \cdot 10^4$	$4.62 \cdot 10^4$	$1.43 \cdot 10^4$	$2.81 \cdot 10^3$
OUT	$3.03 \cdot 10^5$	$1.84 \cdot 10^5$	$1.48 \cdot 10^5$	$9.96 \cdot 10^4$	$4.62 \cdot 10^4$	$1.43 \cdot 10^4$	$2.81 \cdot 10^3$
Total IN	201674.37						
Total OUT	202178.06						
Total Error	-0.25 [%]						

5.3 Model 3

This model combines recharge and evaporation concept 3 (Chapters 4.4.3 and 4.5.3) and the aquifer concept 2. Model 3 was developed, because flow paths of Model 2 indicated local to intermediate groundwater flow systems (Chapter 5.4). To account for this, the attempt was made to distinguish between recharge and discharge areas by the use of the topographic index. During calibration a boundary index was adjusted. Below results with a topographic boundary index of 12 are described, i.e. all indices lower than 12 represented recharge areas and indices higher than 12 discharge areas where evaporation zones were assigned.

5.3.1 Aquifer parameter

For the minimum and maximum approach the same hydraulic parameters were used, like in the minimum and maximum approach of Model 2 (Chapter 5.2.1) and therefore not explicitly listed here.

5.3.2 Model performance

In Figure 5.11 observed versus simulated groundwater levels for the minimum and the maximum approach are plotted. Figure 5.12 is showing residuals corresponding to observed water levels and Figure 5.13 the location of positive and negative residuals within layer 1. Calibration statistics are listed in Table 5.10.

TABLE 5.10: Calibration statistics of model 3

	min. approach	max. approach
Residual Mean	-7.30 m	-10.36 m
Res. Std. Dev.	33.29 m	26.99 m
Min. Residual	-71.78 m	-70.07 m
Max. Residual	213.24 m	170.13 m
Range in Target Values	1885 m	1885 m
MAE	23.64 m	21.72 m
RMS	34.06 m	28.89 m
R^2	0.985	0.992

Minimum approach:

The scatter plot in Figure 5.11 indicates the largest residuals in low and high elevations, whereas in moderate elevations the best fits are achieved. The most negative residual with a value of -71.78 m (red arrow) and the most positive residual (black arrow) with a value of 213.24 m are located similarly as in the minimum approach of Model 2 (Figure 5.13). The residual mean is -7.3 m and the residual standard deviation 33.29 m. MAE and RMS values are 23.4 m and 34.06 m, respectively with a coefficient of determination of R^2=0.985.

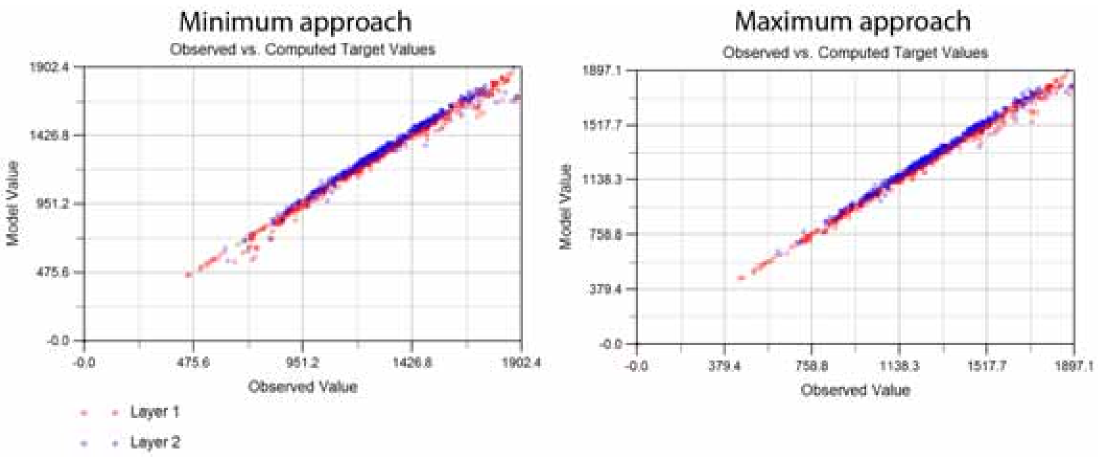

FIGURE 5.11: Observed vs. simulated heads - Model 3

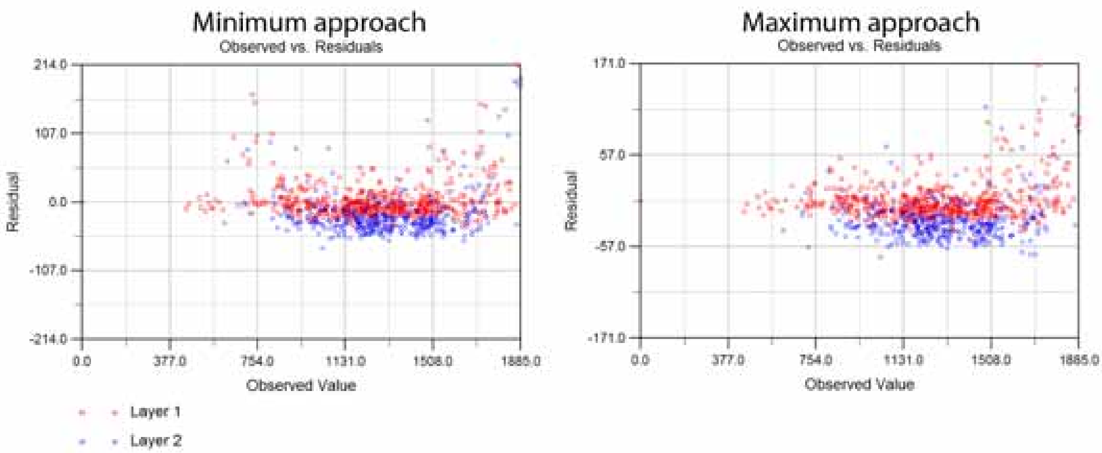

FIGURE 5.12: Observed heads vs. residuals - Model 3

Maximum approach:
While showing best fits in low elevations, the largest scattering in Figures 5.11 and 5.12 occurs in higher elevations. The most positive (170.13 m, black arrow) and negative (-70.07 m, red arrow) residuals are located at the same place as in the maximum approach of Model 2 (Figure 5.13). The residual mean is -10.36 m and the residual standard deviation 26.99 m. The MAE has a value of 21.72 m, the RMS a value of 28.89 m and R^2 is 0.990.

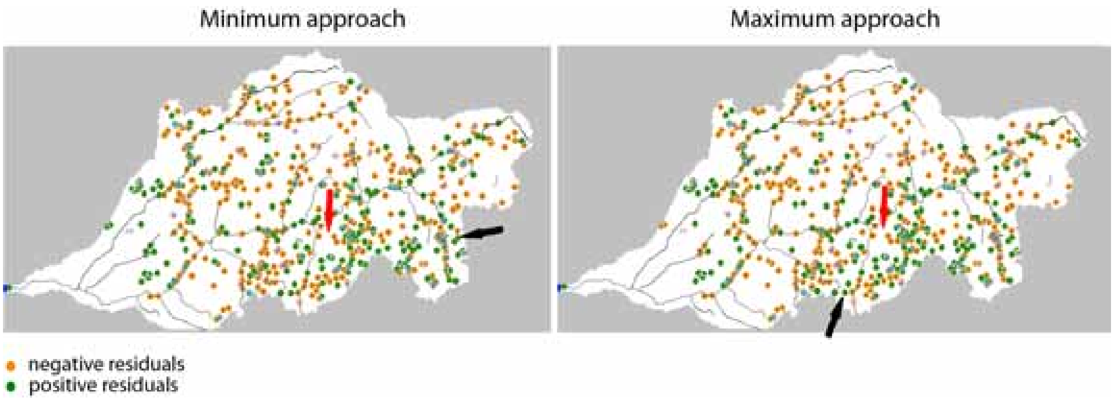

FIGURE 5.13: Residual circles - Model 3

5.3.3 Mass balance

As shown in Figure 5.14 in the minimum as well as in the maximum approach, evaporation did not compensate for the input amount and a large surface runoff occurred. In Table 5.11 and 5.12 the model summaries of mass balances for the minimum and maximum approach are listed, specifying in- and outputs for each layer.

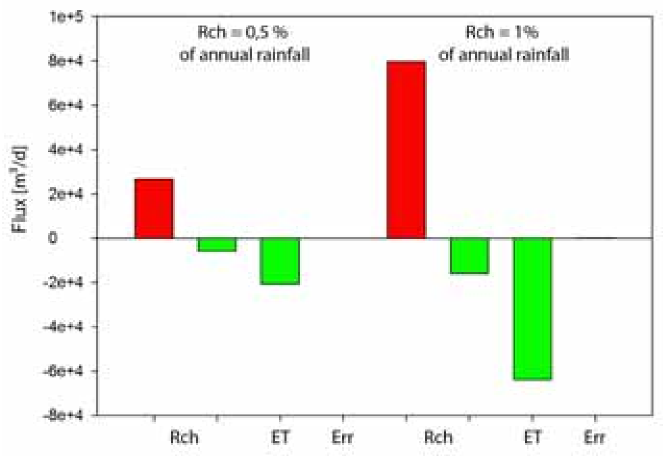

FIGURE 5.14: Model summary of mass balance Model 3

Minimum approach:
As shown in Table 5.11 the recharge rate is $2.66{\cdot}10^4$ m^3/d equal to $9.71{\cdot}10^6$ m^3/a. Outputs are evaporation and surface runoff with rates of $2.08{\cdot}10^4$ m^3/d and 5790 m^3/d, respectively. 7.65 m^3/d are flowing in from the sea (const. head cells). Combined, total inputs are 26564.97 m^3/d and total outputs 26611.96 m^3/d, resulting in a total water balance error of -0.177 %.

TABLE 5.11: Mass balance summary Model 3 - minimum approach

Layer	1.00	2	3	4	5	6	7
Recharge in	$2.66{\cdot}10^4$						
Recharge out	$5.79{\cdot}10^3$						
ET out	$2.08{\cdot}10^4$						
Const. head	7.65						
Qz Top in		$2.52{\cdot}10^4$	$2.19{\cdot}10^4$	$1.81{\cdot}10^4$	$1.07{\cdot}10^4$	$3.69{\cdot}10^3$	$9.09{\cdot}10^2$
Qz Top out		$2.52{\cdot}10^4$	$2.19{\cdot}10^4$	$1.81{\cdot}10^4$	$1.07{\cdot}10^4$	$3.69{\cdot}10^3$	$9.09{\cdot}10^2$
Qz Bottom in	$2.52{\cdot}10^4$	$2.19{\cdot}10^4$	$1.81{\cdot}10^4$	$1.07{\cdot}10^4$	$3.69{\cdot}10^3$	$9.09{\cdot}10^2$	
Qz Bottom out	$2.52{\cdot}10^4$	$2.19{\cdot}10^4$	$1.81{\cdot}10^4$	$1.07{\cdot}10^4$	$3.69{\cdot}10^3$	$9.09{\cdot}10^2$	
IN	$5.18{\cdot}10^4$	$4.71{\cdot}10^4$	$4.00{\cdot}10^4$	$2.87{\cdot}10^4$	$1.43{\cdot}10^4$	$4.60{\cdot}10^3$	$9.09{\cdot}10^2$
OUT	$5.18{\cdot}10^4$	$4.71{\cdot}10^4$	$4.00{\cdot}10^4$	$2.87{\cdot}10^4$	$1.43{\cdot}10^4$	$4.60{\cdot}10^3$	$9.09{\cdot}10^2$
Total IN	26564.97						
Total OUT	26611.96						
Total Error	-0.177 [%]						

Maximum approach:

Mass balance of the maximum approach shows a similar picture compared to the mass balance of the minimum approach. Recharge flux is $7.97{\cdot}10^4$ m^3/d equal to 29.09 $\cdot 10^4$ m^6/a. Evaporation takes place with a rate of $2.08{\cdot}10^4$ m^3/d. The recharge rate that did not enter the model domain is $1.58{\cdot}10^4$ m^3/d. Furthermore 7.65 m^3/d are flowing in from the Atlantic Ocean (Table 5.12).

TABLE 5.12: Mass balance summary Model 3 - maximum approach

Layer	1	2	3	4	5	6	7
Recharge in	$7.97{\cdot}10^4$						
Recharge out	$1.58{\cdot}10^4$						
ET out	$6.38{\cdot}10^4$						
Const. head	7.65						
Qz Top in		$7.55{\cdot}10^4$	$6.54{\cdot}10^4$	$5.34{\cdot}10^4$	$3.06{\cdot}10^4$	$1.05{\cdot}10^4$	$2.61{\cdot}10^3$
Qz Top out		$7.55{\cdot}10^4$	$6.54{\cdot}10^4$	$5.34{\cdot}10^4$	$3.06{\cdot}10^4$	$1.05{\cdot}10^4$	$2.61{\cdot}10^3$
Qz Bottom in	$7.55{\cdot}10^4$	$6.54{\cdot}10^4$	$5.34{\cdot}10^4$	$3.06{\cdot}10^4$	$1.05{\cdot}10^4$	$2.61{\cdot}10^3$	
Qz Bottom out	$7.55{\cdot}10^4$	$6.54{\cdot}10^4$	$5.34{\cdot}10^4$	$3.06{\cdot}10^4$	$1.05{\cdot}10^4$	$2.61{\cdot}10^3$	
IN	$1.55{\cdot}10^5$	$1.41{\cdot}10^5$	$1.19{\cdot}10^5$	$8.40{\cdot}10^4$	$4.11{\cdot}10^4$	$1.31{\cdot}10^4$	$2.61{\cdot}10^3$
OUT	$1.55{\cdot}10^5$	$1.41{\cdot}10^5$	$1.19{\cdot}10^5$	$8.40{\cdot}10^4$	$4.11{\cdot}10^4$	$1.31{\cdot}10^4$	$2.61{\cdot}10^3$
Total IN	79667.09						
Total OUT	79649.53						
Total Error	0.02 [%]						

5.4 Groundwater flow system

The maximum approach of Model 2 was used to analyze the groundwater flow paths. In Figure 5.17 the positions of cross and longitudinal sections as well as river compartments are shown.
Figure 5.15 illustrates groundwater contour lines (green) and velocity vectors within layer 2 (top elevation 25 m b.g.l.) (note that velocity vectors are in logarithmic scale and exaggerated). Red and blue arrows indicate downward and upward fluxes, respectively. Areas of divergence of these vectors are recharge areas and areas of convergence are discharge areas (*Ophori*, 2007). In general, convergence occurs in the river valleys (denoted as black lines) and divergence on hills and higher elevations (some of them marked with a R in Figure 5.15). Conspicuous are upward vectors and a common convergence near the outlet. The shape of the equipotentials along the major river reaches changes significantly from higher to lower elevations. While being almost straight, especially along the Khan River in the north of Wilhelmstal they get sharper in the downstream direction. Another conspicuity are the groundwater mounds located on a line from Wilhelmstal to the south west and the associated divergence of velocity vectors.

In Figure 5.16 velocity vectors in layer 1 are plotted on the hydrogeological map (*DWA & GSN*, 2001). Groundwater flow directions, denoted as purple arrows in the hydrogeological map, fit in general to the simulated flow directions. Also some of the springs, signed as purple and orange circles, can be linked to converging velocity vectors, e.g. thermal spring in the south-west of Okahandjia (S1), the springs downstream of Swakoppoort Dam (S2), the spring located near the Umbujosare stream (S3), the submonatane spring at the Witwaters Mountains in the south west (S4) (Figure 5.16).
Four longitudinal sections and four cross sections are given in Figure 5.19 and Figure 5.18 (see positions in Figure 5.17). In general troughs and river valleys in the longitudinal and in the cross sections display areas where upwelling of groundwater occurs. Exemptions are observed in the longitudinal section R3 (Figure 5.19), where velocity vectors in the Windhoek Graben display decurrent fluxes. Furthermore, the longitudinal section R4, which is going through the outlet, is indicating an upward movement of groundwater at the saltwater-freshwater interface.

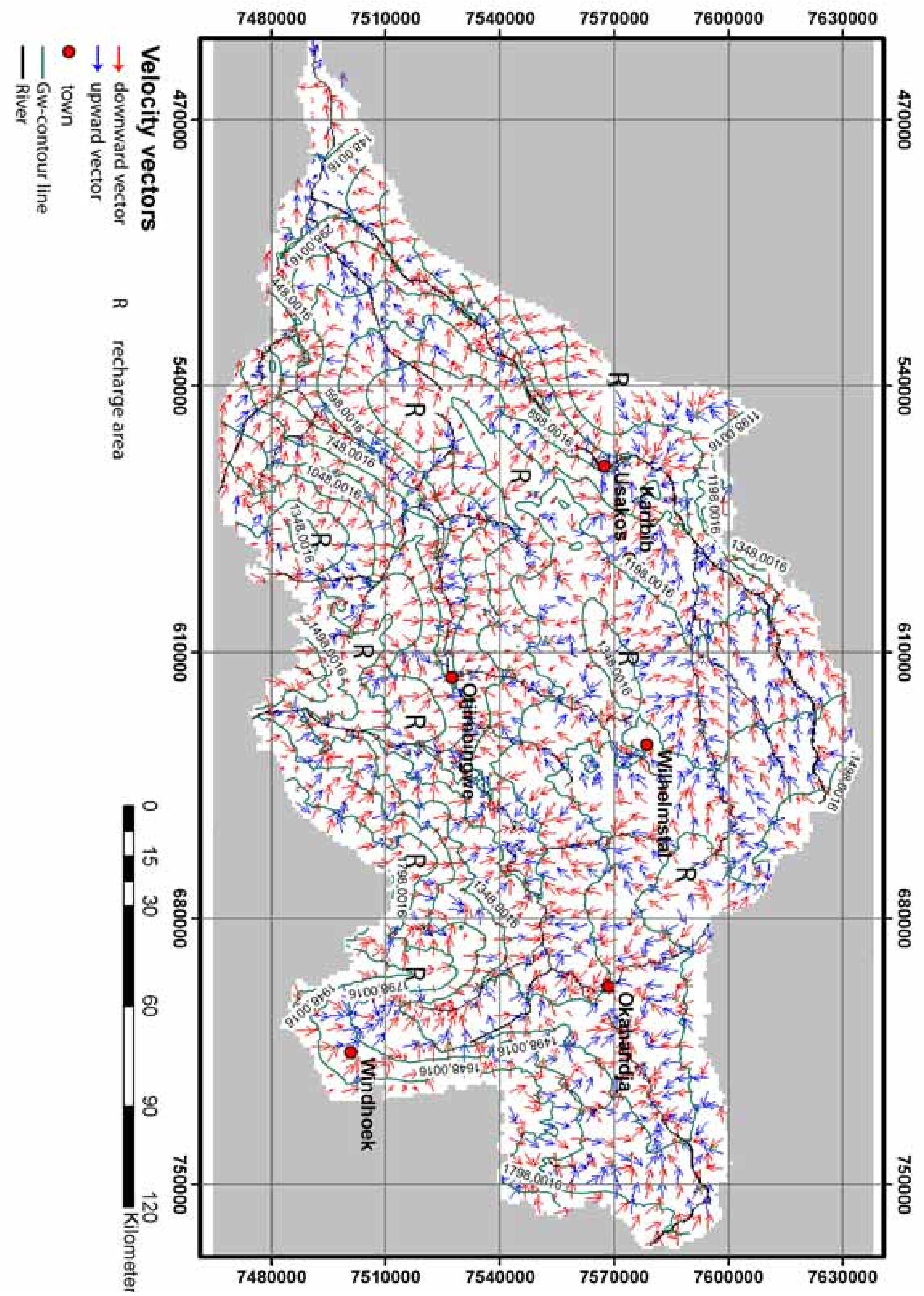

FIGURE 5.15: Simulated flow pattern in the horizontal plane of layer 2

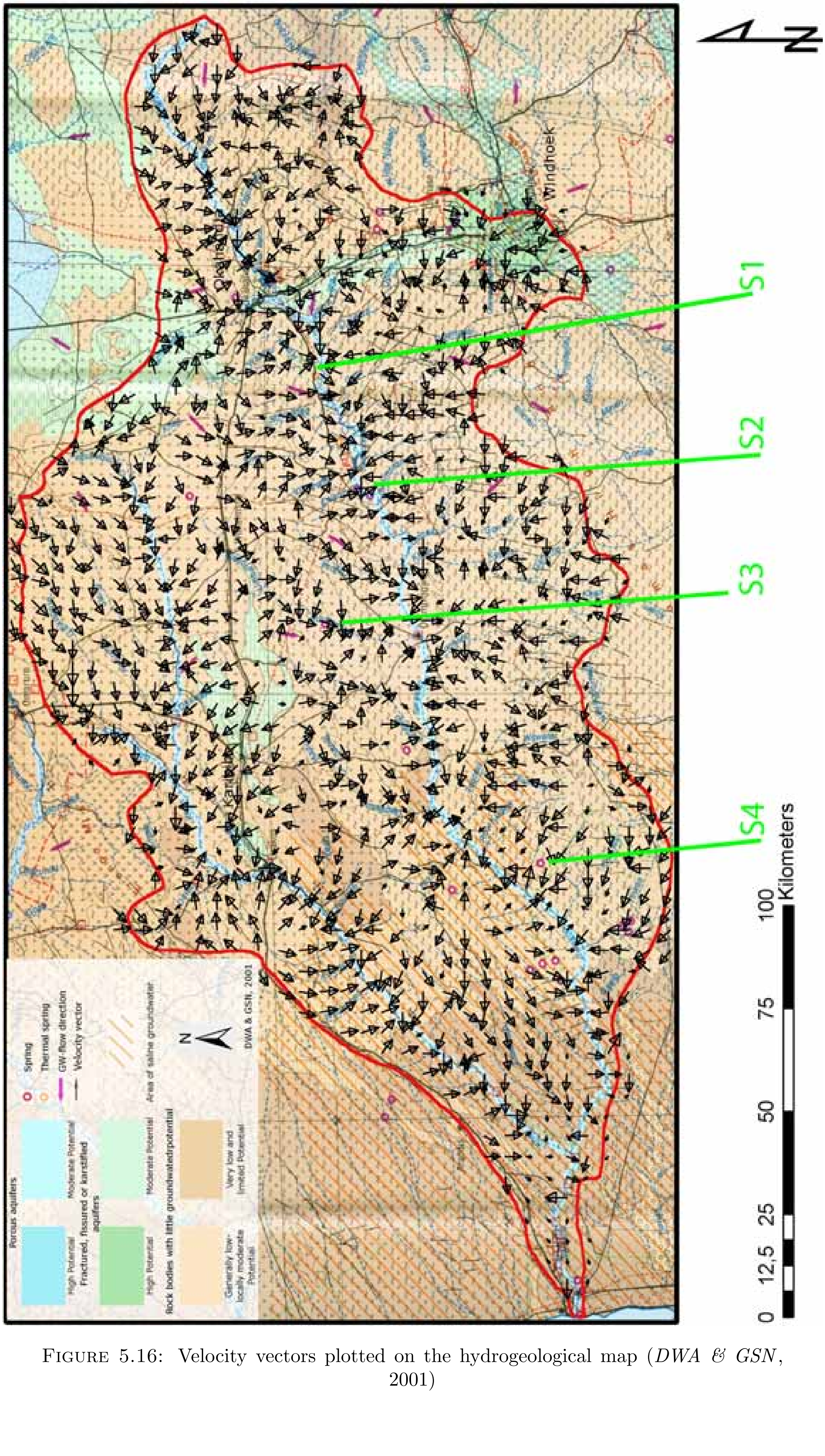

FIGURE 5.16: Velocity vectors plotted on the hydrogeological map (*DWA & GSN*, 2001)

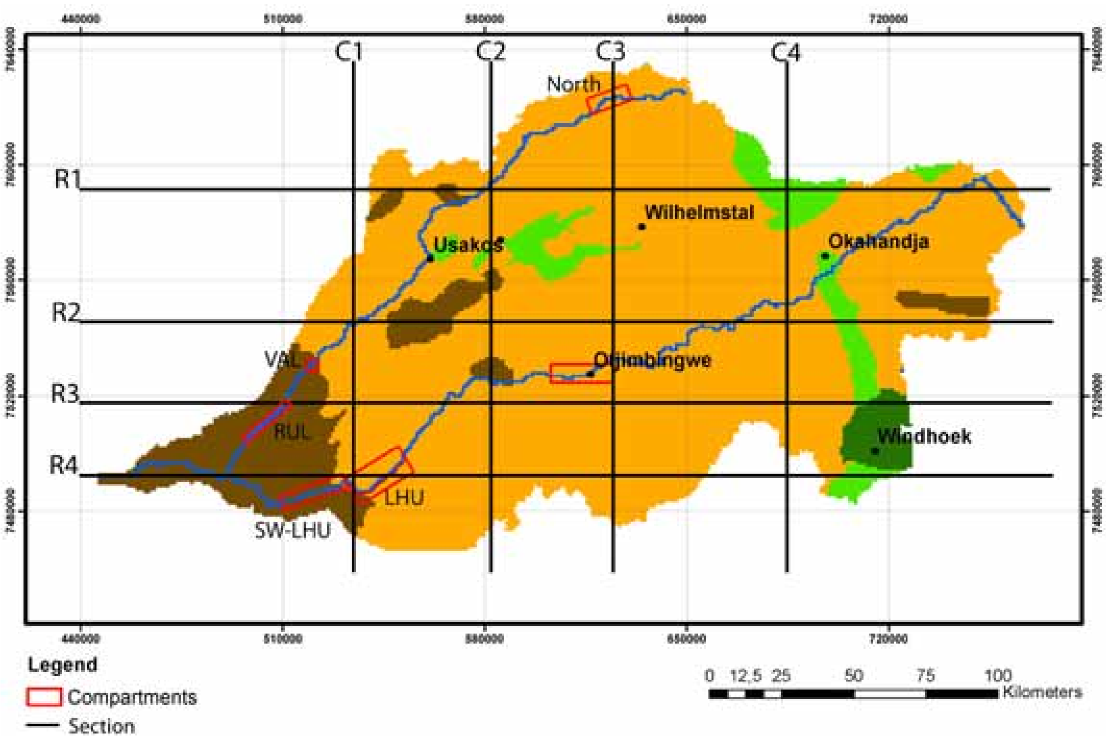

FIGURE 5.17: Selected sections and river compartments

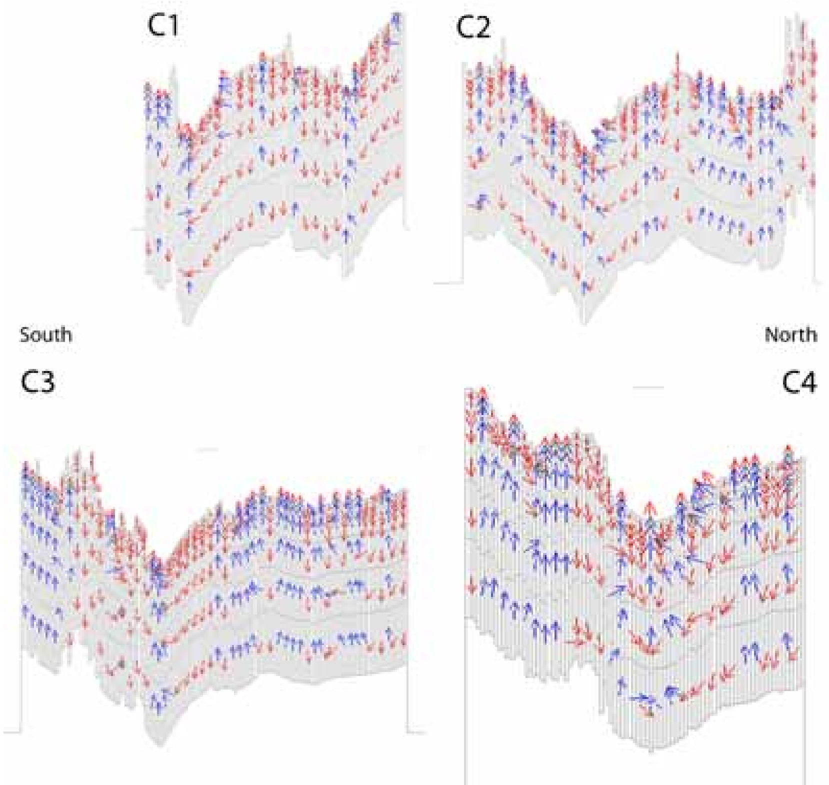

FIGURE 5.18: Simulated flow patterns in cross sections (position in Figure 5.17)

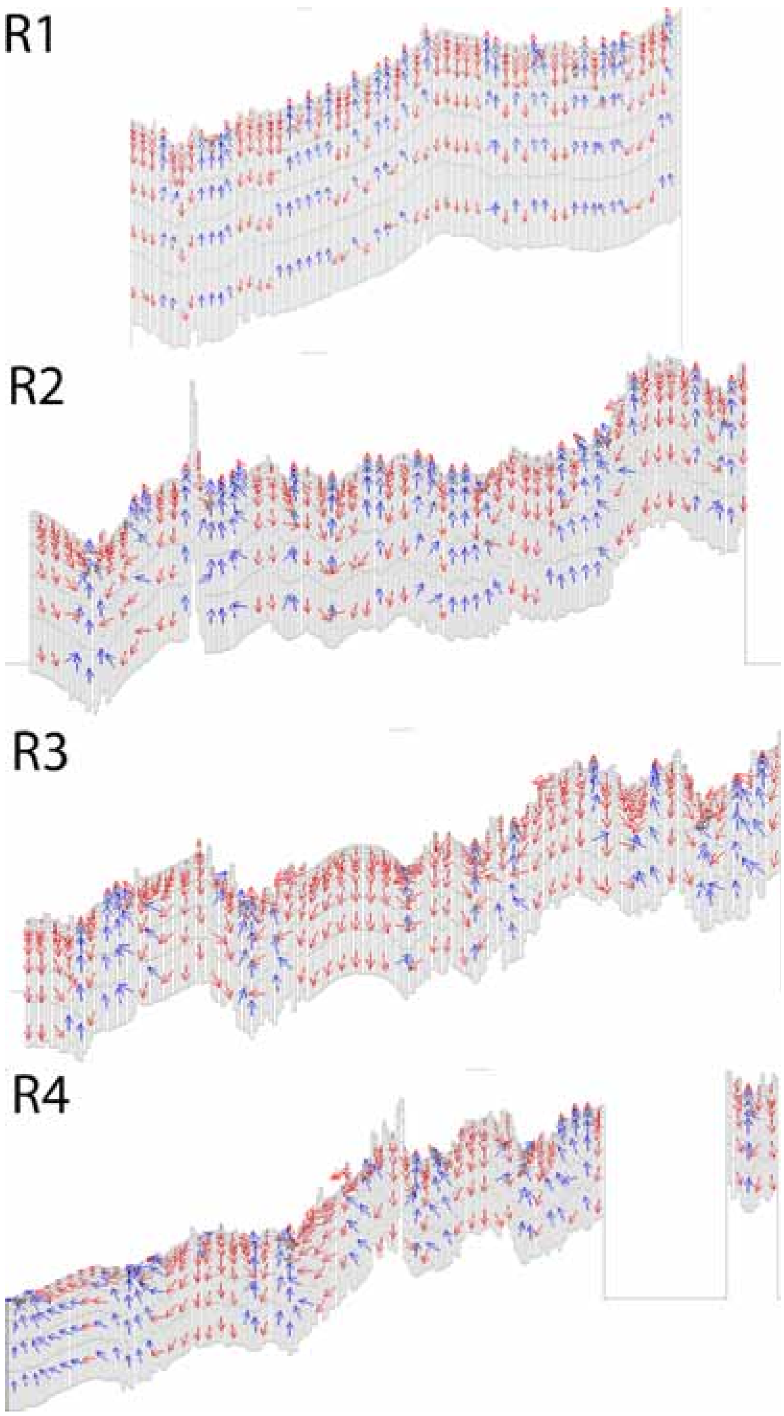

Figure 5.19: Simulated flow pattern in the vertical east-west section (see position in Figure 5.17)

Particle tracking analysis:

A particle tracking analysis was performed near the outlet of the basin in the zone of saline groundwater (location illustrated in the hydrogeological map, Figure 3.9) using the MODPATH module (*Pollock*, 1994) within Groundwater Vistas (*Rumbaugh & Rumbaugh*, 2007).

Particle circles were placed in layer 1, 2, 3, 5, and 7 at different locations and reverse computation was conducted. In Figure 5.20 the pathways are illustrated and medial travel times listed. The majority of the flow pathways produced by particle tracking analysis with starting locations in layer 1, depict short distances between entrances and exits ($\approx$ 1-5 km). Many of them are rather shallow and reach down to layer 3 and 4 (max. 100 - 200m). But also longer pathways were computed with an origin of approximately 30 km eastward from their exits, reaching down to layers 5 and 6. Particles placed very close to the outlet, north of the Swakop river, infiltrated in north easterly direction at the border of the basin and have horizontal distances between entrances and exits of about 20 km. The medial travel time computed for the particles placed in layer 1 is 36299 a.

Particles applied to layer 2 show a similar picture. Short distances between entrances and exits of about 1-3 km prevail and a few flow pathways occur with horizontal length of 10-13 km. Medial travel time from their entrance to their appearance in layer 2 is 9555 a.

Particle tracking analysis with particles put in layer 3 have a medial travel time of 46749 a, following from distances between origin and occurrence in layer 3 of about 10 km near the outlet and larger ones of approximately 30 km with entrances in higher elevations.

The origins of particles placed close to the outlet in layer 5 and 7 are equally located like those produced by particles placed in layer 1 and are located at the basin border north of the convergence of the Swakop and Khan Rivers.

Furthermore the ridge (Chuos Mountains) between the rivers as well as the area between the Langer Heinrich and the Witwaters Mountains (starting layer 5) indicate recharge areas for these particles. Medial travel time calculated for particles placed in layer 5 is 366915 a.

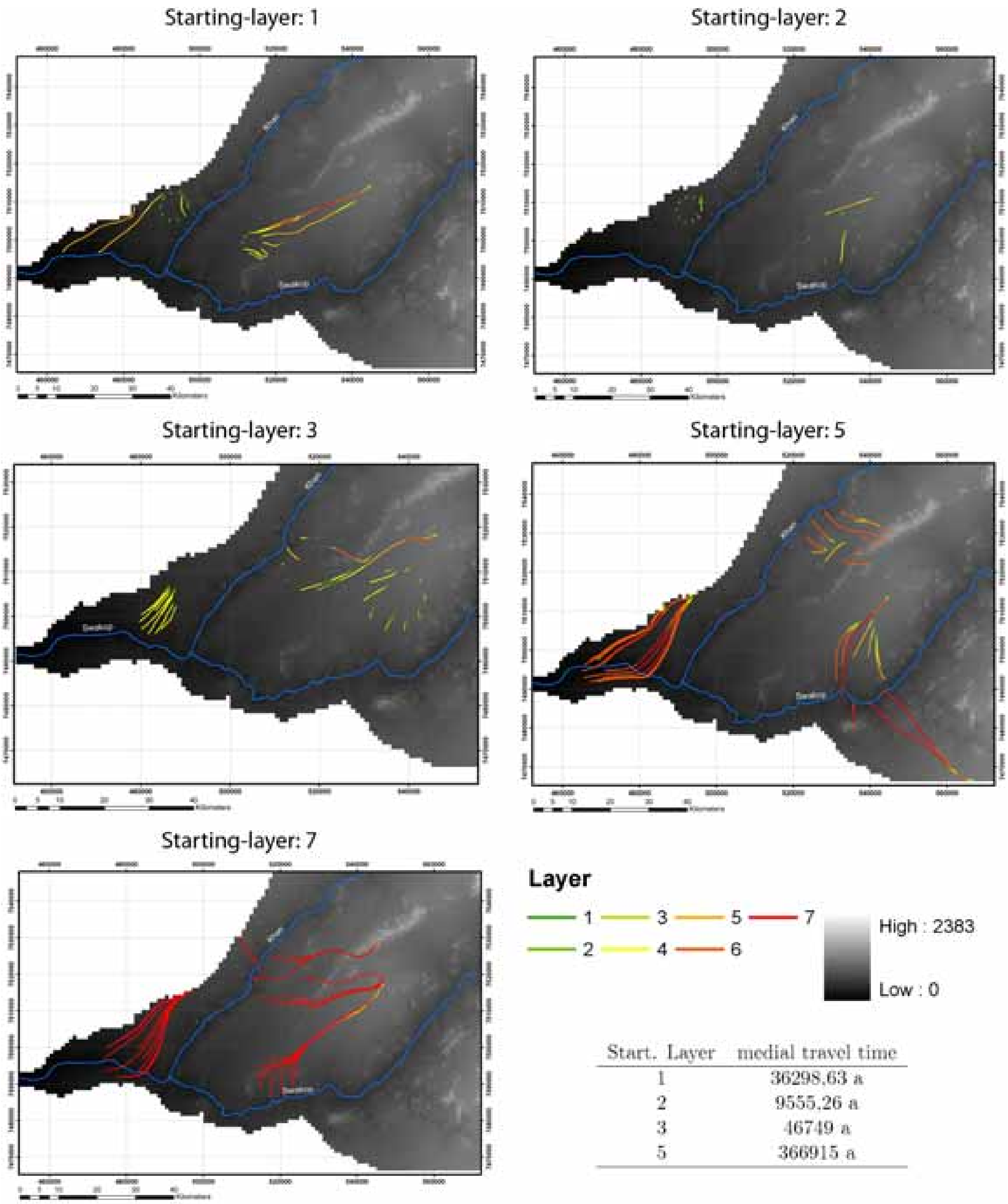

Start. Layer	medial travel time
1	36298.63 a
2	9555.26 a
3	46749 a
5	366915 a

FIGURE 5.20: Pathways produced by particle tracking analysis in the zone of saline groundwater

A particle tracking analysis was also applied to produce flow paths at the thermal springs located between the Swakoppoort Dam and the Von Bach Dam. Six particles were set at the surrounding cells and flow pathways were computed reversely (Figure 5.21). The spring in the vicinity of the Swakoppoort Dam is dominated by short pathways and travel times, however, one cell of the thermal spring in the southwest of the Von Bach Dam illustrates deeper and longer groundwater path ways. Three particle circles (each with 10 particles) were set to this cell (row: 86, column: 234) and medial travel time calculated, resulting in a value of 644115 a and pathways reaching down to the bottom of layer 6 (650 m b.g.l.).

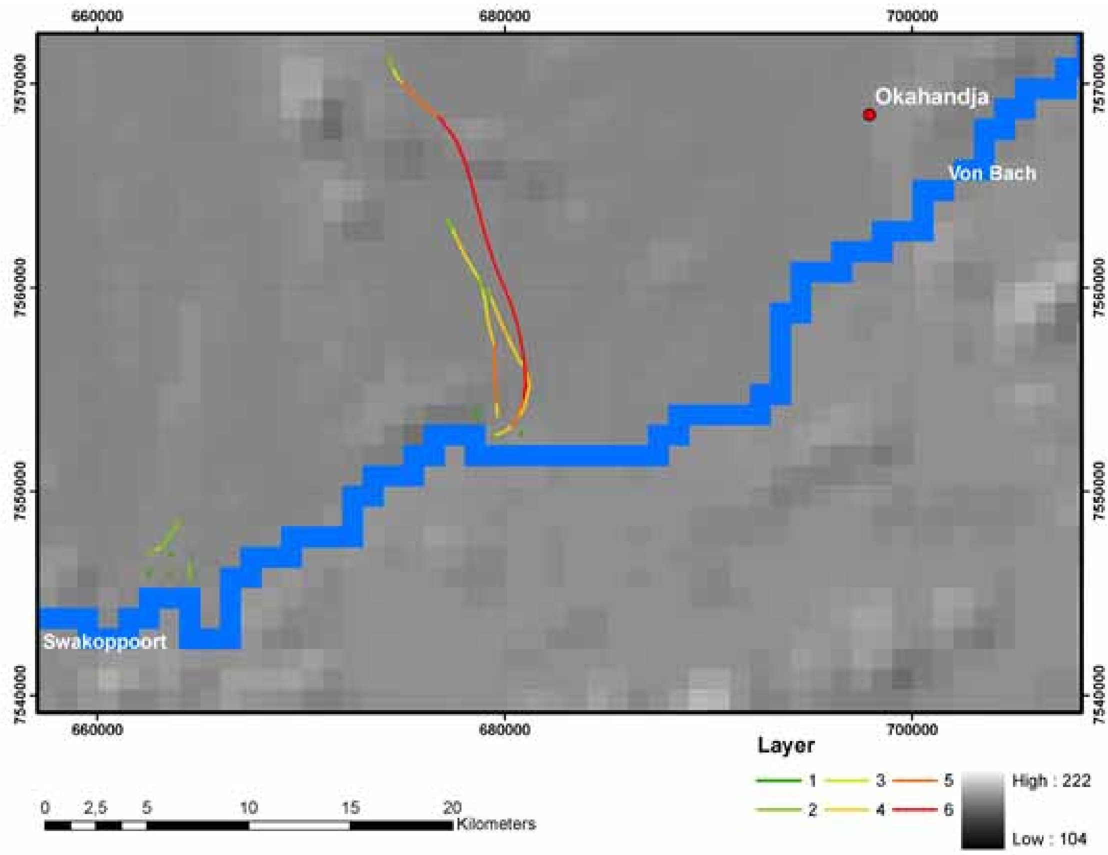

FIGURE 5.21: Flow paths to thermal springs

5.5 River compartments

Six river compartments (three in the Swakop and three in the Khan River) were selected and investigated. The positions are shown in Figure 5.17. Mass balances were computed and particle tracking analyses were conducted to trace the flow pathways, horizontal distances and travel times. Particles were set to the bottom of layer 1 in the alluvial aquifers and tracked reverse from their exit to their entrance locations.
Mass balances are listed in Table 5.14 (note, only vertical fluxes are listed) and illustrated in Figure 5.22.
Determining the influence of basement water fluxes on the alluvial aquifers was achieved by the application of four indicators (I) described in Chapter 2.5. Values are listed in Table 5.13 and Figure 5.23 depicts the indicators in comparison.

TABLE 5.13: Flux - indicators for the selected river compartments

Indicator	RUL	VAL	North	SW-LHU	LHU	Otjimb.
I1: Total In - Rch/Total In	0.79	0.95	0.93	0.88	0.97	0.82
I2: Bottom In/ Total In	0.68	0.54	0.08	0.77	0.71	0.67
I3: Bottom in/Total In-Rch	0.88	0.56	0.09	0.88	0.73	0.82
I4: ET/Total In	0.65	0.98	0	0.87	0.97	0.70

Khan River:
In the RUL compartment (26 km^2) direct recharge inflow is 15.3 m^3/d and evaporation outflow is 44.6 m^3/d. Bottom inflow represents the largest flux occurring, with an amount of 47.3 m^3/d. 20.96 m^3/d are percolating into layer 2 (bottom out), resulting in total in- and outputs of around 69.1 and 69.3 m^3/d. As shown in Figure 5.22 smaller horizontal inputs enter the compartment mainly from the north and the east, while water is mainly draining to the east and west. The ratio of basement fluxes to all inflows (Indicator I1) is 0.79. The fraction of vertical inflow from the basement to total inflow (I2) is 0.68; I3 (the ratio of vertical inflow from the basement to total basement inflow) has a value of 0.88 and I4 (the measure for evaporation influence) has value of 0.65 (Table 5.13).

The VAL compartment, with an area of 9 km^2, is characterized by a large horizontal input from the north as well as a large evaporation rate of 278.31 m^3/d. Bottom inflow occurs with a rate of 151.72 m^3/d and bottom outflow with 4.45 m^3/d, while direct recharge inflow is 13.3 m^3/d. Furthermore small influxes come from all horizontal directions, while output besides evaporation occurs through the bottom. Indicator values listed in Table 5.13 are: I1: 0.95; I2: 0.54; I3: 0.56 and I4: 0.98.
The compartment located in the north of Wilhelmstal and denoted North (10 km^2), gets inputs through direct recharge (77,06 m^3/d) and the bottom (100 m^3/d).

The largest input is coming from the north ($\approx$ 1000 m^3/d). Evaporation does not take places. Indicator values listed in Table 5.13 are: I1: 0.93; I2: 0.08; I3: 0.09 and I4: 0.

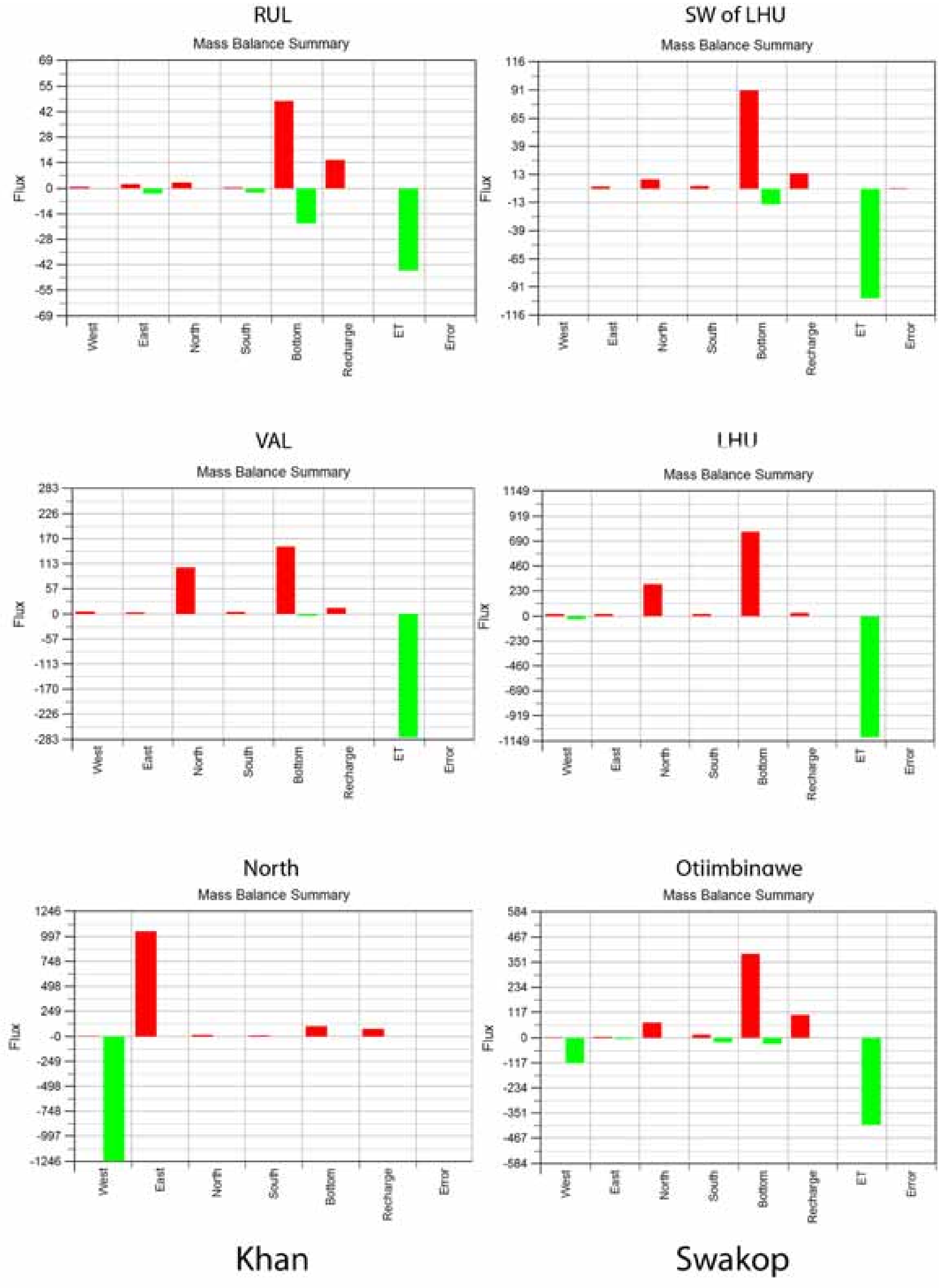

FIGURE 5.22: Mass balances of river compartments

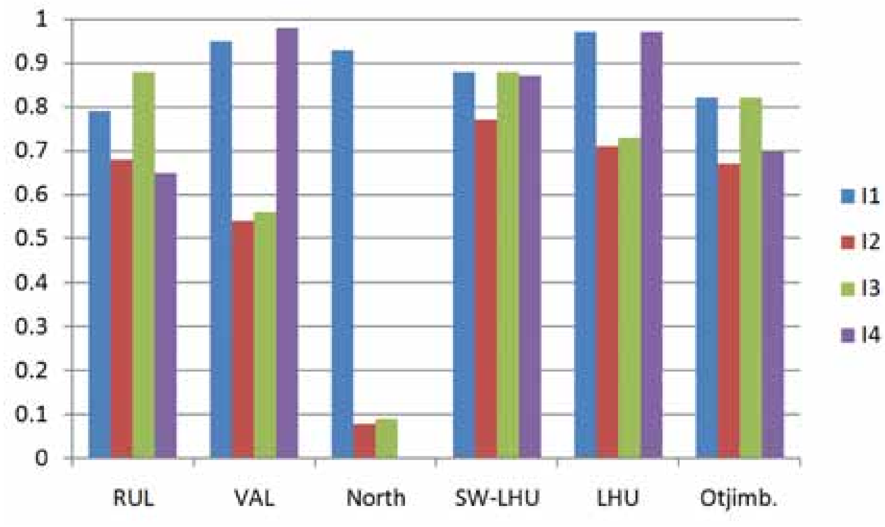

FIGURE 5.23: Indicators by comparison

Swakop River:

The mass balance of the compartment lying in the southwest of the LHU compartment (SW in Figure 5.17), with an area of 22 km^2, is made up by a direct recharge inflow of 14.4 m^3/d, by an evaporation rate of 101.14 m^3/d, by a bottom inflow of 89.82 m^3/d and a bottom outflow of 14.87 m^3/d. The largest horizontal inflow comes from the north, the largest horizontal output flux takes place in southern direction. Indicator values listed in Table 5.13 are: I1: 0.88; I2: 0.77; I3: 0.88 and I4: 0.87.

The mass balance of the LHU compartment (31 km^2) is characterized by a large evaporation amount of 997.2 m^3/d, by a bottom outflow of 4.65 m^3/d, by a recharge amount of 28.28 m^3/d and by a bottom inflow of 727.05 m^3/d. Outlined here are horizontal fluxes from all directions presenting small sources. Indicator 1 has a value of 0.97. I2 is 0.71, I3 is 0.73 and I4 has value of 0.97 (Table 5.13).

The Otjimbingwe compartment (26 km^2) gets vertical inputs through direct recharge and bottom inflow with rates of 106.78 m^3/d and 390 m^3/d, respectively. Horizontal inputs stem mainly from the north and horizontal outflow takes place to the south and mainly to the west. Evaporation was computed as 406.02 m^3/d and bottom outflow as 30.2 m^3/d. Indicator values listed in Table 5.13 are: I1: 0.82; I2: 0.67; I3: 0.82 and I4: 0.70.

Table 5.14: Mass balances of the river compartments (all fluxes in m^3/d)

	Khan			Swakop		
	RUL	VAL	North	SW of LHU	LHU	Otjimbingwe
Area [km^2]	26	9	10	22	31	26
Recharge inflow	15.3	13.3	77.06	14.4	28.28	106.78
ET outflow	44.60	278.31	0.00	101.14	997.2	406.02
Qz Bottom inflow	47.30	151.72	100	89.82	727.05	390
Qz Bottom outflow	19.1	4.45	0.00	14.87	4.65	30.2
Total IN	69.1	282.77	1246.1	116.37	1025.03	584.28
Total OUT	69.3	282.87	1246.1	116.25	1025.19	584.35

Particle tracking analyses:

Khan River:

As aforementioned, the MODPATH module (*Pollock*, 1994) was used and reverse tracking applied.

The particle tracking analysis in the RUL compartment, located in hard rock bodies with low to limited groundwater potential (Figure 5.17 and 4.15) produced medial travel times of 84796 a (95th percentile of 722202 a) with an average horizontal distance of 5411 m between entrance and exit of the particles (Table 5.15). As illustrated in Figure 5.24 flow paths go as deep as layer 5 (max. 400 m b.g.l., orange line) in general, only the largest flow path occurs in layer 7. Furthermore recharge areas are mainly located in the north of this compartment and distributed along the river reach.

A similar picture was produced in the VAL compartment, also located in the conceptual aquifer zone with low to limited groundwater potential. With an average horizontal distance of 6428 m between entrances and exits of the particles and a medial travel time of 66149 a and a 95th percentile of 332759 a, the deepest layer particles mainly travel through is layer 5.

In contrast particle analysis in the compartment north of Wilhelmstal produced shorter medial travel times (12897 a; 95th percentile: 24226 a) and horizontal distances between recharge and discharge (3751 m). Also the majority of flow paths do not go as deep as layer 4 (max. 200m b.g.l.), only the longest flow paths initiated in the north east appear in layer 5,6 and 7.

Swakop River:

Also situated in the aquifer zone with low to limited groundwater potential, the compartment in the southwest of the LHU compartment (SW) (not shown in Figure 5.24) receives water mainly from the north, by flow paths with medial travel times of 55384 a (95th percentile: 722202 a). The average horizontal distance between recharge and discharge is 4079 m.

Flow paths go as deep as layer 6 (max. 650 m b.g.l.), nevertheless the majority up to layer 5.
In the LHU compartment flow paths are characterized by medial travel times of 51669 a and a large average distance between entrances and exits of particles of 13420 m. Conspicuous are the origins of large and deep flow paths in the north of the river, located in adjacencies and diverging toward the river. Flow paths located in the southwest of the river are in general deeper and longer than those in the north. Their origin can be divided into a southern and a south western area.
The particle tracking analysis in the Otjimbingwe compartment produced medial travel times of 17798 a (95th percentile: 631781 a) with an average horizontal distance of 5030 m between entrance and exit of the particles. Furthermore, flow paths are mainly located in the north and are rather shallow and shorter compared to those two occurring in the south with origins in the schists of the Khomas Highland.

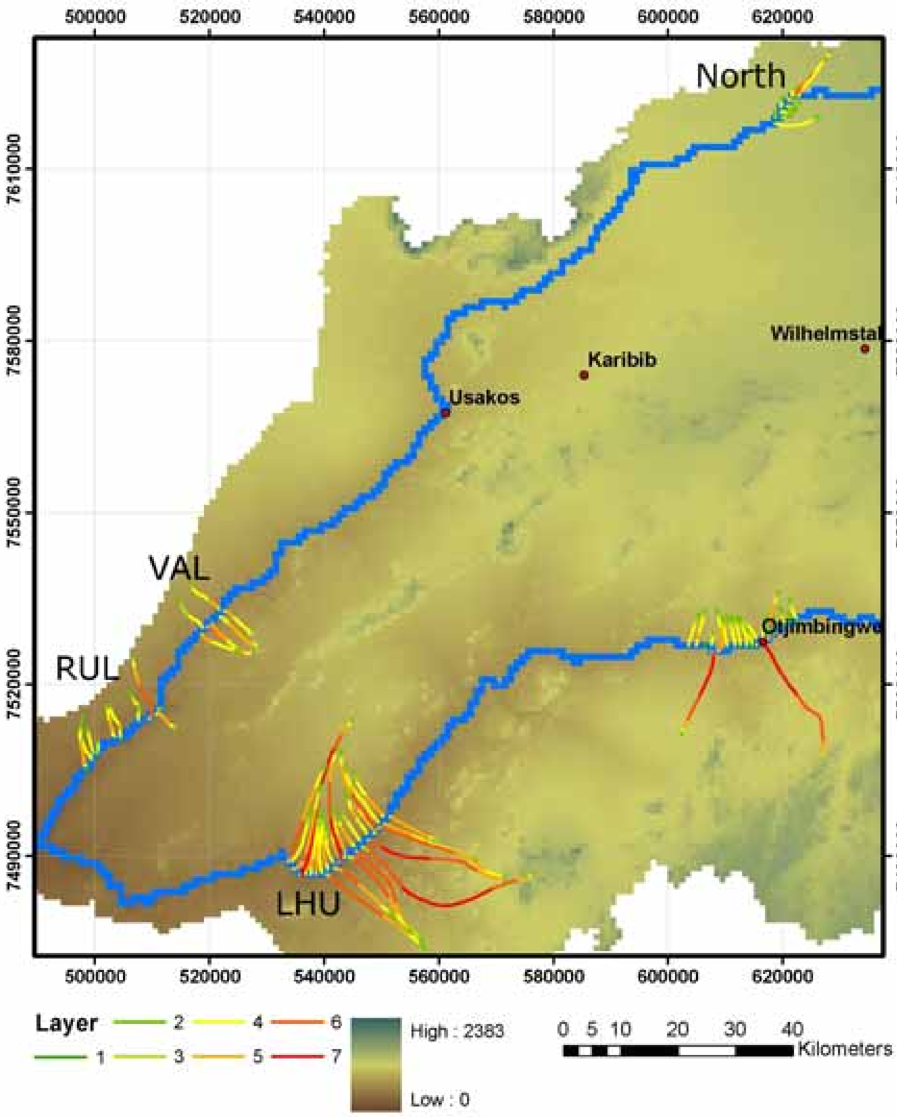

FIGURE 5.24: Particle tracks illustrating flow systems

Table 5.15: Travel times and average horizontal distances between entrances and exits of particles

	RUL	VAL	North	SW	LHU	Otjim.
Av. horiz. dist.	5411 m	6428 m	3751 m	4079 m	13420 m	5030 m
Med. Travel Time	84795.6a	66149.3 a	12897 a	55383.8 a	51668.8 a	17797.9 a
95th Percentile	722202 a	332758.9 a	24225.6 a	722202 a	1.2 Ma	631780.8 a

Chapter 6

Discussion

Since Model 2 was adopted for investigations, in the following the results of Model 1 and Model 3 will be summarized briefly and a detailed discussion will be undertaken for Model 2.

6.1 Model 1

Model 1 (Chapter 5.1), developed to get an initial insight in magnitudes of average basin wide hydraulic parameters, neglected recharge distribution and discretization based on hydrogeological properties. However, recharge rates of the minimum and maximum approach with rates of $35 \cdot 10^6$ m^3/a (1.19 mm/a) and $71.18 \cdot 10^6$ m^3/a (2,43 mm/a) are marginally smaller than those obtained with recharge concept 2 (Chapter 4.4.2). Basin wide hydraulic conductivities within both approaches ($8.25 \cdot 10^{-4}$ m/d and $8.47 \cdot 10^{-3}$ m/d) of Model 1 fall into the range of reported literature values and can be classified as slightly permeable (*Balke*, 2000).
The most negative residual of the minimum approach occurs at the same location as with the other models and seems to be associated with the interface between the intruded Donkerhoek granite and the schists of the Kuiseb Formation. The location of the most negative residual of the maximum approach located south of Windhoek within sandstones of the Rehoboth Group (Figure 5.3) was not confirmed by the other models due to the implementation of the fractured aquifer zone (fractured aquifer with high potential). The most positive residuals of both approaches are congruent and can be attributed to a very low permeability of the bedrock at this location. Nevertheless Model 1 produces comparable performances to the other models according to the RMS of 27.9 m and 34.99 m and the MAE of 22.25 m and 25.05 m for the minimum and maximum approach, respectively. The calculated water balance errors within this model are 0.18

% and 0.14 % for the minimum and maximum approach, respectivley. Since this simple model was built up without considering any hydrogeological discretization, it was not used for investigation, although it resulted in a minor water balance error and similar calibration statistics than Model 2.

6.2 Model 3

The implementation of the Topographic Index in Model 3 was based on the fact, that flow paths computed with Model 2 indicated local to intermediate flow systems. Furthermore, deactivating SURFACT´s recharge package RSF4 (*HydrogeologicInc.*, 2007) and using the RCH1 package of MODFLOW (*McDonald & Harbaugh*, 1988), ponding of water predominantly occurred in troughs and river valleys. This was interpreted as another indicator for a preponderance of local and/or intermediate groundwater flow systems.

By using the recharge and evaporation concept 3 (see Chapters 4.4.3 and 4.5.3) approximately 20% of the applied recharge amount ($5.79{\cdot}10^3$ m^3/d in the minimum and $1.58{\cdot}10^4$ m^3/d in the maximum approch) did not enter the model domain and were interpreted as surface runoff (Table 5.11 and 5.12). Thus, the net recharge amounts infiltrated into the model domain are $7.6{\cdot}10^6$ m^3/a (0.25 mm/a) in the minimum and $23.32{\cdot}10^6$ m^3/a (0.79 mm/a) in the maximum approach. These amounts are the lowest recharge rates estimated in this study. However, the later value seems to be plausible, since it lies within the range of estimated values reported in literature (*Mainardy*, 1999). Calibration statistics listed in Table 5.10 show similar results to the calibration statistics of Model 2 (Table 5.7) with a MAE of 23.64 m for the minimum and 21.72 m for the maximum and a RMS of 34.06 m and 28.89 m for the maximum and minimum approach respectively. This points towards a higher senitivity of the model on hydraulic parameters than on climatic ones. Thus, the implementation of the concepts based on the Topographic Index seems to be a encouraging approach for the inverse estimation of recharge rates and zones in investigation areas with better known hydraulic parameters (e.g. *Zhang et al.* (2007) implemented evaporation rates in discharge zones with no zero recharge and adjusted the rate during calibration). Against that, calibration in this thesis was done by tuning hydraulic conductivity based on fixed recharge rates according to a correlation of rainfall and elevation.

6.3 Model 2

6.3.1 Mass balance

Model 2 with a recharge distribution according to elevation (recharge concept 2, Chapter 4.4.2) applied basin wide recharge amounts of $36.87 \cdot 10^6$ m^3/a and $73.62 \cdot 10^6$ m^3/a equal to 1.25 mm/a and 2.25 mm/a within the minimum (0.5 % of annual rainfall) and maximum (1 % of annual rainfall) approach, respectively. *Mainardy* (1999) gives values for potential groundwater recharge rates estimated with ProcessingMODFLOW in carbonate rocks (665.4 km^2) near Okahandja of 0.3 to 6.4 mm/a, in quartzites (385.7 km^2) at Windhoek of 0.6 to 3.2 mm/a, in pegmatites at Windhoek (4.64 km^2) of 0.3 to 16 mm/a and in carbonate rocks (55.1 km^2) at Windhoek of 0.6 to 3.2 mm/a. Thus the implemented recharge rates obtained with recharge concept 2 are within the reported values range. Within both approaches evaporation compensates the applied recharge amount completely (Chapter 5.2.3). This arises from the fact that no groundwater discharge out of the basin can occur, except through a narrow bottleneck assigned at the outlet in layer 1 (Chapter 4.2), where upwelling of groundwater is forced by density varieties at the saltwater-freshwater interface, which is presented by a no-flow boundary (*Dingman*, 2008; *Gossel et al.*, 2004).
The use of the evaporation concept 2 (Chapter 4.5.2) seems to be reasonable due to low calculated water balance errors of -0.297 % for the minimum and -0.32 % for the maximum approach (Chapter 5.2.3). Nevertheless, this simple concept is based on a constant relative humidity within the basin and neglects further regional influecing factors (e.g. coastal versus mountainous terrain). Therefore, the regionalization and implementation of climate data surveyed within the basin, instead of the coarse regionalization based on the Atlas of Namibia (*DEA*, 2002), would provide further improvement in the estimation of evaporation rates.

6.3.2 Aquifer parameters

The model calibration with hydraulic conductivity, was started with literature values (Tables 4.4 and 4.5) which were consecutively modified. Moreover, they represent averaged magnitudes (EPM approach), covering large areas and fitted to a fixed recharge rate and distribution. The description of the decrease in hydraulic conductivity developed by *Saar & Magna* (2004) (Equation 2.6) was adopted, without changing the decay coefficient (δ=250 m), due to lack of information about the decrease in the study area. Thus, the hydraulic conductivity in the Swakop River basin decreased by 4% from layer 1 to 7 (down to 1000 m bgl) (Tables 5.5 and 5.6).

6.3.3 Model performance

The model performances of the maximum and minimum approaches resulted in similar calibration statistics (Table 5.7) with slightly better performances within the maximum approach with a RMS of 28.37 m and a MAE of 22.12 m.
The occurrence of the great number of dry cells toward the outlet of the basin in layers 1 and 2 (Figure 5.8), is profound to construe, because of lack of observed basement groundwater levels in this area. Reasons may be that recharge was not applied until the altitudinal belt of 400 m a.s.l. (Chapter 4.4.2) and the appearance of the highest evaporation rates in 500 m a.s.l.. Nevertheless the assumption, that there is a absence of recharge, does not have to be inaccurate. The analysis of stable isotopes ($^{1}8O$ and ^{2}H) in groundwater samples along the alluvial aquifer conducted by *Marx* (2009) represented no detectable altitude effect. This indicated a high longitudinal connectivity of floods between the upper and the lower catchment and therefore large amounts of indirect recharge caused by large floods generated in higher elevations. The dry cells occur mainly in the mountainous area of the moon landscape into which the rivers are deeply incised. So dry cells located in highest points are explicable by deep groundwater levels in hard rock mountains.
Most of the calculated residuals are negative which implies higher simulated groundwater heads than observed ones. The majority of negative residuals range from -72.54 m to -50 m (4.1 % of all residuals) and from -50 m to -30 m (Figures 5.9 a,b), can be associated with fault structures. In general areas where those structures are nested have higher hydraulic conductivities, a fact which was not considered in the model, because of the difficulty to implement small scale properties into a coarse grid size ((*Wolf et al.*, 2008)) and lack of data. The most negative residual with a value of -72.54 m, situated in the southeast of Otjimbingwe, possibly arises from its location at the interface between the Donkerhoek Batholith and schists of the Kuiseb Formation and a associated zone of higher hydraulic conductivity.
Residuals ranging from -30 m to -10 m and from -10 m to 10 m (Figure 5.9 c and d) represent the largest classes with 37.9 % and 28.3 %, respectivley. This is also reflected in the values of the MAE (22.12 m) and the residual mean (-13.93 m). Many of these residuals can also be put down to zones were faults are situated. The wide range of residual values located along the alluvial aquifers (Figures 5.9 c, d and e) indicate the versatile properties in individual river compartments (*CSIR*, 1997; *Marx*, 2009). Simulated groundwater levels lower than the observed ones, illustrated in Figures 5.9 e, f, g, and h, predominantly occur in the schists of the Kuiseb Formation. This may be attributed to the complex geological structures, with versatile hydraulic properties, since large negative residuals are situated in the vicinities as well. In general borehole

success rates and yields in the mica schists of the Khomas Highland decrease towards the Namib (*Müller*, 2001).

6.3.4 The groundwater flow system

The groundwater flow pattern is investigated in detail in order to determine recharge and discharge areas, to characterize the scales of prevailing ground water flow systems, to identify potential vertical and/or lateral fluxes into the alluvial aquifers as well as regional distinctions along the river reaches.
The simulated flow pattern seems to be mainly controlled by topography.
Calculated ground water flow directions agree in general with the ones plotted in the hydrogeological map (purple arrows in Figure 5.15, drawn in where sufficiently known (*Christelis & Struckmeier*, 2001)) and also some spring locations can be linked to convergences of velocity vectors implicating upwelling groundwater or discharge zones. It is important to note that in Figure 5.16 scales may differ slightly, due to scanning of the hydrogeological map, georeferencing and calculation of the watershed borders within ArcMap 9.3 based on the digital elevation model derived from SRTM data.
The equipotentials in Figure 5.15 show a line of potentiometric mounds that trend from the northeast of Wilhelmstal to the southwest of the basin along the strike of the Otjipatera and Chous Mountains. These mounds depict the groundwater divide where groundwater flow diverges to the subbasins of the Khan and the Swakop River. It is notable, that groundwater contributing to the southern part of the basin (Swakop subbasin) is forced through a narrow bottleneck at the southwestern basin border, located approximately 30 km in the west of the confluence of the rivers.
As shown by the velocity vectors in the cross- and longitudinal sections (Figures 5.18 and 5.19) the large scale groundwater flow of the two subbasins reflect a complex conglomerate of local and intermediate flow systems. In general, discharge areas can be associated with river valleys and troughs, but also with scarps and terraces if there is an upward break in the slope of the water level near the base of these. Recharge areas are situated at hills, mountains and ridges and in general at the boundary areas of the basin. The sections given in Figure 5.19 also depict the domination of local and intermediate flow systems. Recharge areas are alternating with their adjoining discharge areas on a local to medium scale. Further, no evidence for a regional flow system is visible, since no connected flow line between the lower points of the basin and higher elevations exist. This statement is also confirmed by the particle tracking analysis conducted near the outlet of the basin (Figure 5.20). In the three upper most layers shorter pathways preponderate with medial travel times between 9,555 a and 46,749 a. Particles placed in layers 5 and 7 had largest average horizontal distances of approximately 40 km between

entrances and occurrence in the layers. For the detection of a regional flow system, which in general characterizes coastal terrain groundwater flow systems ((*Anderman & Hill*, 2003)), the vertical extend of the model appears to be too shallow. But the Great Escarpment in the catchment is not as pronounced as elsewhere in Namibia, mainly due to erosion caused by drainage of Swakop- and Khan River also Damaran rocks present here weather more readily than rocks forming the Great Escarpment elsewhere (*Schneider et al.*, 2008), whereon shallower flow path could be attributed.
The model was not able to reproduce distinct deep flow pathways to the thermal springs (Gross-Barmen) located between the two surface water dams (Figure 5.21), which would have explained their origin. Particle analysis produced only short and shallow flow pathways to the spring located near the Swakoppoort Dam and thus could not account for high water temperatures, only one flow line at the thermal spring further west reached down to 650 m b.g.l.. The subsequent analysis within this cell resulted in a medial travel time of 644,151 a. By assuming a temperature gradient of 3 °C/100m and a general groundwater temperature of 20°C, the thermal water would have a temperature of 39.5 °C. It is debatable, if the model is able to explain the location of this spring exactly, since most flow pathways were short and not substantially deep.
The model results in the lower parts of the basin imply, that the zone of saline groundwater is caused by upwelling of groundwater and subsequent evaporation. Firstly, the longitudinal sections (e.g. Figure 5.19 R4) indicate upwelling of groundwater, no recharge areas and rather through flow or midline areas near the outlet in the upper most layers. In addition, Figure 5.15 shows an upward movement of groundwater (blue arrows between the rivers), induced by the convergence of the basin borders. This upward movement occurs rather in the northern part (Khan subbasin) where the saline zone (Figure 3.9) is located, while the southern part (Swakop subbasin) in this area is dominated by red arrows, indicating a downward movement. The highest evaporation rates appear around the altitudinal belt of 500 m a.s.l. (Chapter 4.5.2), leading to the occurrence of the saline zone.

6.3.5 River compartments

In Chapter 5.5 six selected river compartments were investigated (see positions in Figure 5.17). Mass balances were computed and flow pathways were produced with reverse particle tracking analyses.

Khan River:
In the RUL compartment the ratio of basement water to total inputs was 80% (indicator I1), from which 88% were contributed through inflow from the bottom of the alluvial aquifer (equal to 68% of total inputs). 19.1 m^3/d were percolating into layer 2, which represents the highest outflow occurring in compartments investigated along the Khan River. 65% of total inputs were removed through evaporation. As shown in Figure 5.24 particle traces (put on the bottom) indicate major flow pathways from northern directions. Also the mass balance plot for RUL (Figure 5.22) depicts the highest amounts for lateral inputs from the north and east (note that lateral fluxes include alluvium to compartment fluxes as well). High vertical inflow from the basement appears to be attributable to the convergence of the basin borders and as indicated by the blue arrows in Figure 5.15 in a discharge zone.
Compared to the RUL compartment, the VAL compartment has greater influence of evaporation, since it is located in the zone of the highest evaporation rates (around 500 m a.s.l.). 98% of all inputs were removed by evaporation. Direct recharge was a marginal contribution to the other input fluxes, illustrated by the high ratio of basement water to all inputs (I1 = 95%). Vertical inflow had a ratio of 56% to all basement water inflows occurring (equal to 54% of all inputs). The mass balance plot for the VAL compartment given in Figure 5.22 shows evened lateral fluxes from all directions (north include alluvium to compartment flows) like illustrated through particle traces (Figure 5.24), which are also characterized by larger average horizontal distances between entrances and exits of the particles (6428 m) than those from the RUL compartment (5411 m).
The compartment denoted North, located about 150 km upstream of the VAL compartment depicts a completely diverse picture. While basement input fluxes with a ratio of 93% to total inputs (I1) are similar to those from the VAL compartment. These arise predominatley from lateral inflows, since the fraction of vertical inflows to all basement water fluxes appearing is only 9%. As shown in Figure 5.22 lateral inputs are mainly determined by inflow from the alluvial aquifer into the compartment from the east. This point towards a location of the compartment rather within a recharge zone or a through flow area, than within a discharge zone. This seems to be confirmed by the shapes of the equipotentials (Figures 5.15) and the sooner parallel strike of velocity vectors in this area (Figures 5.15 and 5.16). Noticeable no compensation through evaporation took place.

The bar chart (Figure 5.23) clarifies the reactions of the compartments along the Khan River in the upstream direction. The strongest influence of vertical inflow (I3) is attributed to the RUL compartment, possibly caused by strong upwelling of groundwater induced by the location in a discharge area and the convergence of the basin borders. Further upstream the influence of vertical inflow decreases, also likely due to the opening of the Khan subbasin and the flattening of the area (for illustration, see map of the topographic index Figure 4.7). Readily identifiable is also the characteristic distribution of the evaporation zones implemented, and the absence of evaporation in the North compartment. Nevertheless this absence appears to be unrealistic since vegetation is predominantly located along the river reaches and especially occurs in the more humid eastern part of the catchment. Since evapotranspiration was not considered explicitly, this absence results possibly from the implemented evaporation extinction depth of 2 m (Chapter 4.5). Thus a further development of the model should account for vegetation distributions within the basin.

Swakop River:
The compartment in the southwest of the LHU compartment (SW-LHU) displays a similar picture to the RUL compartment in the Khan River (Figure 5.22). It seems to be mainly influenced by vertical inflow from the basement with a ratio of 88% to total basement water inputs (I3), what could also be caused by the converging shape of the basin. Since the compartment is located slightly higher, evaporation takes stronger effect (I4 = 77%). Like in the RUL compartment, vertical outflow occurs as well, with a small amount compared to vertical inflows. The highest lateral inflow from northern direction is caused by fluxes from the alluvial aquifer into the compartment as well as lateral fluxes from the basement into the compartment. The majority of produced particle traces have their entrances in the north. Nevertheless, small lateral inflows from the east and south are also existing.
The LHU compartment is influenced by vertical inflow with a ratio of 71% to total basement water inflows. Flow pathways originate mainly in northern direction at the Chuos Mountains where also the groundwater divide of the Swakop and Khan River is located. Longer and deeper flow pathways enter the alluvial aquifer from southern direction and have their origin in the Witwaters Mountains (position in Figure 3.2). Inflows from the north can also be attributed to fluxes from the alluvium into the compartment. Also small lateral inputs from the other cardinal points proceed. Indicator I4 shows a high influence of evaporation (97% of all fluxes occurring) and can again be attributed to the location within a discharge zone as well as to the position in the zone of highest evaporation rates.
As aforementioned in the discussion of the Khan river compartments, the influence of

evaporation decreases (I4 = 70%) in compartments located in elevations around. This is also recognizable in the Otjimbingwe compartment. The vertical inflow from the basement is higher than in the LHU compartement with a fraction of vertical inflow to total basement water inflow of 82% which is remarkable. Figure 4.7 illustrating the distribution of the topographic index within the basin depicts the location of the compartent surrounded by areas with minor indices (discharge zones). Moreover equipotentials and velocity vectors characterize the area as a prefered discharge zone with which high vertical inflows can be attributed.

A critical aspect investigating the river compartments is that the alluvial aquifers may not be displayed adequately due to the coarse model discretization. This leads to uniform hydraulic parameterization and the negligence of characteristic aquifer geometries. As shown in the bar chart (Figure 5.23) the reactions within the compartments are determined by local as well as regional properties. On the one hand the surrounding topography affects the compartment on the local scale while on the other hand large scale climatic conditions and topological aspects, i.e. the location within the basin according to convergence or divergence of the basin borders also characterize the compartment.

Chapter 7

Conclusion

The aim of the thesis was to develop an initial understanding of the groundwater flow system, to determine recharge and discharge areas as well as possible direct recharge rates, consistent with the basin geology.

Firstly, a simple conceptual model (Model 1) was developed and adopted. In the course of this study, the initial model was modified increasing complexity by including further basin characteristics (Model 2 and 3). The best results were obtained with Model 2 with a mean absolute error of 22.12 m and a root mean square error of 28.37 m ($R^2 = 0.992$). Most of the large residuals (observed minus simulated groundwater levels) could be linked to geological structures and amongst these mainly to highly fractured areas. Using this model, the groundwater flow pattern was investigated in detail. On the regional scale results show that groundwater is mainly recharged at the basin margins as well as along a line of potentiometric mounds that trend from the northeast of Wilhelmstal alongside the ridges of the Otjipatera and Chous Mountains to the southwest. From these mounds groundwater diverges to the northeast and southwest into the subbasins of the Khan and Swakop Rivers, respectively. This large scale flow pattern consists of a complex conglomerate of local and intermediate flow systems where recharge areas alternate with their adjacent discharge areas which are preferably located in troughs and river valleys. In contrast, no deep, regional groundwater flow system was identified since no connected flow lines between the lower points and higher elevations in the basin exist. This was confirmed by particle tracking analyses conducted at different locations in the basin. Model results further indicate that the zone of saline in the lower basin are caused by upwelling of groundwater and subsequent evaporation. Mass balance computations and particle tracking analyses in six selected river compartments insinuated different intensities of basement water influences depending on climatic and topographic basin characteristics. This was most clearly shown in the compartments of the Khan River where basement fluxes into the alluvial aquifer of the Khan River increased towards the confluence.

The numerical groundwater model of the Swakop River basin was able to picture the groundwater flow pattern by a discretization of the basin´s geology according to the Hydrogeological Map of Namibia (*DWA & GSN*, 2001) as well as using aquifer parameters given in literature (*Mattheß & Ubell*, 1983; *Mainardy*, 1999). The recharge rates determined for the basin with the models range from 0.25 mm/a to 2.25 mm/a. These results are within the range of reported rates in literature (*Mainardy*, 1999). It can be concluded that the groundwater system of the Swakop River is dominated by a pattern of local to intermediate flow systems rather than by a regional flow system. The amounts of basement water flowing into the compartments of the alluvial aquifers should be regarded tentatively due to the coarse discretization of the model. However, it was shown that for some compartments the influence of basement groundwater is significant and should thus not be neglected in further investigations of single aquifer compartments.

Further developments of the model should account for evapotranspiration in areas of denser vegetation as well as for a recharge distribution according to hydrogeological units implemented. Moreover, highly fractured areas should be considered by introducing higher hydraulic conductivities in the direction of the fractures strikes. Also the assignment of high productive well fields and the associated abstraction rates is possible, since withdrawals were neglected in this study. This model could be calibrated and validated with the estimated travel times by radiocarbon dating (upper age-limit about 45,000 a) (*Zhu & Murphy*, 2000; *Michael & Voss*, 2009). Telescopic mesh refinement (*HydrogeologicInc.*, 2007) depicts a possibility of creating more refined models within subregions of this large scale model. Therefore the model could be used as a fundament for small to medium scale modeling with greater resolution, contributing with bound information to a sustainable management of the region´s groundwater resources.

Appendix A

Tables

Table A.1: The effect of temperature on hydraulic conductivity

Depth [m]	K [m^2]	T [°C]	$\rho[kg/m^3]$	$\eta[kg/ms]$	τ	kf [m/d]	kf_t[m/d]
0	1.03E-12	20	1000	1.01E-03	9.71E+06	6.67E-01	8.64E-01
50	8.43E-13	21.5	1000	9.74E-04	1.01E+07	5.46E-01	7.34E-01
100	6.90E-13	23	1000	9.41E-04	1.04E+07	4.47E-01	6.22E-01
150	5.65E-13	24.5	1000	9.09E-04	1.08E+07	3.66E-01	5.27E-01
200	4.63E-13	26	1000	8.79E-04	1.12E+07	3.00E-01	4.46E-01
250	3.79E-13	27.5	1000	8.50E-04	1.15E+07	2.46E-01	3.78E-01
300	3.10E-13	29	1000	8.23E-04	1.19E+07	2.01E-01	3.20E-01
350	2.54E-13	30.5	1000	7.97E-04	1.23E+07	1.65E-01	2.70E-01
400	2.08E-13	32	1000	7.72E-04	1.27E+07	1.35E-01	2.28E-01
450	1.70E-13	33.5	1000	7.49E-04	1.31E+07	1.10E-01	1.93E-01
500	1.39E-13	35	1000	7.26E-04	1.35E+07	9.03E-02	1.63E-01
550	1.14E-13	36.5	1000	7.05E-04	1.39E+07	7.40E-02	1.37E-01
600	9.34E-14	38	1000	6.85E-04	1.43E+07	6.05E-02	1.16E-01
650	7.65E-14	39.5	1000	6.65E-04	1.47E+07	4.96E-02	9.75E-02
700	6.26E-14	41	1000	6.47E-04	1.52E+07	4.06E-02	8.21E-02
750	5.13E-14	42.5	1000	6.29E-04	1.56E+07	3.32E-02	6.91E-02
800	4.20E-14	44	1000	6.12E-04	1.60E+07	2.72E-02	5.82E-02
850	3.44E-14	45.5	1000	5.95E-04	1.65E+07	2.23E-02	4.90E-02
900	2.81E-14	47	1000	5.79E-04	1.69E+07	1.82E-02	4.12E-02
950	2.30E-14	48.5	1000	5.64E-04	1.74E+07	1.49E-02	3.46E-02
1000	1.89E-14	50	1000	5.50E-04	1.78E+07	1.22E-02	2.91E-02

Table A.2: Recharge zones and rates of recharge concept 2

Zone	Av. elevation [m amsl]	Area[km^2]	RCH = 0.5% of annual rainfall [m/d]	RCH=1% of annual rainfall [m/d]
1	50	78	0	0
2	150	158	0	0
3	250	236	0	0
4	350	272	0	0
5	450	537	$2.38{\cdot}10^{-7}$	$4.75{\cdot}10^{-7}$
6	550	582	$6.49{\cdot}10^{-7}$	$1.30{\cdot}10^{-6}$
7	650	719	$1.06{\cdot}10^{-6}$	$2.12{\cdot}10^{-6}$
8	750	1067	$1.47{\cdot}10^{-6}$	$2.94{\cdot}10^{-6}$
9	850	1305	$1.88{\cdot}10^{-6}$	$3.76{\cdot}10^{-6}$
10	950	1814	$2.29{\cdot}10^{-6}$	$4.58{\cdot}10^{-6}$
11	1050	2249	$2.7{\cdot}10^{-6}$	$5.41{\cdot}10^{-6}$
12	1150	2910	$3.11{\cdot}10^{-6}$	$6.23{\cdot}10^{-6}$
13	1250	3687	$3.53{\cdot}10^{-6}$	$7.05{\cdot}10^{-6}$
14	1350	3754	$3.94{\cdot}10^{-6}$	$7.87{\cdot}10^{-6}$
15	1450	3334	$4.35{\cdot}10^{-6}$	$8.69{\cdot}10^{-6}$
16	1550	2899	$4.76{\cdot}10^{-6}$	$9.52{\cdot}10^{-6}$
17	1650	1435	$5.17{\cdot}10^{-6}$	$1.03{\cdot}10^{-5}$
18	1750	1159	$5.58{\cdot}10^{-6}$	$1.12{\cdot}10^{-5}$
19	1850	720	$5.99{\cdot}10^{-6}$	$1.20{\cdot}10^{-5}$
20	1950	224	$6.40{\cdot}10^{-6}$	$1.28{\cdot}10^{-5}$
21	2050	59	$6.81{\cdot}10^{-6}$	$1.36{\cdot}10^{-5}$
22	2150	20	$7.22{\cdot}10^{-6}$	$1.44{\cdot}10^{-5}$
23	2250	1	$7.64{\cdot}10^{-6}$	$1.53{\cdot}10^{-5}$
total		29219	$1.01{\cdot}10^{5}$ [m^3/d] $3.68{\cdot}10^{7}$[m^3/a]	$2.02{\cdot}10^{5}$[m^3/d] $7.37{\cdot}10^{7}$[m^3/a]

Table A.3: Evaporation rates according to elevation. mean annual temperature and relative humidity - concept 2

Zone	Elevation [m amsl]	T° C	es [hPa]	RH [%]	e [hPa]	es-e [hPa]	ET [mm/d]
1	100	18	20.64	35	7.22	13.42	6.04
2	200	19	21.97	35	7.69	14.28	6.43
3	300	20	23.38	35	8.18	15.20	6.84
4	400	21	24.87	35	8.70	16.17	7.27
5	500	22	26.44	35	9.25	17.19	7.73
6	600	21.65	25.88	35	9.06	16.82	7.57
7	700	21.3	25.33	35	8.87	16.47	7.41
8	800	20.95	24.79	35	8.68	16.12	7.25
9	900	20.6	24.27	35	8.49	15.77	7.10
10	1000	20.25	23.75	35	8.31	15.44	6.95
11	1100	19.9	23.24	35	8.13	15.10	6.80
12	1200	19.55	22.74	35	7.96	14.78	6.65
13	1300	19.2	22.25	35	7.79	14.46	6.51
14	1400	18.85	21.77	35	7.62	14.15	6.37
15	1500	18.5	21.30	35	7.45	13.84	6.23
16	1600	18.15	20.84	35	7.29	13.54	6.09
17	1700	17.8	20.38	35	7.13	13.25	5.96
18	1800	17.45	19.94	35	6.98	12.96	5.83
19	1900	17.1	19.50	35	6.83	12.68	5.70
20	2000	16.75	19.07	35	6.68	12.40	5.58
21	2100	16.4	18.65	35	6.53	12.12	5.46
22	2200	16.05	18.24	35	6.38	11.86	5.34
23	2300	15.7	17.84	35	6.24	11.59	5.22

Bibliography

Abd Ellah, R. (2009). Evaporation rate at wadi el-rayan lake, egypt. World Applied Science Journal of African Earth Sciences, v. 38, iss. 5, p. 413-435., 6: 524–528.

Anderman, E. & Hill, M. (2003). Modflow-2000, the U.S. Geological Survey modular ground-water model - three additions to the hydrogeologic-unit flow (HUF) package. U.S. Geological Survey, Open File Report 03-347.

Anderson, J., Refsgaard, J., & Jenseni, K. (2001). Distributed hydrological modelling of the senegal river basin - model construction and validation. Journal of Hydrology, 247: 200–214.

Balke, K. (2000). Grundwassererschließung: Grundlagen, Brunnenbau, Grundwasserschutz, Wasserrecht. Borntraeger, Berlin, Stuttgart.

Barthel, R., Rojanschi, V., Wolf, J., & Braun, J. (2008). Modelling groundwater flow on the regional scale in the upper Danube catchment (germany). http://www.igeograf.unam.mx/aih/pdf/T8/T8-11.pdf, downloaded: 18.11.2009, 1:30 pm.

Bauer, P., Gumbricht, T., & Kinzelbach, W. (2006). A regional coupled surface water - groundwater model of the Okavango Delta, Botswana. Water Resources Research, 42, W04403: 1–15.

Belcher, W. (2004). Death valley regional ground-water flow system, Nevada and California. hydrogeologic framework and transient ground-water flow model. U.S. Geological Survey Scientific Investigations Report 2004-5205–only online, http://pubs.usgs.gov/sir/2004/2005/.

Beven, K. & Kirkby, M. (1979). A physically based, variable contributing area model of basin hydrology. Hydrological Sciences, 24: 43–69.

Breitkopf, J. & Maiden, K. (1988). Tectonic setting of the Matchless Belt pyritic copper deposits, Namibia. Economic Geology, 83: 710–723.

Carroll, R., Pohll, G., & Hershey, R. (2009). An unconfined groundwater model of the Death Valley Regional Flow System and a comparison to its confined predecessor. Journal of Hydrology, 373: 316–328.

Christelis, G. & Struckmeier, W. (2001). Groundwater in Namibia, an explanation to the Hydrogeological Map. Department of Water affairs.

CSIR (1997). An Assessment of the Potential Enviromental Impacts of the Proposed Aquifer Recharge Scheme on the Khan River, Namibia. Final Report. CSIR Division of Water, Environment & Forest Technology to Rössing Uranium Limited.

Dagan, G. (2002). An overview of stochastic modeling of groundwater flow and transport: From theory to applications. Eos, Transactions American Geophysical Union, 83: 621.

DEA (2002). Atlas of Namibia. Directorate of Environmental Affairs, Ministry of Environment and Tourism, Namibia.

Dingman, S. (2008). Physical Hydrology, second edition. Waveland Press, Inc.

DWA (1970). Department of water affairs. aquifer constants of alluvial sediments in the Khan and Swakop Rivers near Rössing. Report by Dziembowski, Geoloical Survey, Pretoria.

DWA (2004). Growas, groundwater database. Technical Report, Department of Water Affairs, Ministry of Agriculture, Water and Forestry.

DWA & GSN (2001). Hdrogeological Map of Namibia 1:1 000 000. Department of Water Affairs and Geological Survey of Namibia.

Ellmies, R. (2009). Strategic Environmental, Social and Economic Assessment for the Central Namib Uranium rush, BGR-GSN project; http://www.iaea.org/ourwork/st/ne/nefw/documents/rawmaterials/rtc-namibia-2009/ellmies%20%20-%20sea%20erongo%20region.pdf; downloaded: 04. february 2010, 9 a.m.

ESRI (2008). Arcmap 9.3. Environmental Systems Research Institute, Redlands, California, U.S.A.

Feyen, L. (2005). Large scale groundwater modelling. European Comission, Directorate General, Joint Research Centre, EUR 22124 EN.

Foster, S. S. D., Bath, A. H., Farr, J. L., & Lewis, W. J. (1982). The likelihood of active groundwater recharge in the Botswana Kalahari. Journal of Hydrology, 55: 113–136.

Gordon, M. (1986). Dependence of effective porosity on fracture continuity in fractured media. Ground Water, 24: 446–452.

Gordon, N., McMahon, T., Finlayson, B., Gippel, C., & Nathan, R. (2004). Stream Hydrology - An Introduction for Ecologists. John Wiley & Sons, Ltd, The Atrium, Southern Gate, Chichester, West Sussex, England.

Gossel, W., Ebraheem, A., & Wyciski, P. (2004). A very large scale GIS-based groundwater flow model for the Nubian sandstone aquifer in eastern Sahara (Egypt, northern Sudan and eastern Libya). Hydrogeology Journal, 12: 698–713.

Gruenert, N. (2003). Namibias faszinierende Geologie. Ein Reisehandbuch. Klaus Hess Verlag.

GSA (n.a.). htttp://memoirs.gsapubs.org/content/200/63/F13.large.jpg, downloaded 29.10.2009, 11:28 a.m.

GSN (n.a.). Geological map 1:250 000, digital data. Sheets: 2114 Omaruru, 2214 Walvis Bay, 2216 Windhoek, 2116 Okahandja.

Gunduz, O. & Aral, M. (2005). River networks and groundwater flow: a simultaneous solution of a coupled system. Journal of Hydrology 301 (2005) 216234, 301: 216–234.

Harbaugh, A., Banta, E., Hill, M., & McDonald, M. (2000). Modflow-2000, the U.S. Geological Survey modular ground-water model - user guide to modularization concepts and the ground-water flow process. Open-File Report 00-92, Page 121.

Heynes, P. (1992). Namibia's water resource: A new approach needed. Namibia Review, 1: 17–29.

Hueser, K., Besler, H., Bluemel, W., Heine, K., Leser, H., & Rust, U. (2001). Namibia. Eine Landschaftskunde in Bildern. Klaus Hess Verlag, Goettingen.

Huyakorn, P. (1986). A three dimensional finite-element model for simulating water flow in variably saturated porous media. Water Resources Research, 22: 1790–1808.

HydrogeologicInc. (2007). MODFLOW-SURFACT software (version 3.0). Herdon, VA, USA.

Ingebritsen, S. & Manning, C. (1999). Geological implications of a permeability-depth curve for the continental crust. Geology, 27: 1107–1110.

Ingebritsen, S. & Sanford, W. (1998). Groundwater in Geologic Processes. Cambridge University Press, New York.

ITCorporation (1996). Underground test area subproject, phase 1 data analysis task, hydrologic parameter data documentation package. Report ITLV/10972-181 prepared for the U.S. Department of Energy, 8 volumes, various pagnation, IV.

Jacobson, P., Jacobson, K., & Seely, M. (1995). Ephemeral Rivers and their catchments - sustaining people and development in western Namibia. Desert Research Foundation of Namibia, Windhoek.

Jung, S., Hoernes, S., Masberg, P., & Hoffer, E. (1999). The petrogenesis of some migmatites and granites (central Damara Orogen, Namibia): Evidence for disequilibrium melting, wall-rock contamination and crystal fractionation. Journal of Petrology, 40: 1241–1269.

Kim, N., Chung, I., Won, Y., & Arnold, J. (2008). Development and application of the integrated SWAT - MODFLOW model. Journal of Hydrology (, 356: 1–16.

Külls, C. (2000). Groundwater of the North-Western Kalahari, Namibia - Estimation of Recharge and Quantification of the Flow Systems. Dissertation, Julius-Maximilian University of Würzburg.

Klock, H. (2001). Hydrogeology of the Kalahari in north-easter Namibia with special emphasis on groundwater recharge, flow modelling and hydrochemistry. Dissertation, Julius-Maximilians-University of Würzburg.

Krasny, J. & Sharp, J. (2007). Groundwater in fractured rocks. Routledge.

Kresic, N. (2006). Hydrogeology and Groundwater Modeling. CRC Press Inc.

Lippert, R. (1986). Hydrogeologische Untersuchungen in kristallinen Festgesteinen im Bereich der Pfunderer Berge/Pustertal (Südtirol/Italien). Dissertation, Erlangen/Nürnberg.

Lubcynski, M. (1997). Application of numerical flow modelling combined with remote sensing and gis techniques for the quantification of regional groundwater resources in hard rock terrains. Hard Rock Hydrosystems (Proceedings of Rabat Symposium S2) IAHS, 241: 151–157.

Maidment, D. (1993). Handbook of Hydrology. McGraw-Hill Professional Publishing.

Mainardy, H. (1999). Grundwasserneubildung in der Übergangszone zwischen Festgesteinsrücken und Kalahari-Lockersedimentüberdeckung (Namibia). HU-Forschungsergebnisse aus dem Bereich Hydrogeologie und Umwelt, 17: 1–145.

Marklund, L. (2009). Topographic Control of Groundwater Flow. Dissertation, Department of Land and Water Resources Engineering, Royal Institut of Technology (KTH), Stockholm, Sweden.

Marx, V. (2009). Impacts of upstream uses on the alluvial aquifer of the Swakop River, Namibia. Diplomarbeit, Albert-Ludwigs Universität Freiburg, Institut für Hydrologie.

Massuel, S., George, B., Gaur, A., & Nune, R. (2007). Groundwater modeling for sustainable resource management in the Musi catchment, India. Paper presented at Proceedings, International Congress on Modelling and Simulation, Christchurch, New Zealand, 10: 1429–1435.

Mattheß, G. & Ubell, K. (1983). Allgemeine Hydrogeologie - Grundwasserhaushalt. Gebrüder Bornträger, Berlin-Stuttgart.

Mazor, E. (1982). Rain recharge in the Kalahari - a note on some approaches to the problem. Journal of Hydrology, 55: 137–144.

McDonald, M. & Harbaugh, A. (1988). A modular three-dimensional finite difference ground-water flow model. US Geological Survey, Techniques of Water Resources Investigations.

Michael, H. & Voss, C. (2009). Estimation of regional scale groundwater flow properties in the Bengal Basin of India and Bangladesch. Hydrogeology Journal, 17: 1379–13461.

Miller, R. M. (1983). Evolution of the Damara Orogen of South West Africa/Namibia. Geological Society of South Africa, Johannsburg.

Müller, S. (2001). Central namib - Windhoek area. Groundwater in Namibia, an explanation to the hydrogeological map, Department of Water Affairs, Pages 77–85.

Nagel, R. (1999). Eine Milliarde Jahre geologischer Entwicklung am NW-Rand des Kalahari Kratons. Dissertation, Mathematisch-Naturwissenschaftleiche Fakultäten, Georg-August-Universität Göttingen.

Nex, P., Herd, D., & Kinnaird, J. (2002). Fluid extraction from quartz in sheeted leucogranites as a monitor to styles of uranium mineralization: an example from the Rössing area, Namibia. Geochemistry: Exploration, Environment, Analysis, 2: 83–96.

Ophori, D. (2004). A simulation of large-scale groundwater flow and travel time in a fractured rock environment for waste disposal purposes. Hydrogeological Processes, 18: 1579–1593.

Ophori, D. U. (2007). A simulation of large scale groundwater flow in the Niger Delta, Nigeria. Environmental Geosciences, 14: 181–195.

Pollock, D. (1994). User´s guide for MODPATH/MODPATH-PLOT, version 3: A particel tracking post processing package for MODFLOW, the U.S. Geological Survey finite difference ground-water flow model. U.S. Geological Survey, Open-File Report 94-464, Page 252 p.

Refsgaard, J. (2001). Model Validation: Perspectives in Hydrological science, Chapter Discussion of model validation in relation to the regional and global scale, Pages 461–483. Wiley, New York.

Refsgaard, J. & Storm, B. (1995). Mike she. Singh, V. (Ed.). Computer models of Watershed Hydrology. Water Resources Publications, Highland Ranch, Colorado, Pages 809–846.

Rumbaugh, J. & Rumbaugh, O. (2007). Groundwater vistas, version 5. Environmental Simulation, Inc., Reinholds, PA.

Saar, M. & Magna, M. (2004). Depth dependence of permeability in the Oregon Cascades inferred from hydrogeologic, thermal, seismic, and magmatic modeling constraints. Journal of Geophysical Research-Solid Earth, 109.

Said, A., Stevens, D., & Sehlke, G. (2005). Estimating water budget in a regional aquifer using HSPF-MODFLOW integrated model. Journal of the American Water Resources Association, 41 (1): 55–66.

Scanlon, B., Mace, R., Barrett, M., & Smith, B. (2003). Can we simulate regional groundwater flow in a karst system using equivalent porous media models? case study, Barton Springs Edwards aquifer, U.S.A. Journal of Hydrology 276, 276: 137–158.

Schmidt, G. & Plöthner, D. (1999). Grundwasserstudie zum Otavi-Bergland/Namibia. Zeitschrift für angewandte Geologie, 44: 114–123.

Schneider, G., Becker, T., & von Benzig, L. (2008). The Roadside Geology of Namibia. Borntraeger.

Selroos, J., Walker, D., Ström, A., Gylling, B., & Follin, S. (2002). Comparison of alternative modelling approaches for groundwater flow in fractured rock. Journal of Hydrology, 257: 174–188.

Smith, D. (1965). The geology of the area around the Khan and Swakop Rivers in South West Africa. Geological Survey, Pretoria.

Tóth, J. (1962). A theory of groundwater motion in small drainage basins in central Alberta. Journal of Geophysical Research, 68: 4795–4812.

Tóth, J. (1963). A theoretical analysis of groundwater flow in small drainage basins. Journal of Geophysical Research, 16: 4795–4812.

Tóth, J. (1999). Groundwater as a geologic agent. Hydrogeology Journal, 7: 1–14.

Watkins, D. (2007). Groundwater in Fractured Rocks, Chapter 9. Determining a representative hydraulic conductivity of the Carnmenelis granite of Cornwall, UK, based on a range of sources of information, Pages 151–162. Taylor and Francis Group, London, UK.

Wolf, J., Barthel, R., & Braun, J. (2008). Modeling ground water flow in alluvial mountainous catchments on a watershed scale. GROUND WATER, 46, No.5: 695–705.

Wrabel, J. (1999). Ermittlung der Grundwasserneubildung im semiariden Bereich Namibias mittels der Chlorid-Bilanz-Methode. HU-Forschungsergebnisse aus dem Bereich Hydrogeologie und Umwelt, 16: 1–155.

Yu, Z., Pollard, D., & Cheng, L. (2006). On continental-scale hydrologic simulations with a coupled hydrologic model. Journal of Hydrology, 331: 110–124.

Zhang, Q., Varma, S., Bradley, J., & Schaeffer, J. (2007). Groundwater model of the Collie Basin western Australia. Hydrogeological Record Series, Record No. HG 15: 94.

Zhu, C. & Murphy, W. (2000). On radiocarbon dating of ground water. Ground Water, 38: 802–804.